UNIVERSITÀ DEGLI STUDI DI CATANIA

DOTTORATO DI RICERCA IN
SCIENZA DEI MATERIALI E NANOTECNOLOGIE

XXXV CICLO

LUCA PULVIRENTI

NOVEL HYBRID COMPOSITES BY SURFACE MODIFICATIONS OF FERRITE FOR ENVIRONMENTAL AND BIOMEDICAL APPLICATIONS

TUTOR: PROF G.G. CONDORELLI

TESI PER IL CONSEGUIMENTO DEL DOTTORATO DI RICERCA

Contents

CHAPTER 1: 6

Ferrites–Based Nanocomposites 6

1.1. Introduction 6

1.2. Ferrites: a perfect core for nanocomposites 7

1.2.1. Basics of Ferrites: Structures 8

1.2.2. Basics of Ferrites #2: Properties 11

1.2.3. Magnetite 14

1.2.4. Bismuth Ferrite 16

1.3. Self-Assembled Hybrid Coatings 17

1.3.1. Self-Assembled Monolayer (SAMs) 18

1.3.1.1. Characterization of SAMs 19

1.3.2. Metal Organic Framework (MOFs) 21

1.3.2.1. Materials of Institute Lavoisier (MIL) 22

References 23

CHAPTER 2 33

General Experimental Procedures 33

2.1. Synthesis of Ferrite Inorganic Core 33

2.1.1. Synthesis of Bismuth Ferrite 33

2.1.2. Synthesis of Magnetic Fe_3O_4 Nanoparticles (MNPs) 34

2.2. Functionalization Processes 34

2.2.1. Porphyrins anchoring on Bismuth Ferrite 34

2.2.2. Iron-Based MILs growth on Bismuth Ferrite 34

2.2.3. SAMs-functionalized Fe_3O_4 : overall synthetic route 35

2.2.4. Iron-Based MILs on Magnetite (Fe_3O_4) 37

2.3. Samples Characterization 37

2.4. General procedure for photocatalytic tests 39

2.5. General procedure for drug Loading and Release tests 40

2.6. Biological Tests 41

2.6.1. Cytotoxicity Assay 41

2.6.2. Cellular Uptake 42

2.6.3. Intracellular Localization 43

2.6.4. High-Content Screening (HCS) 43

Reference 44

CHAPTER 3 46

Porphyrin on Bismuth Ferrite nanocrystals for enhanced solar light photocatalysis. 46

3.1. Introduction 46

3.2. Results and Discussion 49

3.3. Conclusions 62

References 63

CHAPTER 4: 68

Enhancement of the visible light photo-induced antibacterial activity of $BiFeO_3$ nanocrystals by surface modification with MIL-101. 68

4.1. Introduction 68

4.2. Results and Discussion 69

4.3. Conclusions 78

CHAPTER 5: 84

Intracellular Transport: The Interplay between Sodium Butyrate, Folic Acid and a Multifunctional Paramagnetic Fe_3O_4 - Based System 84

5.1. Introduction 84

5.2. Results and Discussion 86

5.3. Conclusions 103

References 104

CHAPTER 6: 109

Enhancement of Temozolomide absorption and efficiency in glioblastoma treatment by MIL-modified Fe_3O_4 magnetic nanoparticles 109

6.1. Introduction 109

6.2. Results and Discussion 112

6.3. Conclusions 124

References 125

CHAPTER 1:

Ferrites–Based Nanocomposites

1.1. Introduction

The term nanocomposites refer to the research and technological development of combined materials on the atomic, molecular and macromolecular scale, leading to the design and construction of structures with scale length in the range of 1-100 nanometres. [1]

The concept behind these materials is very ancient, and throughout history, there are many reports of composite made without modern chemical knowledge. Blue Maya pigment and the ink used by the ancient Egyptians are just simple examples. [2] The first, in particular, is an incredible example of composite whose properties go far beyond that of a simple random mixture of components. This blue pigment was used for the colouring of the ancient Maya frescoes and has managed to withstand for over twelve centuries in a hostile environment such as the humid forests of South America. It is an organic-inorganic hybrid material, obtained through the combination of a natural blue dye (obtained from the Indigofera Tinctoria) encapsulated inside a clay mineral known as Palygorskite.[3] Many studies have shown that this pigment is able to oppose not only biodegradation, but also has a good resistance to attack form acid and alkaline solutions and from the most common organic solvents.

However, we had to wait many centuries before the hybrid nanosystems as we know them today were obtained. In the eighties, with the emergence of soft inorganic chemical processes, the research field of these nanomaterials will experienced an incredibly rapid development. [4,5] Since

then, the study of the so-called "functional hybrid nanocomposites" has become a research field of increasing interest and scientific and industrial implementation. The reason for this trend can be found in the multiple mechanical, thermal, magnetic and optical properties that these materials demonstrated.

Nowadays the potential of hybrid composites has become real, as many hybrid materials have entered the market in a variety of applications to satisfy the increasingly stringent design requirements. It is now clear that these systems do not represent an "exotic" alternative to conventional composites, but their characteristics make possible the creation of innovative advanced materials with high added value. [6]

Among them, the study of ferrite-based hybrid nanocomposites is a fast-growing research field of research due to their exponentially increasing use in magnetic biosensors, magnetic recording devices, electronic devices, [7] gyromagnetic devices, medical devices, [8] pollution control [9-11] and catalysis. [12,13]

Looking to the future, there is no doubt that these new generations of hybrid nanocomposites will play a key role in the development of advanced functional materials with improved properties.

1.2. Ferrites: a perfect core for nanocomposites

"Ferrite" is a generic name for a class of ceramic materials composed of iron oxide (Fe_2O_3) chemically combined with one or more additional metal elements. Iron oxide can react with a variety of different metals, including magnesium, aluminium, barium, manganese, copper, nickel, cobalt, and even iron itself, to generate various types of ferrites. [14] They have excellent electrical, magnetic and optical properties which arise from the interactions

between metallic ions occupying specific positions relative to the oxygen ions in the crystal structure of the oxide.

1.2.1. Basics of Ferrites: Structures

According to the above, ferrites exist in a variety of crystal structures and they can be classified in four types: spinel, garnet, ortho, and hexagonal ferrites.

Spinel Ferrites

Spinel Ferrites (SFs) are a group of ferrites with a face centred cubic crystal structure (Fig.1.1a). They have a general formula $MeFe_2O_4$ (with Me = Fe^{2+}, Zn^{2+}, Co^{2+}, Mn^{2+}, Ni^{2+}, Mg^{2+}, etc.). [15-17] Inside the spinel unit cell there are two types of interstices, both of which may be occupied by metal ions. These interstices are referred to as tetrahedral sites or "A" and octahedral sites or "B". Octahedral sites are larger than tetrahedral sites and normally only eight tetrahedral and 16 octahedral locations for unit cell are occupied by cations. Based on the distribution of cations in tetrahedral and octahedral sites, SFs can be classified as normal spinel, inverse spinel and mixed spinel. [18,19]

In normal spinel, divalent cations occupy one-eighth of the tetrahedral sites "A" and trivalent cations occupy half of the octahedral sites "B". [20] A typical example of normal spinel is $ZnFe_2O_4$. [21,22] In inverse spinel, all divalent cations occupy octahedral sites, while half of the trivalent cations occupy the tetrahedral sites "A" and the other half occupy the octahedral sites "B". A typical example of inverse spinel is Fe_3O_4 (Fig.1.1b). [23,24] In the random spinel structure, there is an equal distribution of cations on two sites based on site ratio and stoichiometry.

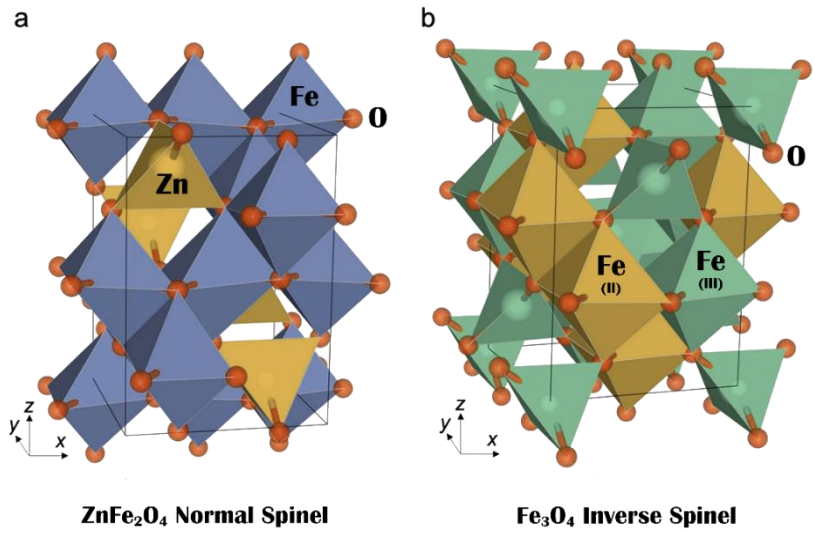

Fig.1.1. Crystalline structure of normal (a) and inverse (b) spinel ferrites

The general formula for these ferrites becomes $(M_{\delta}^{2+}Me_{(1-\delta)}^{3+})_A[M_{(1-\delta)}^{2+}Me_{(1+\delta)}^{3+}]_BO_4$, where δ is the inversion parameter, which depends on the preparation method and ferrite constituents. If δ = 1, the structure is that of a complete normal spinel, whereas for δ = 0, the complete inverse spinel exists. If δ varies between these two extreme values, spinel is called mixed spinel. A typical example of mixed spinel is $MgFe_2O_4$. [25]

Garnet Ferrites

Garnet ferrites have a cubic crystal structure. The general garnet formula is $R_3Fe_5O_{12}$, where R represents trivalent ion of rare earth such as yttrium, gadolinium or samarium. It has been estimated that the unit cell of the garnet contains 160 atoms. [26] The crystalline structure contains three crystallographic reticular sites: tetrahedral (a), octahedral (b) dodecahedral (c). Rare earth ions occupy dodecahedral sites, while iron ions are distributed in a ratio of 3:2 between tetrahedral and octahedral sites.

Orthoferrites (also known as Perovskite Ferrites)

Orthoferrites are chemical compounds that have a cubic structure with centred faces (Fig.1.2). Their general formula is $REFeO_3$. In these particular ferrites, RE is normally a rare earth element, but trivalent metal ions (Me^{3+}) can also be used. In these cases, as for bismuth ferrite, orthoferrite crystallizes in a perovskite-distorted structure of type $MeFeO_3$. [27]

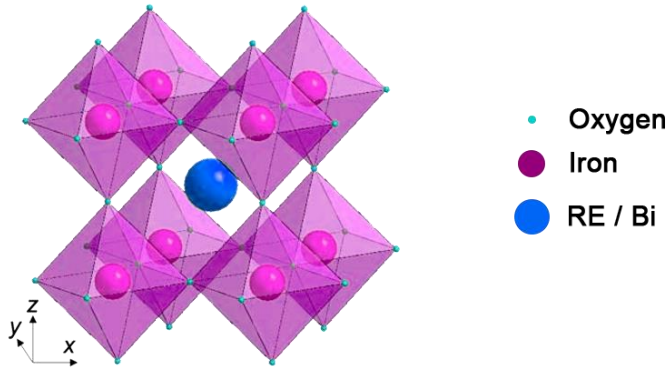

Fig.1.2. Crystalline structure of orthoferrite

In these distorted structures, the Fe^{3+} ions are coordinated to six oxygen anions, resulting in octahedral, with the iron ion at its centre. Cationic species Me^{3+} are located in the interstitial area between octahedral structures and is coordinated by 12 oxygen anions. [28]

Hexagonal Ferrites

Many ferrites fall into the category of hexagonal ferrites and the best known of these is certainly the barium ferrite. [29] All these ferrites have a hexagonal structure and are classified into some subgroups called M, Y, Z, U, W, which differ exclusively in the stoichiometric ratio between the components. Hexagonal ferrites have the general formula $MeFe_{12}O_{19}$, where Me is a divalent ion, such as Ba^{2+}, Sr^{2+} or Pb^{2+}. They have three interstitial

sites that can be occupied by metals: tetrahedral, octahedral and bi-pyramidal trigonal.

1.2.2. Basics of Ferrites #2: Properties

The distinctive property of ferrites is their permanent magnetism. As is known, this property is a direct consequence of the spin orientation of the different metal ions in their structure. Generally, they are aligned antiparallelly, giving rise to a ferrimagnetic alignment when the magnetic moments of the cations do not cancel each other out. The most used method to study the magnetic properties of these materials is to obtain their hysteresis curves. From these tests, it is possible to extract several parameters that are an index of the magnetic behaviour of the material. The most important among them are:

Coercivity (Hc): The intensity of the reverse magnetic field that must be applied to a material to cancel its magnetization after it has reached its saturation value.

Residual magnetization (Mr): The magnetization of the sample in the absence of an applied external magnetic field.

Saturation magnetization (Ms): The maximum magnetization can be achieved by a material when subjected to a magnetic field.

According to the values reached by these three parameters, ferrites can be divided into two important classes: soft and hard ferrites.

Soft ferrites are ferrimagnetic materials that lose decrease significantly their magnetism when the external magnetic field is removed. Therefore, they are not permanent magnets. Soft ferrites have a magnetization curve

characterized by a narrow hysteresis loop (Fig. 1.3a) and small energy losses during magnetization. The general formula of soft magnetic ferrites is $MeFe_2O_4$, where Me is a bivalent transition metal. Soft ferrites also have high susceptibility and permeability values and low coercivity values. [30,31] Soft ferrites are often used as transformers (for this they are often called transformer ferrites) and for the production of electromagnets and computer data storage. On the other hand, hard ferrites can retain their magnetism after being magnetized, and for this reason, they are also known as permanent magnets. These ferrimagnetic materials have a gradually increasing magnetization curve, a large hysteresis loop (Fig. 1.3b) and large energy losses during magnetization. The general formula of hard ferrite magnetic materials is $MeFe_{12}O_{19}$ or $MeFe_{18}O_{27}$. Where ME is usually barium, although this can be entirely or partially replaced by strontium or lead. Hard ferrites have low susceptibility and permeability and high coercivity. [32] Therefore, the main uses of hard ferrites are permanent magnets, DC magnets and speakers.

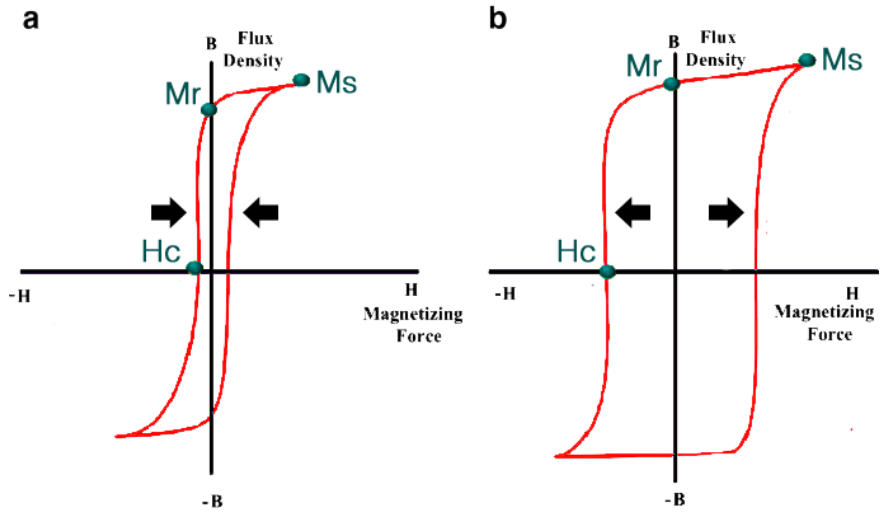

Fig.1.3. B-H curve for (a) soft ferrites and (b) hard ferrites.

Although the most common applications of ferrites are mostly related to their magnetic properties, some of them ($BiFeO_3$, $ZnFe_2O_4$ or $SrFe_{12}O_{19}$) have remarkable optical properties. The band structure of these ferrites classifies them as semiconductors, as their band gap usually falls below 2.7 eV. [33-35]

Figure 1.4 shows the absorption spectrum of solar radiation reaching Earth. It can be observed that UV radiation represents only 5% of solar energy, while visible light represents 46% of the total energy from the sun, with the remaining part corresponding to the infrared region. [36] Many of the photocatalysts that are commonly used have wide band gaps (> 3.1 eV) and are only able to use the small portion of sunlight corresponding to UV radiation. [37] Therefore, the development of photocatalysts capable of using a greater fraction of solar radiation effectively is important.

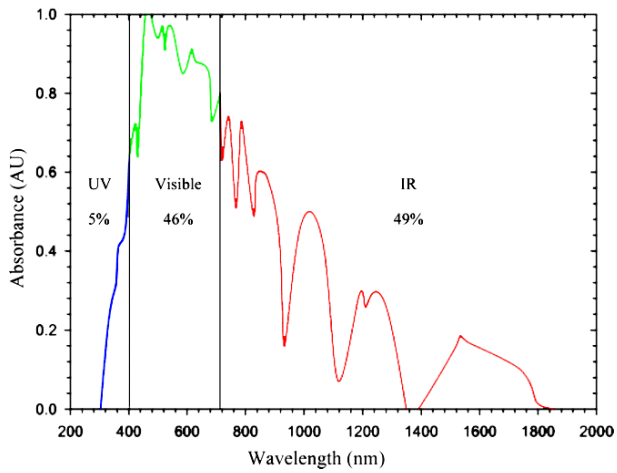

Fig.1.4. Solar energy spectrum

There are two main approaches that can be used to allow photocatalyst to exploit visible radiation. The first approach involves the use of doping elements to reduce the band-gap of an active material in the UV region. This is the strategy usually used to improve the performance of TiO_2. [38,39] The

most common dopants include nitrogen, [40] carbon, [41] silver, [42] gold, [43] and ruthenium. [44]

The second method, and also that of greatest interest for the writer of this thesis, is the study and development of materials that have a narrow band gap, which allows them a photocatalytic activity under visible light irradiation. [45,46]

The history, characteristics and applications of two of the most important ferrites are described below. For this thesis, magnetite has been studied for its magnetic properties and bismuth ferrite for its optical properties.

1.2.3. Magnetite

The history of ferrites (a word derived from the latin "Ferrum" for iron) began many centuries before the birth of Christ with the discovery of some stones that had the "mysterious" ability to attract iron. The most abundant deposits of these stones were found in the Magnesia district of Asia Minor. From this place, the mineral took the name of Magnetite (Fe_3O_4).

Among the iron oxides found in nature, due to its availability, versatility and eco-compatibility, the above-mentioned magnetite, is one of the most popular types of nanomaterials currently being researched, due to its availability, versatility and eco-compatibility. It is characterized by a crystalline cubic inverse spinel structure, where all the Fe^{2+} ions occupy the octahedral site and half of the Fe^{3+} ions are the octahedral lattice site and the other half in the tetrahedral sites. [47] This structure gives magnetite its unique and well-known magnetic properties.

One of the characteristics that make this material object of study even today is related to the behaviour of Fe_3O_4 nanocrystal (below 50 nanometres): superparamagnetism (Fig.1.5). [48]

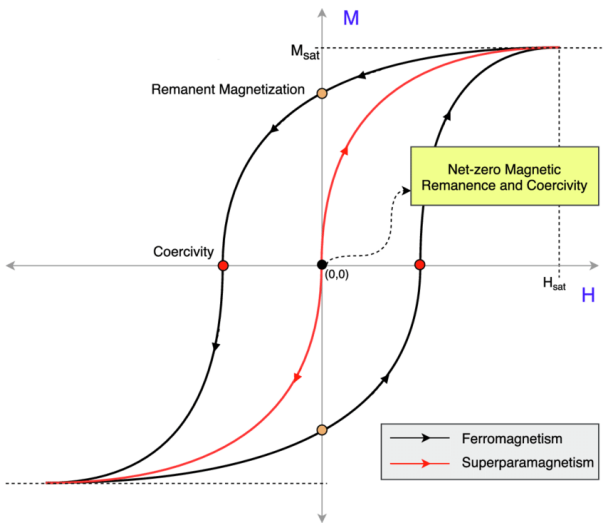

Fig.1.5. Magnetization of ferromagnetic (black line) and superparamagnetic (red line) materials by applied magnetic field.

Below this threshold, and in the absence of an external magnetic field, the magnetization of nanoparticles can randomly reverse direction under the effect of temperature. The time between two reversals is known as the Néel relaxation time. If the time used to measure the magnetization of nanoparticles is much longer than the Néel relaxation time, they will show an average magnetization value of zero and are said to be in a superparamagnetic state.

These magnetic properties make magnetite suitable for a wide range of applications. Among these, the most studied include magnetic separation, [49] catalysis, [50] batteries, [51] sorbents for the removal of pollutants. [52] In addition to its magnetic properties, it has excellent biocompatibility, biodegradability and non-toxicity for humans. These unique features are essential for biomedical applications, particularly for drug delivery systems. In the biomedical field, magnetite can be used for hyperthermia therapy [53], bio-sensing and diagnosis, [54] controlled and targeted drug delivery [55] and cancer treatment. [56]

1.2.4. Bismuth Ferrite

Bismuth ferrite ($BiFeO_3$ or even BFO) is an inorganic chemical compound discovered in the 1950s and one of the most promising multiferroic materials. [57]

BFO is a perovskite ferrite, name indicating a class of materials that follow the crystalline structure of formula ABO_3. This structure was first discovered in the mineral "perovskite" consisting essentially of calcium titanium oxide ($CaTiO_3$). In its ideal form, a perovskite has a cubic structure (space group Pm3m) and it is possible to identify two sites (A and B) that host the largest and the smallest cation respectively. It is interesting to note that most perovskites do not have this ideal theoretical cubic structure at room temperature, but often exhibit distortions.

Therefore, BFO can be described more correctly based on a rhombohedral cell (space group R3c), which contains two perovskite $BiFeO_3$ unit cells (Fig.1.6). [58,59] Compared to the ideal perovskite structure, the unit cell is distorted at an angle of about 89.4° and a reticular parameter of 3.965 A. [60]

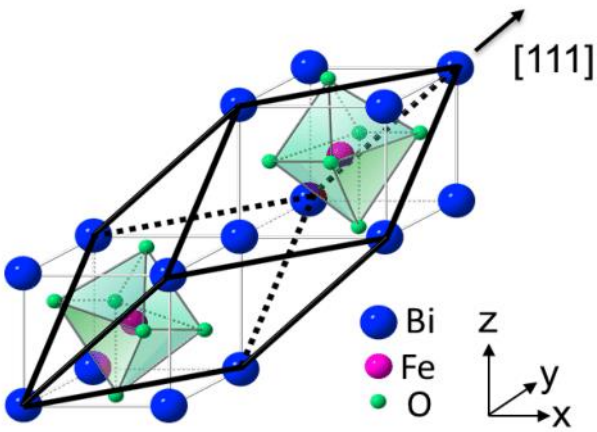

Fig.1.6. Crystal structure of $BiFeO_3$

BFO is a multiferroic material that is a material in which at least two among the ferroelectric properties and magnetic properties coexist simultaneously. In particular, the ferroelectric properties derive mainly from the lone pair (present in the orbital 6s of the valence shell) of the Bi^{3+} ions, present in the site A. While the magnetic properties (more specifically antiferromagnetic) depend on the element occupying the perovskite, site B, in this case the Fe^{3+} ions [61].

$BiFeO_3$ exhibits a wide range of functional properties, which are of particular interest in energy harvesting applications, [61] photochemical cells, [62] non-volatile memories, optical, [63] capacitors [64] and thin film capacitors, catalytic activity [65].

Bismuth ferrite is clearly a material with several remarkable properties, but one of them makes it stand out in the competitive field of photocatalysis. When compared to other semiconductors such as TiO_2, it has a very narrow band-gap, making it an efficient photocatalyst in the visible region of the solar spectrum.

BFO-based nanomaterials show superior photocatalytic activity when compared to a UV-active material. This makes it suitable for use in the degradation of harmful organic compounds such as dyes, organic waste and pesticides. Studies of photocatalytic activity on methyl-orange, [66] methylene blue, [67] and Rhodamine B [68] have been reported. It was also shown that by changing the surface area of the material, it is also possible to modify the band-gap, therefore, affecting the photocatalytic behaviour. [69]

1.3. Self-Assembled Hybrid Coatings

The molecular approaches of material science have reached such a level of sophistication that it is possible to control the assembly of a wide variety of nano-objects in complex and organized hybrid architectures (self-assembly,

metal-organic frameworks, bio-inspired strategies, etc.) for the production of smart materials and devices with complex structures at a high level of miniaturization.

1.3.1. Self-Assembled Monolayer (SAMs)

Self-assembled monolayers (SAMs) are highly ordered molecular assemblies (crystalline or semi-crystalline) that are formed through the adsorption and self-organization of molecular constituents, in liquid or gaseous phase, on the surface of a solid (substrate) with appropriate characteristics. [70] This approach is of great relevance as it allows the formation of complex structures of nanoscale size that would not be possible with traditional synthetic processes. [71] The concept of self-assembly on a substrate is a process known since the 1946, thanks to pioneering work of Zisman and colleagues on the anchoring of long chain of alcohols, amines and carboxylic acids on glass and metal surfaces. [72,73] However, it was only in the 1978 that the term "self-assembled monolayers" was used for the first time. That year, Dietman Mobius described in the journal Topics in Surface Chemistry the technique of manipulating monolayers. [74] In the same year, Polymeropoulos and Sagiv presented an interesting article on the ability of some monolayers deposited on aluminium to detect the variation of the electrical conduction between two metal surfaces as function of temperature changes. [75] Their work was the first demonstration of the real applicability and stability of SAMs. A few years later in 1980, Savig also had the merit of having demonstrated the possibility of producing monolayers from liquid phase, in an article on the self-assembly of homogenous oleophobic monolayers directly from organic solutions.

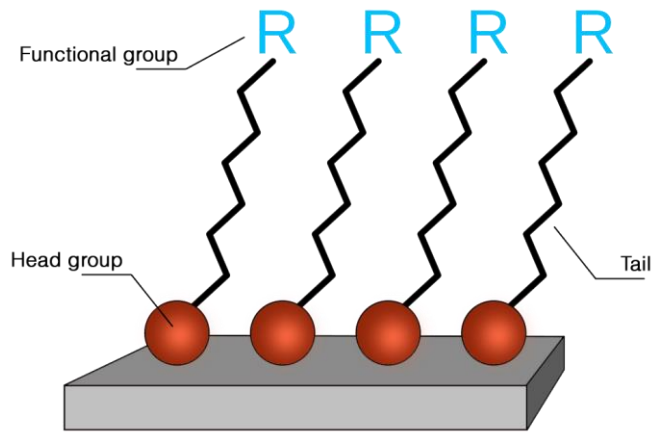

Fig.1.7. Graphical representation of a Self-Assembled Monolayer

Nowadays, self-assembled monolayers are an important element of modern nanotechnology. [76,77] They are considered the most highly versatile, cost effective, flexible and simple method for the functionalization of metal, metal oxide and semiconductor surfaces, and especially for the anchoring of molecules and biomolecules in the manufacture of new and more advanced supramolecular architectures.

1.3.1.1. Characterization of SAMs

Self-assembled monolayers (SAMs) must be characterized in order to determine their quality. Parameters such as thickness, coverage uniformity, molecular orientation, composition, and thermal and chemical stability often play a critical role for applicability of these materials. To do this, numerous experimental methods can be used. These methods include both physical measurements such as contact angle and wettability, and spectroscopic techniques like X-ray photon spectroscopy (XPS), infrared spectroscopy (IR), Auger electron spectroscopy (AES), fluorescence spectroscopy and surface plasmon resonance (SPR) providing valuable information about the structure and dynamics of SAMs. Some of these methods, which have provided key

information for the realization of this thesis, are briefly discussed in this chapter.

XPS is a powerful diagnostic tool to analyse SAMs because of its sampling depth (about 5-10 nm) which makes this techniques highly surface sensitive. In this technique, incident X-rays bombard the sample and the electrons are ejected without inelastic collision from the core shells of the atoms of the layers close to the surface. These electrons are collected and selected as function of their kinetic energies. The electron binding energy calculated through the Koopman theorem from the measured kinetic energy is specific for each element and provides indications on the oxidation state of the elements. It can be used to probe the chemical nature of modified layers and, in particular, to determine the presence of a covalent bonds between the SAM head group and the substrate, the involved chemical species and their oxidation states and the SAM thickness.

FT-IR is also a reliable technique for the chemical characterization of nanoparticles functionalized with SAMs. It allows the identification of the functional groups present in the system, measuring the specific vibrational frequencies of the involved chemical bonds. The vibrational excitation energy of the molecules is in the range corresponding to infrared radiation (10^{13} - 10^{14} Hz). This means that IR spectroscopy can be used to study the vibrational transitions of SAMs functional groups anchored to nanoparticle surfaces. In addition, the characteristic peaks of organic molecules typically used to anchor metal oxide surfaces (such as carboxylic and phosphonic groups) are located in areas of the infrared spectrum without interfering signals. This allows a simpler and more correct interpretation of the spectra, despite, normally, the infrared characterization of surface coatings is a challenge because of the high sampling depth of this techniques which decreases the sensitivity towards surface elements.

1.3.2. Metal Organic Framework (MOFs)

Metal Organic Framework (MOFs) is an emerging class of porous materials consisting of transition metal ions (or clusters of metal ions) that occupy nodal positions within a large crystalline network held together by polydentate organic ligands. [78,79]

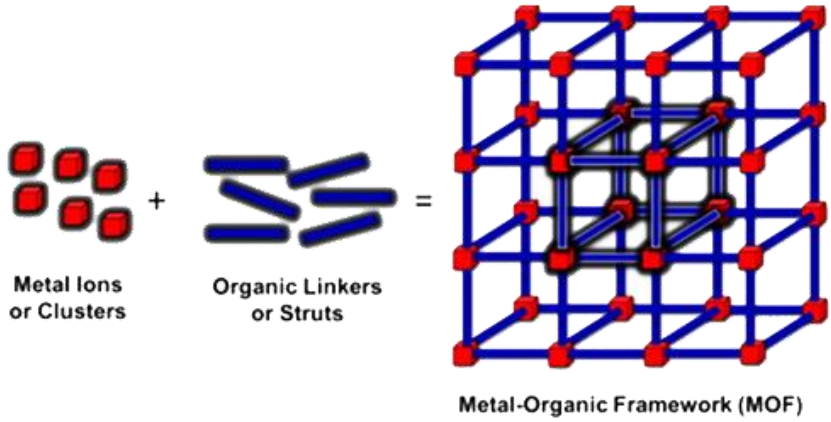

Fig.1.8. Graphical representation of MOFs [80]

Key features of these hybrid materials are high porosity, resulting in high surface area and low density, but also great thermal and chemical stability. [81]

One of the main advantages of MOFs as materials is the possibility to combine a large variety of transition metals and organic binders, which possess completely different chemical and physical properties. Due to their structural adaptability, a dynamic structure with adjustable pore sizes, as well as their ever-expanding scope, have become one of the most fascinating material classes to study, offering endless possibilities of design of functional materials.

All these aspects give MOFs the possibility to be exploited in various fields of application, such as gas separation, hydrogen storage, molecular recognition, drug administration and catalysis. [82]

There are thousands of MOFs that have been discovered and named according to their origin and serial number.

Among these, the MILs (Matériaux de l'Institut Lavoisier) are of particular application interest.

1.3.2.1. Materials of Institute Lavoisier (MIL)

MILs materials are one of the most studied MOFs groups. They typically consist of carboxylate ligands and trivalent cation clusters (such as Cr^{3+}, Fe^{3+}, Al^{3+}, etc…). Among these, the most known, especially with regard to potential applications, are those based on 1,4-Benzenedicarboxylic (terephthalic). [83] such as the MIL-53, MIL-88, and MIL-101 which are all isomers to each other. They are assembled from the same metal secondary building units and organic linkers, but differ in both connectivity and properties. [84,85]

MIL-101 family have a similar topology to zeolites, but differ in surface morphology, density, and pore size. For example, MIL-101(Fe) is composed of octahedral chains Fe(III) as a secondary construction unit (SBU) and 1,4-Benzenedicarboxylic acid. [86]

This group of MOFs has several application potentials, both in the environmental and biomedical fields. MIL-101 is considered to be an excellent adsorbent due to its exceptional water/chemical stability, high porosity and large specific surface area. [87] Many studies have shown these materials can be used for selective adsorption of dyes, pollutants or drugs, revealing adsorption performance significantly higher than traditional compounds.

In addition, MIL-101 has usually good photocatalytic properties. This capacity is mainly determined by two factors that play a critical role in determining photo-degradative efficiency. First, a tridimensional structure with high order and periodicity. As mentioned above, the MILs have

permanent and uniform pores and an ultra-high surface area, resulting in an abundance of active sites and excellent mass transfer capacity. [88] Finally, the band structure of the photocatalysts can be regulated by modifying organic ligands or by introducing functional substituents into organic ligands. [89.90]

References

1. Okpala, C. C. (2013). Nanocomposites–an overview. International Journal of Engineering Research and Development, 8(11), 17-23.

2. Christiansen, T., Cotte, M., de Nolf, W., Mouro, E., Reyes-Herrera, J., De Meyer, S., ... & Larsen, S. (2020). Insights into the composition of ancient Egyptian red and black inks on papyri achieved by synchrotron-based microanalyses. Proceedings of the National Academy of Sciences, 117(45), 27825-27835.

3. Gómez-Romero, P., & Sanchez, C. (2005). Hybrid materials. Functional properties. From Maya Blue to 21st century materials. New journal of chemistry, 29(1), 57-58.

4. Yadav, S., Rani, N., & Saini, K. (2022, February). A review on transition metal oxides based nanocomposites, their synthesis techniques, different morphologies and potential applications. In IOP Conference Series: Materials Science and Engineering (Vol. 1225, No. 1, p. 012004). IOP Publishing.

5. Parashar, M., Shukla, V. K., & Singh, R. (2020). Metal oxides nanoparticles via sol–gel method: a review on synthesis, characterization and applications. Journal of Materials Science: Materials in Electronics, 31, 3729-3749.

6. Chongdar, S., Bhattacharjee, S., Bhanja, P., & Bhaumik, A. (2022). Porous organic–inorganic hybrid materials for catalysis, energy and environmental applications. Chemical Communications, 58(21), 3429-3460.

7. Sharif, A., Mustaqeem, M., Saleh, T. A., ur Rehman, A., Ahmad, M., & Warsi, M. F. (2022). Synthesis, structural and dielectric properties of Mg/Zn ferrites-PVA nanocomposites. Materials Science and Engineering: B, 280, 115689. 12.

8. Kefeni, K. K., Msagati, T. A., Nkambule, T. T., & Mamba, B. B. (2020). Spinel ferrite nanoparticles and nanocomposites for biomedical applications and their toxicity. Materials Science and Engineering: C, 107, 110314.

9. Kefeni, K. K., Mamba, B. B., & Msagati, T. A. (2017). Application of spinel ferrite nanoparticles in water and wastewater treatment: a review. Separation and Purification Technology, 188, 399-422.

10. Kumar, M., Dosanjh, H. S., Singh, J., Monir, K., & Singh, H. (2020). Review on magnetic nanoferrites and their composites as alternatives in wastewater treatment: synthesis, modifications and applications. Environmental Science: Water Research & Technology, 6(3), 491-514.

11. Reddy, D. H. K., & Yun, Y. S. (2016). Spinel ferrite magnetic adsorbents: alternative future materials for water purification? Coordination Chemistry Reviews, 315, 90-111.

12. Abu-Dief, A. M., & Abdel-Fatah, S. M. (2018). Development and functionalization of magnetic nanoparticles as powerful and green catalysts for organic synthesis. Beni-Suef University Journal of Basic and Applied Sciences, 7(1), 55-67.

13. Kharisov, B. I., Dias, H. R., & Kharissova, O. V. (2019). Mini-review: Ferrite nanoparticles in the catalysis. Arabian Journal of Chemistry, 12(7), 1234-1246.

14. Almessiere, M. A., Slimani, Y., Trukhanov, A. V., Sadaqat, A., Korkmaz, A. D., Algarou, N. A., ... & Toprak, M. S. (2021). Review on functional bi-component nanocomposites based on hard/soft ferrites: structural, magnetic, electrical and microwave absorption properties. Nano-Structures & Nano-Objects, 26, 100728.

15. Qin, H., He, Y., Xu, P., Huang, D., Wang, Z., Wang, H., ... & Wang, C. (2021). Spinel ferrites (MFe_2O_4): Synthesis, improvement and catalytic application in environment and energy field. Advances in Colloid and Interface Science, 294, 102486.

16. Ramimoghadam, D., Bagheri, S., & Abd Hamid, S. B. (2014). Progress in electrochemical synthesis of magnetic iron oxide nanoparticles. Journal of Magnetism and Magnetic Materials, 368, 207-229.

17. Bromho, T. K., Ibrahim, K., Kabir, H., Rahman, M. M., Hasan, K., Ferdous, T., ... & Jiang, Z. T. (2018). Understanding the impacts of Al+

3-substitutions on the enhancement of magnetic, dielectric and electrical behaviors of ceramic processed nickel-zinc mixed ferrites: FTIR assisted studies. Materials Research Bulletin, 97, 444-451.

18. Šutka, A., & Gross, K. A. (2016). Spinel ferrite oxide semiconductor gas sensors. Sensors and Actuators B: Chemical, 222, 95-105.

19. Cullity, B. D., & Graham, C. D. (2011). Introduction to magnetic materials. John Wiley & Sons.

20. Burdett, J. K., Price, G. D., & Price, S. L. (1982). Role of the crystal-field theory in determining the structures of spinels. Journal of the american chemical society, 104(1), 92-95.

21. Greenberg, E., Rozenberg, G. K., Xu, W., Arielly, R., Pasternak, M. P., Melchior, A., ... & Dubrovinsky, L. S. (2009). On the compressibility of ferrite spinels: a high-pressure X-ray diffraction study of M Fe_2O_4 (M= Mg, Co, Zn). High Pressure Research, 29(4), 764-779.

22. O'neill, H., & St, C. (1992). Temperature dependence of the cation distribution in zinc ferrite ($ZnFe_2O_4$) from powder XRD structural refinements. European Journal of Mineralogy, 571-580.

23. Sickafus, K. E., Wills, J. M., & Grimes, N. W. (1999). Structure of spinel. Journal of the American Ceramic Society, 82(12), 3279-3292.

24. Rozenberg, G. K., Amiel, Y., Xu, W. M., Pasternak, M. P., Jeanloz, R., Hanfland, M., & Taylor, R. D. (2007). Structural characterization of temperature-and pressure-induced inverse↔ normal spinel transformation in magnetite. Physical Review B, 75(2), 020102.

25. Antao, S. M., Hassan, I., & Parise, J. B. (2005). Cation ordering in magnesioferrite, $MgFe_2O_4$, to 982 C using in situ synchrotron X-ray powder diffraction. American Mineralogist, 90(1), 219-228.

26. Berchmans, L. J., Karthikeyan, R., Helan, M., Berchmans, S., Ŝepelak, V., & Becker, K. D. (2011). Mechanochemical synthesis and electrochemical characterization of nano crystalline calcium ferrite. Catalysis letters, 141(10), 1451-1457.

27. Dixon, C. A., Kavanagh, C. M., Knight, K. S., Kockelmann, W., Morrison, F. D., & Lightfoot, P. (2015). Thermal evolution of the crystal structure of the orthorhombic perovskite $LaFeO_3$. Journal of Solid State Chemistry, 230, 337-342.

28. Ahmed, M. A., Selim, M. S., & Arman, M. M. (2011). Novel multiferroic $La_{0.95}Sb_{0.05}FeO_3$ orthoferrite. Materials Chemistry and Physics, 129(3), 705-712.

29. Pullar, R. C. (2012). Hexagonal ferrites: a review of the synthesis, properties and applications of hexaferrite ceramics. Progress in Materials Science, 57(7), 1191-1334.

30. Zabotto, F. L., Gualdi, A. J., Eiras, J. A., Oliveira, A. J. A. D., & Garcia, D. (2012). Influence of the sintering temperature on the magnetic and electric properties of $NiFe_2O_4$ ferrites. Materials Research, 15, 428-433.

31. Chauhan, L., Shukla, A. K., & Sreenivas, K. (2015). Dielectric and magnetic properties of Nickel ferrite ceramics using crystalline powders derived from DL alanine fuel in sol–gel auto-combustion. Ceramics International, 41(7), 8341-8351.

32. Dho, J., Lee, E. K., Park, J. Y., & Hur, N. H. (2005). Effects of the grain boundary on the coercivity of barium ferrite $BaFe_{12}O_{19}$. Journal of Magnetism and Magnetic Materials, 285(1-2), 164-168.

33. Ravindra, A. V., Padhan, P., & Prellier, W. (2012). Electronic structure and optical band gap of $CoFe_2O_4$ thin films. Applied Physics Letters, 101(16), 161902.

34. Wang, H., Zheng, Y., Cai, M. Q., Huang, H., & Chan, H. L. (2009). First-principles study on the electronic and optical properties of $BiFeO_3$. Solid State Communications, 149(15-16), 641-644.

35. Fang, C. M., Kools, F., Metselaar, R., & De Groot, R. A. (2003). Magnetic and electronic properties of strontium hexaferrite $SrFe_{12}O_{19}$ from first-principles calculations. Journal of Physics: Condensed Matter, 15(36), 6229.

36. Sen, Z. (2008). Solar energy fundamentals and modeling techniques: atmosphere, environment, climate change and renewable energy. Springer Science & Business Media.

37. Li, S., Lin, Y. H., Zhang, B. P., Nan, C. W., & Wang, Y. (2009). Photocatalytic and magnetic behaviors observed in nanostructured $BiFeO_3$ particles.

38. Yang, J., Chen, C., Ji, H., Ma, W., & Zhao, J. (2005). Mechanism of TiO2-assisted photocatalytic degradation of dyes under visible irradiation: photoelectrocatalytic study by TiO_2-film electrodes. The Journal of Physical Chemistry B, 109(46), 21900-21907.

39. Anpo, M., & Takeuchi, M. (2003). The design and development of highly reactive titanium oxide photocatalysts operating under visible light irradiation. Journal of catalysis, 216(1-2), 505-516.

40. Fu, H., Zhang, L., Zhang, S., Zhu, Y., & Zhao, J. (2006). Electron spin resonance spin-trapping detection of radical intermediates in N-doped TiO_2-assisted photodegradation of 4-chlorophenol. The Journal of Physical Chemistry B, 110(7), 3061-3065.

41. Zhang, X., Lei, L., Zhang, J., Chen, Q., Bao, J., & Fang, B. (2009). A novel CdS/S-TiO_2 nanotubes photocatalyst with high visible light activity. Separation and Purification Technology, 66(2), 417-421.

42. Zielińska, A., Kowalska, E., Sobczak, J. W., Łącka, I., Gazda, M., Ohtani, B., ... & Zaleska, A. (2010). Silver-doped TiO_2 prepared by microemulsion method: Surface properties, bio-and photoactivity. Separation and Purification Technology, 72(3), 309-318.

43. Luo, S., Xiao, Y., Yang, L., Liu, C., Su, F., Li, Y., ... & Zeng, G. (2011). Simultaneous detoxification of hexavalent chromium and acid orange 7 by a novel Au/TiO_2 heterojunction composite nanotube arrays. Separation and Purification Technology, 79(1), 85-91.

44. Senthilnanthan, M., Ho, D. P., Vigneswaran, S., Ngo, H. H., & Shon, H. K. (2010). Visible light responsive ruthenium-doped titanium dioxide for the removal of metsulfuron-methyl herbcide in aqueous phase. Separation and purification technology, 75(3), 415-419.

45. Casbeer, E., Sharma, V. K., & Li, X. Z. (2012). Synthesis and photocatalytic activity of ferrites under visible light: a review. Separation and Purification Technology, 87, 1-14.

46. Gao, T., Chen, Z., Huang, Q., Niu, F., Huang, X., Qin, L., & Huang, Y. (2015). A review: preparation of bismuth ferrite nanoparticles and its applications in visible-light induced photocatalyses. Rev. adv. mater. sci, 40(2), 97-109.

47. Yew, Y. P., Shameli, K., Miyake, M., Khairudin, N. B. B. A., Mohamad, S. E. B., Naiki, T., & Lee, K. X. (2020). Green biosynthesis

of superparamagnetic magnetite Fe_3O_4 nanoparticles and biomedical applications in targeted anticancer drug delivery system: A review. Arabian Journal of Chemistry, 13(1), 2287-2308.

48. Bean, C. P., & Livingston, U. D. (1959). Superparamagnetism. Journal of Applied Physics, 30(4), S120-S129.

49. Valeev, D., Kunilova, I., Alpatov, A., Varnavskaya, A., & Ju, D. (2019). Magnetite and carbon extraction from coal fly ash using magnetic separation and flotation methods. Minerals, 9(5), 320.

50. Niculescu, A. G., Chircov, C., & Grumezescu, A. M. (2022). Magnetite nanoparticles: Synthesis methods–A comparative review. Methods, 199, 16-27.

51. Zhang, S., Li, W., Tan, B., Chou, S., Li, Z., & Dou, S. (2015). One-pot synthesis of ultra-small magnetite nanoparticles on the surface of reduced graphene oxide nanosheets as anodes for sodium-ion batteries. Journal of Materials Chemistry A, 3(9), 4793-4798.

52. Panda, S. K., Aggarwal, I., Kumar, H., Prasad, L., Kumar, A., Sharma, A., ... & Mishra, V. (2021). Magnetite nanoparticles as sorbents for dye removal: a review. Environmental Chemistry Letters, 19(3), 2487-2525.

53. Shaterabadi, Z., Nabiyouni, G., & Soleymani, M. (2018). Physics responsible for heating efficiency and self-controlled temperature rise of magnetic nanoparticles in magnetic hyperthermia therapy. Progress in biophysics and molecular biology, 133, 9-19.

54. Chircov, C., Grumezescu, A. M., & Holban, A. M. (2019). Magnetic particles for advanced molecular diagnosis. Materials, 12(13), 2158.

55. Yew, Y. P., Shameli, K., Miyake, M., Khairudin, N. B. B. A., Mohamad, S. E. B., Naiki, T., & Lee, K. X. (2020). Green biosynthesis of superparamagnetic magnetite Fe_3O_4 nanoparticles and biomedical applications in targeted anticancer drug delivery system: A review. Arabian Journal of Chemistry, 13(1), 2287-2308.

56. Soleymani, M., Khalighfard, S., Khodayari, S., Khodayari, H., Kalhori, M. R., Hadjighassem, M. R., ... & Alizadeh, A. M. (2020). Effects of multiple injections on the efficacy and cytotoxicity of folate-targeted magnetite nanoparticles as theranostic agents for MRI detection and magnetic hyperthermia therapy of tumor cells. Scientific reports, 10(1), 1-14.

57. Gulati, S., Goyal, K., Arora, A., Kumar, S., Trivedi, M., & Jain, S. (2022). Bismuth ferrite ($BiFeO_3$) perovskite-based advanced nanomaterials with state-of-the-art photocatalytic performance in water cleanup. Environmental Science: Water Research & Technology.

58. Moreau, J. M., Michel, C., Gerson, R., & James, W. J. (1971). Ferroelectric $BiFeO_3$ X-ray and neutron diffraction study. Journal of Physics and Chemistry of Solids, 32(6), 1315-1320.

59. Bucci, J. D., Robertson, B. K., & James, W. J. (1972). The precision determination of the lattice parameters and the coefficients of thermal expansion of $BiFeO_3$. Journal of Applied Crystallography, 5(3), 187-191.

60. Kubel, F., & Schmid, H. (1990). Structure of a ferroelectric and ferroelastic monodomain crystal of the perovskite $BiFeO_3$. Acta Crystallographica Section B: Structural Science, 46(6), 698-702.

61. Queraltó, A., Frohnhoven, R., Mathur, S., & Gómez, A. (2020). Intrinsic piezoelectric characterization of $BiFeO_3$ nanofibers and its implications for energy harvesting. Applied Surface Science, 509, 144760.

62. Pattnaik, S. P., Behera, A., Martha, S., Acharya, R., & Parida, K. (2018). Synthesis, photoelectrochemical properties and solar light-induced photocatalytic activity of bismuth ferrite nanoparticles. Journal of Nanoparticle Research, 20, 1-15.

63. Ghahfarokhi, S. E. M., Larki, M. R., & Kazeminezhad, I. (2020). The effect of Mn doped on the structural, magnetic, dielectric and optical properties of bismuth ferrite ($BiFe_{1-x}MnxO_3$) nanoparticles. Vacuum, 173, 109143.

64. Yan, F., Shi, Y., Zhou, X., Zhu, K., Shen, B., & Zhai, J. (2021). Optimization of polarization and electric field of bismuth ferrite-based ceramics for capacitor applications. Chemical Engineering Journal, 417, 127945.

65. Iqbal, M. A., Ali, S. I., Amin, F., Tariq, A., Iqbal, M. Z., & Rizwan, S. (2019). La-and Mn-codoped Bismuth Ferrite/Ti_3C_2 MXene composites for efficient photocatalytic degradation of Congo Red dye. ACS omega, 4(5), 8661-8668.

66. Wang, S., Chen, D., Niu, F., Zhang, N., Qin, L., & Huang, Y. (2016). Hydrogenation-induced surface oxygen vacancies in $BiFeO_3$ nanoparticles for enhanced visible light photocatalytic performance. Journal of Alloys and Compounds, 688, 399-406.

67. Sharma, P., Zhang, Q., Sando, D., Lei, C. H., Liu, Y., Li, J., ... & Seidel, J. (2017). Nonvolatile ferroelectric domain wall memory. Science advances, 3(6), e1700512.

68. Hsieh, Y. H., Xue, F., Yang, T., Liu, H. J., Zhu, Y., Chen, Y. C., ... & Chu, Y. H. (2016). Permanent ferroelectric retention of $BiFeO_3$ mesocrystal. Nature communications, 7(1), 1-9.

69. Li, S., Lin, Y. H., Zhang, B. P., Wang, Y., & Nan, C. W. (2010). Controlled fabrication of $BiFeO_3$ uniform microcrystals and their magnetic and photocatalytic behaviors. The Journal of Physical Chemistry C, 114(7), 2903-2908.

70. Love, J. C., Estroff, L. A., Kriebel, J. K., Nuzzo, R. G., & Whitesides, G. M. (2005). Self-assembled monolayers of thiolates on metals as a form of nanotechnology. Chemical reviews, 105(4), 1103-1170.

71. Isaacs L., Chin D. N., Bowden N., Xia Y. and Whitesides G. M., Perspectives in Supramolecular Chemistry, Wiley & Sons, Chichester, 4, 1 (1999).

72. Bigelow, W. C., Pickett, D. L., & Zisman, W. A. (1946). Oleophobic monolayers: I. Films adsorbed from solution in non-polar liquids. Journal of Colloid Science, 1(6), 513-538.

73. Bigelow, W. C., Glass, E., & Zisman, W. A. (1947). Oleophobic monolayers. II. Temperature effects and energy of adsorption. Journal of colloid science, 2(6), 563-591.

74. Möbius, D. (1978). Monolayer Assemblies. In Topics in Surface Chemistry (pp. 75-101). Springer, Boston, MA.

75. Sagiv, J., & Polymeropoulos, E. E. (1978). Electrical conduction through adsorbed monolayer. J. Chem. Phys., 69, 1836.

76. Sagiv, J. (1980). Organized monolayers by adsorption. 1. Formation and structure of oleophobic mixed monolayers on solid surfaces. Journal of the American Chemical Society, 102(1), 92-98.

77. Onclin, S., Ravoo, B. J., & Reinhoudt, D. N. (2005). Engineering silicon oxide surfaces using Self-Assembled monolayers. Angewandte Chemie International Edition, 44(39), 6282-6304.

78. Ricco, R., Pfeiffer, C., Sumida, K., Sumby, C. J., Falcaro, P., Furukawa, S., ... & Doonan, C. J. (2016). Emerging applications of metal–organic frameworks. CrystEngComm, 18(35), 6532-6542.

79. Zhang, W. X., Liao, P. Q., Lin, R. B., Wei, Y. S., Zeng, M. H., & Chen, X. M. (2015). Metal cluster-based functional porous coordination polymers. Coordination Chemistry Reviews, 293, 263-278.

80. Dhakshinamoorthy, A.; Garcia, H. Catalysis by Metal Nanoparticles Embedded on Metal-Organic Frameworks. Chem. Soc. Rev. 2012, 41, 5262–5284.

81. Almeida Paz, F. A.; Klinowski, J.; Vilela, S. M. F.; Tomé, J. P. C.; Cavaleiro, J. A. S.; Rocha, J. Ligand Design for Functional Metal-Organic Frameworks. Chem. Soc. Rev. 2012, 41, 1088–1110.

82. Yap, M. H., Fow, K. L., & Chen, G. Z. (2017). Synthesis and applications of MOF-derived porous nanostructures. Green Energy & Environment, 2(3), 218-245.

83. Barea, E., Montoro, C., & Navarro, J. A. (2014). Toxic gas removal–metal–organic frameworks for the capture and degradation of toxic gases and vapours. Chemical Society Reviews, 43(16), 5419-5430.

84. Hamon, L., Llewellyn, P. L., Devic, T., Ghoufi, A., Clet, G., Guillerm, V., ... & Férey, G. (2009). Co-adsorption and separation of CO2− CH4 mixtures in the highly flexible MIL-53 (Cr) MOF. Journal of the American Chemical Society, 131(47), 17490-17499.

85. Knebel, A., Zhou, C., Huang, A., Zhang, J., Kustov, L., & Caro, J. (2018). Smart Metal-Organic Frameworks (MOFs): Switching Gas Permeation through MOF Membranes by External Stimuli. Chemical Engineering & Technology, 41(2), 224-234.

86. Serre, C., Millange, F., Surblé, S., & Férey, G. (2004). A route to the synthesis of trivalent transition-metal porous carboxylates with trimeric secondary building units. Angewandte Chemie International Edition, 43(46), 6285-6289.

87. Sun, C. Y., Qin, C., Wang, C. G., Su, Z. M., Wang, S., Wang, X. L., ... & Wang, E. B. (2011). Chiral nanoporous metal-organic frameworks with high porosity as materials for drug delivery. Advanced Materials, 23(47), 5629-5632.

88. Xu, W. T., Ma, L., Ke, F., Peng, F. M., Xu, G. S., Shen, Y. H., ... & Yuan, Y. P. (2014). Metal–organic frameworks MIL-88A hexagonal microrods as a new photocatalyst for efficient decolorization of methylene blue dye. Dalton transactions, 43(9), 3792-3798.

89. Lionet, Z., Kim, T. H., Horiuchi, Y., Lee, S. W., & Matsuoka, M. (2019). Linker engineering of iron-based MOFs for efficient visible-light-driven water oxidation reaction. The Journal of Physical Chemistry C, 123(45), 27501-27508.

90. Xu, C., Fang, R., Luque, R., Chen, L., & Li, Y. (2019). Functional metal–organic frameworks for catalytic applications. Coordination chemistry reviews, 388, 268-292.

CHAPTER 2

General Experimental Procedures

2.1. Synthesis of Ferrite Inorganic Core

2.1.1. Synthesis of Bismuth Ferrite

The BFO particles were synthesized using the sol-gel method. Typically, 5 mmol of bismuth nitrate pentahydrate [$Bi(NO_3)_3$ x $5H_2O$] and iron nitrate nonahydrate [$Fe(NO_3)_3$ x $9H_2O$] in stoichiometric proportion (molar ratio 1:1) are dissolved separately in ethylene glycol (Chapter 3) or in distilled water (Chapter 4) and then mixed together. Bismuth nitrate is only slightly soluble in water, for this, some drops of nitric acid are added. Once both were solubilized, 5 mmol of tartaric acid [$C_4H_6O_6$] were added to the resulting solution under constant magnetic stirring. The sol formed was heated to 80 ºC to obtain a soft dry gel and then transferred to a crucible to be filled in a furnace where it was kept at 600 ºC for 2 hours to obtain the required BFO phase. Finally, the as prepared particles were washed several times with distilled water and ethanol.

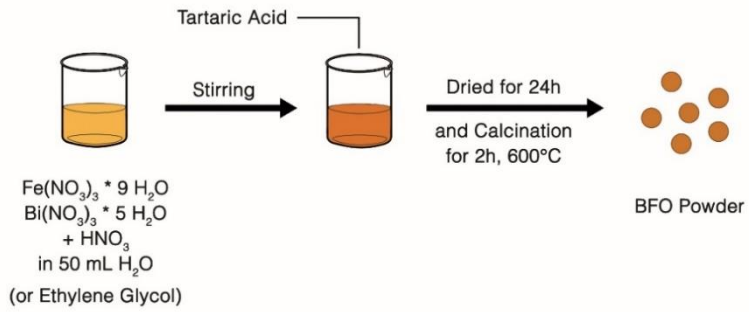

Fig.2.1. Schematic representation for the synthesis of BFO

2.1.2. Synthesis of Magnetic Fe_3O_4 Nanoparticles (MNPs)

Magnetic Nanoparticles were obtained by co-precipitation method according to the procedure described below. NH_4OH (5 mL, 25%) was added to a water solution obtained dissolving iron (II) chloride tetrahydrate [$FeCl_2$ x $4H_2O$] and iron (III) chloride hexahydrate [$FeCl_3$ x $6H_2O$] (1:2 molar ratio) under N_2 atmosphere and constant stirring. The reaction was kept to 80ºC for 30min, and then the resulting suspension was cooled to room temperature and washed with ultrapure water. The synthesized magnetic nanoparticles (MNPs) were separated from the solvent by magnetic decantation.

2.2. Functionalization Processes

2.2.1. Porphyrins anchoring on Bismuth Ferrite

For the anchoring of the porphyrins on the BFO a two-step process was carried out. In the first step, the surface of the inorganic particles was activated. To do this they were placed in a round-bottomed flask and sonicated for 30 minutes before being refluxed in an aqueous solution of hydrogen peroxide at 100 ºC for 2 hours. The activated particles (100 mg) were subsequently dispersed in 5 ml of a solution of Tetrakis (4-carboxyphenyl) porphyrin (TCPP) in ethanol (1 mM) and stirred overnight. The composite was recovered from dispersion by centrifugation at 6000 rpm for 10 min. After grafting, the particles were washed by re-dispersion in ethanol and recollection by centrifugation.

2.2.2. Iron-Based MILs growth on Bismuth Ferrite

The MIL structures with which bismuth ferrite nanoparticles are functionalized are obtained by direct growth process from solution. A batch

of nanoparticles is suspended in a beaker containing 15 ml of DMF in which 1 mmol of 2-aminotherephthalic acid and 0.1 mmol of Iron (III) chloride hexahydrate are previously solubilized. The reaction was kept reflux for 4 hours in an oil bath at 90 ºC. The functionalized nanoparticles are separated through centrifugation and rinsed several times in ethanol and water.

2.2.3. SAMs-functionalized Fe_3O_4 : overall synthetic route

In order to better understand the synthetic pathway adopted for the organic functionalization of magnetic nanoparticles, an overall summary diagram is presented below (Fig.2.2).

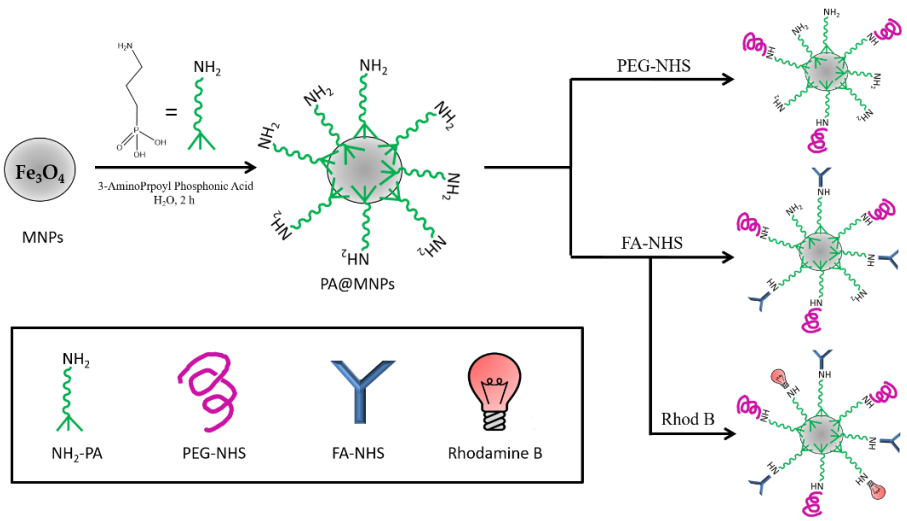

Fig.2.2. Overall synthetic scheme

The functionalized MNPs used in Chapter 5 were synthetized adopting a multistep procedure. [1,2] This methodology is based on the pre-functionalization of magnetic nanoparticles with 3-aminophosphonic acids (NH_2-PA) which is a bifunctional linker capable of binding the Fe_3O_4 surface through its phosphonic acid group, leaving the amino portion available for other reactions. N-hydroxysuccinimide (NHS) activated PEG (PEG-NHS) alone or in a mixture (1:1) with NHS-activated FA (FA-NHS) were bonded

to NH_2-PA pre-functionalized MNPs (MNPs@PA) through an amide bond formation in order to obtain MNPs@PEG and MNPs@PEG-FA, respectively. Finally, for fluorescence measurements, a Rhodamine luminescent probe was added to the coating of the MNP@PEG-FA samples.

- ***Synthesis of N-Hydroxysuccinimide Ester of Folic Acid (FA-NHS)***

N-Hydroxysuccinimide Ester of Folic Acid (FA-NHS) was prepared in according to the following published methodology. [3]

In brief, 500 mg of Folic Acid (FA) were dissolved in 10 mL of DMSO with 240 mL of triethylamine. Then, 260 mg N-hydroxysuccinimide (NHS) and 470 mg N,N-dicyclohexylcarbodiimide (DCC) were added and the mixture was left to react overnight at room temperature in the dark. The by-product, dicyclohexylurea (DCU), was removed by filtration. The DMSO solution was subsequently concentrated under reduced pressure and FA-NHS precipitated into diethyl ether. The product was washed several times using anhydrous ether and air-dried.

- ***3-Aminopropylphosphonic acid anchoring on MNPs (MNPs@PA)***

A small amount of MNPs (200 mg) was dispersed in 25 mL of H_2O using an ultrasonic bath for 30 min. After this, 100 mg of 3-aminopropylphosphonic acid (NH_2-PA) was added to the suspension, which was agitated for 2 hours at room temperature. Finally, the particles were magnetically separated and washed several times with H_2O, then ethanol and dried in air.

- ***PEG anchoring on modified MNPs (MNPs@PEG)***

PA@MNPs (300 mg) and 30 mg of PEG-NHS were dispersed in 15 mL DMSO. The solution was stirred overnight at 25 ◦C. The as obtained

particles were separated magnetically, washed with DMSO, H_2O, ethanol and then air-dried.

- ***FA anchoring on PEGylated MNPs (MNPs@PEG-FA)***

MNPs@PEG-FA were obtained by a process similar to the one described above, but by adding 3 mg of FA-NHS to the solution.

- ***Carboxy-X-Rhodamine anchoring on FA-PEGylated MNPs***

Carboxy-X-Rhodamine marked FA-PEG@MNPs were obtained with the same procedure, but with the addition of Rhod-NHS (3 mg) to the solution described above.

2.2.4. Iron-Based MILs on Magnetite (Fe_3O_4)

MIL frameworks were grown through two similar route both using Fe_3O_4 nanoparticles as the metal core and Fe^{3+} ion source. In particular, in the first route (a) Fe_3O_4 magnetic nanoparticles (0.25 g) were dissolved in an ethanol or DMF solution (15 mL) of 2-aminoterephthalic acid (0.16 g) and the reaction was kept under reflux for 4h in an 80°C oil bath. Functionalized nanoparticles were successively separated by magnetic decantation and washed by re-dispersion in ethanol and recollection. The synthetic second route (b) was similar to the previous one but with the addition of iron (III) chloride hexahydrate (0.08 g) as external source of Fe^{3+} ions to the ethanol solution.

2.3. Samples Characterization

X-ray diffraction (**XRD**) was performed using both a θ-θ Bruker-AXS D5005 diffractometer equipped with a Göebel mirror to parallel Cu Kα radiation operating at 40 kV and 30 mA, and an XRD Smartlab Rigaku

diffractometer (Tokyo, Japan) in grazing incident mode (0.5°) operating with a rotating anode of Cu Kα source radiation at 45 kV and 200 mA.

X-ray photoelectron spectroscopy (**XPS**) spectra were recorder with a PHI 5600 multitechnique ESCA spectrometer equipped with a standard Mg Kα X-ray source. Analyses were carried out at a 45° photoelectron angle (relative to the sample surface) with an acceptance angle of ± 7°. The XPS binding energy (B.E.) scale was calibrated by centring C 1s peak due to hydrocarbon moieties and "adventitious" carbon at 285.0 eV.

For **FT-IR** measurements, both a Nicolet 6700 FT-IR spectrophotometer and a JASCO FT-IR 4600LE (Easton, MD, USA) spectrometer were used. The spectral range analyzed was between 560 and 4000 cm^{-1}, with a resolution of 4 cm^{-1}. The samples were diluted with dry KBr to 2 wt% and pure KBr was used as a reference.

UV–Vis absorption spectra were recorded on a Nicolet Evolution 500 UV–Vis spectrometer for the liquids. For solid state measurements of powders, UV–Vis-DR spectra were recorded by using a diffuse reflectance DR accessory and using KBr standard as white reference.

BET Surface Area (**SBET**) measurement of BFO samples (Chapter 3) was calculated via a multipoint BET method.

Thermal Gravimetric Analysis (**TGA**) was performed using a Mettler Toledo TGA/SDTA 851. All the curves were acquired in O_2 flow in the temperature range 25–600°C with a heating rate of 5°C min-1. N_2-sorption analysis was carried out on a Quantachrome Quadrasorb SI automated gas adsorption system. Before starting the measurement, the samples were

degassed using an AS-6 degasser for 16 h at 150 °C, and then the analysis was performed at -196 °C.

SEM (Scanning Electron Microscope) images were obtained using a field emission scanning electron microscope (FESEM) ZEISS VP 55 (Oberkochen, Germany).

TEM (Transmission Electron Microscopy) analysis was carried out with a JEOL JEM 2010F (Akishima, Tokyo, Japan) working at 200 kV accelerating voltage. The dried powder was dispersed mechanically on an ultra-thin carbon coated lacey carbon grid.

2.4. General procedure for photocatalytic tests

The photocatalytic degradation experiments, both for Chapter 3 and Chapter 6, were performed by dispersing the photocatalyst (50 mg) in 50 mL of a Methylene Blue (or Rhodamine B) solution ($1.5x10^{-5}$ M for both dyes). The solution was magnetically stirred into a dark room for 30 minutes to achieve the adsorption-desorption equilibrium between the dye and the catalyst surface. After that, the catalyst/dye suspension was irradiated with sunlight using a Unnasol US 800, 180 W solar simulator. In this experimental configuration, the average irradiance measured by a Thorlabs PM160T optical power meter was $50mW/cm^2$. During irradiation, at certain time intervals, small aliquots (4 mL) were collected and centrifuged to remove the photocatalyst and dye concentration was determined by UV-Vis spectroscopy at wavelengths of 664 nm and 540 nm for MB and Rhd-B respectively. The stability of the photocatalyst was verified by repeating the MB degradation measures four times. The effect of the pH of the dye solution on the

photodegradation of the MB was investigated by varying the pH from 3 to 12, by adding HCl or NaOH.

To evaluate i) the role of OH radicals• and ii) the catalytic effectiveness of free TCPP, degradation of Rhd-B was carried out also in the presence of a) 2-propanol ($2x10^{-3}$M) and b) using free TCPP (0.1 mg/ml) rather than BFO@TCPP.

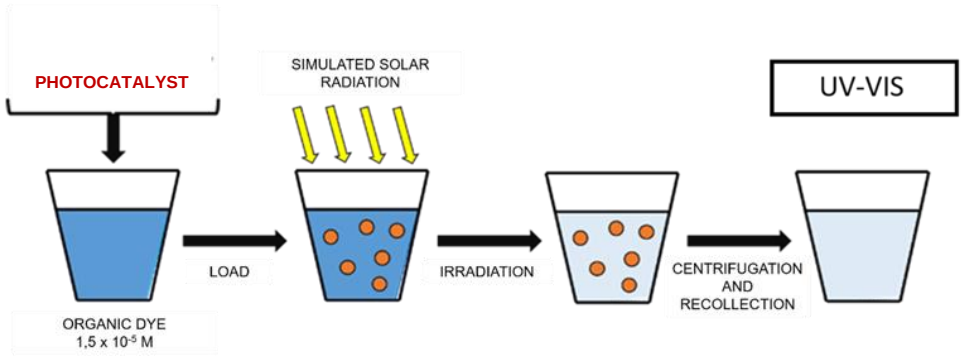

Fig.2.3. Schematic representation for the procedure of photocatalytic tests

2.5. General procedure for drug Loading and Release tests

The drug loading and release studies were performed in triplicate and the amount of loaded and release drug was analyzed using a JASCO V-560 UV/vis spectrophotometer (Easton, MD, USA) equipped with a 1 cm path length cell at 230 nm.

Before the drug loading experiments were performed, preliminary tests were carried out with an organic dye. A stock solution of Rhodamine B (Rhd B) ($6x10^{-6}$ M) was prepared by dissolution of the simulant in water. Loading tests were carried out dispersing the samples (3 mg) in the Rhodamine B solution (4 mL). The solution was maintained under agitation in an orbital shaker and, every 30 minutes, a small batch of the sample (1 mL) was removed and analyzed. Then the nanoparticles were recollected from the solution thought magnetic separation and put into pure water to

perform the release test. The suspension was again kept under stirring and, every 30 minutes, a small amount of sample (1 mL) was removed and analyzed using UV/Vis spectrometry.

In the case of Temozolomide (TMZ) (Chapter 6) loading tests, experiments were conducted in the same way as the Rhd B experiments mentioned above using a $2x10^{-4}$ M TMZ solution in water. The TMZ solution was prepared by dissolving 39 µL of the TMZ stock solution in DMSO (51.51 mM) in 10 mL of water. This means that the amount of DMSO in the loading solution is approximately 0.4%. Unfortunately, the release of TMZ could not be investigated because of its low absorption coefficient and its maximum position (372 nm) overlapping with that of the free aminoterephthalic ligand present in MIL solutions. [4]

2.6. Biological Tests

2.6.1. Cytotoxicity Assay

LoVo cells (Chapter 5) were seeded into 24-well tissue culture plates, at a concentration of 3×10^4 in each well and incubated for 24 h. After this pre-adhesion time, the medium was changed with fresh medium containing different MNPs. After 48 and 72 h of incubation, a cytotoxicity assay in the presence of different concentrations of free butyrate, was performed using an MTT test, based on the reduction of yellow 3-(4,5-dimethythiazol-2-yl)-2,5-diphenyl tetrazolium bromide (MTT) by mitochondrial succinate dehydrogenase. The optical density (OD) values at 570 nm of the samples, with background subtraction of OD at 650 nm, were measured using a Cary 50 spectrophotometer (Varian). Cell viability was expressed in % values (ΔOD: 570–650 nm) with respect to the control. All experiments were performed in triplicate.

Human glioblastoma cells (A172) (Chapter 6) were seeded into 96-well tissue culture plates at a concentration of $2x10^5$ cells per well. Cells were incubated at 37°C in a 5% CO_2 humidified atmosphere and maintained in the presence and absence of different concentrations (5, 10, 15, 20, µg/mL) of MIL for 24 h, using DMSO 0.5% and 1% as vehicle treated groups. Three hours before the end of the treatment time, 20 µL of 0.5% 3-(4,5-dimethylthiazol-2-yl)-2,5-diphenyltetrazolium bromide (MTT) in phosphate-buffered saline (PBS) was added to each microwell. After that, the supernatant was removed and replaced with 100 µL of DMSO to dissolve the formazan crystals produced.The amount of formazan is proportional to the number of viable cells present. The optical density value at λ = 570 nm was measured using a microplate spectrophotometer reader (Synergy HT, BioTek Instruments, Inc., Winooski, VT, USA). Cell viability was expressed in % values with respect to the control. All experiments were performed in triplicate.

2.6.2. Cellular Uptake

MNPs cellular uptake (Chapter 5) was studied combining Scanning Electron Microscopy (SEM) and Energy Dispersive X-Ray Analysis (EDX) measurements. After 24 h of pre-adhesion and after 72 h of incubation with the different kinds of nanoparticles, cells were fixed in 2% glutaraldehyde in 0.1 M sodium-cacodylate buffer (EMS), pH 7.2, for 1 h at 4°C and then post-fixed in 1% osmium tetroxide (EMS) for 1 h at 4 ◦C. After dehydration in graded ethanol and followed by Critical Point Drying using CO_2 (Emscope CPD 750), samples were mounted on stubs and sputter coated with gold. Sample morphologies were observed by field emission gun scanning electron microscopes (FE-SEM), using a ZEISS SUPRA VP 55 and a ZEISS EVO LS 10 (ZEISS, Oberkochen, Germany). Chemical analysis was performed by

energy dispersive X-ray (EDX) analysis using an INCA-Oxford windowless detector with an electron beam energy of 15 keV.

2.6.3. Intracellular Localization

To study the intracellular localization of magnetic nanoparticles (Chapter 5), Transmission Electron Microscopy (S-TEM Hitachi S7000 instrument, Hitachi, Tokyo, Japan) and Confocal Laser Scanning Microscopy (CLSM, Zeiss LSM700, Jena, Germany) were performed. For the TEM analysis, the cells were initially fixed and post-fixed as above mentioned for SEM analysis; the samples were then scraped, centrifuged (300× g/5 min) and the pellets dehydrated in ethanol/acetone and embedded in Durcupan ACM (Fluka). Ultra-thin sections were obtained by an Ultracut Reichert Jung instrument, collected on Cu-Rd grids (EMS) and stained with 5% uranyl acetate and 1% Pb citrate. Finally, the samples were observed and photographed. For CLSM experiments, LoVo cells were cultured on glass coverslips and after 24 h of pre-adhesion were incubated with FA-PEG@MNP and PEG@MNP (20 µg/mL) in the presence of NaBu (1 mM). Afterwards the cells were washed three times with phosphate-buffered saline (PBS). Samples were fixed in 4% paraformaldehyde (PFA) in PBS (15 min at room temperature), washed with PBS and mounted with Vectashield containing 4,6-Diamidino-2-Phenylindole, Dihydrochloride (DAPI) (Vector Laboratories, Inc., Burlingame, CA, USA).

2.6.4. High-Content Screening (HCS)

Human glioblastoma cells (A172) (Chapter 6) were seeded in 96-well plates (Cell Carrier™-96; PerkinElmer #6005550) at a density of $2x10^3$ cells per well. Nuclei were stained with NucBlue solution (NucBlue™ Live cell Stain, Thermo-Fisher Scientific #R37605) for 15 min at Room Temperature

(25°C) following the manufacturer's instructions (Thermo Fisher Scientific, Waltham, MA, USA).

After cell labelling for the nuclei, samples were washed three times in PBS and treated with DMSO, used as vehicle, and different MNPs concentrations (5, 10, 15, 20 µg/mL). Cells were imaged using the PerkinElmer Operetta High-Content Imaging System (# HH12000000). Plates were read under confocal conditions using the 63x long WD objective. A specific fluorescence type channel was used to acquire images of NucBlue (Ex: UV light, Em: 460 nm) for nuclei staining, shown in blue.

All images were analyzed using Harmony high-content imaging and analysis software (PerkinElmer, Waltham, MA, USA). Initial segmentation of cells was carried out in the DAPI channel by identifying the blue-stained nuclei with an area >30 µm. Finally, the number of spots per Area of Cytoplasm and Nucleus was expressed as mean per well.

Reference

1. Tudisco, C.; Cambria, M.T.; Sinatra, F.; Bertani, F.; Alba, A.; Giuffrida, A.E.; Saccone, S.; Fantechi, E.; Innocenti, C.; Sangregorio, C.; et al. Multifunctional magnetic nanoparticles for enhanced intracellular drug transport. J. Mater. Chem. B 2015, 3, 4134–4145.

2. Tudisco, C.; Cambria, M.T.; Giuffrida, A.E.; Sinatra, F.; Anfuso, C.D.; Lupo, G.; Caporarello, N.; Falanga, A.; Galdiero, S.; Oliveri, V.; et al. Comparison between folic acid and gH625 peptide-based functionalization of Fe_3O_4 magnetic nanoparticles for enhanced cell internalization. Nanoscale Res. Lett. 2018, 13, 45.

3. Lee, R.J.; Low, P.S. Delivery of liposomes into cultured KB cells via folate receptor-mediated endocytosis. J. Biol. Chem. 1994, 5, 3198–3204.

4. Du, P.D.; Thanh, H.T.M.; To, T.C.; Thang, H.S.; Tinh, M.X.; Tuyen, T.N.; Hoa, T.T.; Khieu, D.Q. Metal-Organic Framework MIL-101:

Synthesis and Photocatalytic Degradation of Remazol Black B Dye. J. Nanomater. 2019, 2019, 606127.

CHAPTER 3

Porphyrin on Bismuth Ferrite nanocrystals for enhanced solar light photocatalysis.

3.1. Introduction

In terms of pollution, industrialization has always had an adverse impact on the environment and the supply of drinking water. [1,2] According to United Nations reports, 2.2 billion people do not have access to potable water, which contributes to the deaths of 15 million children each year. [3,4]

Persistent Organic Pollutants (POPs) (synthetic dyes, pharmaceutical products, pesticides, endocrine disruptors, etc.) are one of the largest groups of pollutants found in urban wastewater. [5,6] This POPs cannot be effectively disposed of through traditional wastewater treatment using technologies that use biological, physical, or chemical approaches. [7] Because of this, research efforts have thus concentrated on developing new technologies to purify drinking water.

Many studies have been carried out on advanced oxidation processes (AOPs) [8,9] using photocatalytic chemical methods due to their total decomposition capacity of organic pollutants and convert them into inorganic compounds like H_2O, CO_2 and inorganic salts.

Several semiconductor systems have been adopted for photocatalytic degradation of organic pollutants thanks to their excellent absorption of ultraviolet radiation, their high photo-stability and their strong chemical stability. [10]

Although semiconductor materials (CdS, CdSe, ZnO, ZrO_2, TiO_2) are the most studied photocatalysts, [11] they have a number of limitations such as non-optimal excitation ranges and for some of them not negligible toxicity. [1,2]

In particular, many semiconductors are excited by ultraviolet light due to their wide band and because of that, they use only about 5% of the incoming solar energy. [1,3]

For this reason, the development of visible light photocatalysts has recently become an important research topic. In recent years, multiferroic materials in which ferroelectricity, ferromagnetism and ferroelasticity coexist have gained much attention for applications such as photovoltaic, photocatalytic and phototransducer devices. [14,15] The great consideration for the above applications comes from their intrinsic electric polarization because of their inversion-symmetry-breaking. [16]

The excitation induced by light produces electron-hole pairs and their polarization acts as an internal electric field promoting the separation of these charge carrier. [17]

Among the multiferroic materials, the perovskite bismuth ferrite ($BiFeO_3$, BFO), is a promising photocatalyst for wastewater treatments due to its small band gap (about 2.3 eV) [18] makes it possible to exploit a larger range of the spectrum of sunlight than other semiconductor photocatalysts. However, the reported photocatalytic activity of pure BFO is low because of the fast recombination of the photogenerated electron-hole pairs. [19] Consequently, a number of strategies have been implemented to improve the photocatalytic activity of BFO, such as doping, [10,17,20] coupling with narrow-band semiconductors [21-24] and surface modifications. [25]

Photosensitizing with organic dye molecules is one of the most effective and widely used approaches to improve the photocatalytic performance of semiconductor photocatalysts. [26]

Porphyrins, phthalocyanins and dyes such as D149 and N179 were tested as sensitizing agents in order to improve the photocatalytic performance of semiconductor photocatalysts, because of their strong absorption in the visible light region. Moreover, they are excellent electron donors thanks to their large π-electron conjugated systems capable of electron injection. [27-30]

However, some porphyrines do not interact with the surface of the photocatalyst due to the lack of an appropriate anchor group. In this case, electron transfer may not occur, leading to lower photocatalytic efficiency. [31]

The formation of a strong covalent bond between the photocatalyst and the porphyrin may act as a channel for electron transfer, [32] that facilitates the injection of electrons from excited porphyrins to the BFO conducting band.

Modifying semiconductors with porphyrins is a widely adopted method for enhancing the photocatalytic performance of these materials, [33] but, to our knowledge, this approach has not been tested using BFO-based materials.

In view of the remarkable properties of porphyrins, the combination of porphyrins and BFO can be an ideal strategy for constructing effective photocatalytic systems.

In this chapter, multiferroic bismuth ferrite (BFO) was functionalized with meso-Tetraphenylporphine-4,4′,4″,4‴-tetracarboxylic acid (TCPP).

In addition to the already mentioned strong absorption in the visible light region and to the large π-electron conjugated systems typical of all porphyrins, this molecule has four carboxylic groups able to anchor metal oxides. A specific synthetic procedure to bond the BFO surface was recently developed in our group. [34] The novel hybrid organic-inorganic material

exhibits improved photocatalytic activity to degrade of organic dyes because it combines the properties of BFO that is effective visible light photocatalyst with the peculiar porphyrin absorption in the visible light.

Two organic dyes, methylene blue (MB) and Rhodamine B (Rhd-B) were used to test the photocatalytic performance of BFO@TCPP, under simulated solar radiation. [35-37]

Furthermore, the impact of pH on the photodegradation process as well as on the stability and recyclability of the photocatalyst was also examined.

3.2. Results and Discussion

The synthetic pathway developed to obtain the BFO@TCPP is illustrated in Fig.3.1. It consists of a multi-step approach: the first step was the synthesis of BFO particles by sol-gel method, followed by surface activation with hydrogen peroxide (H_2O_2) at 100 °C.

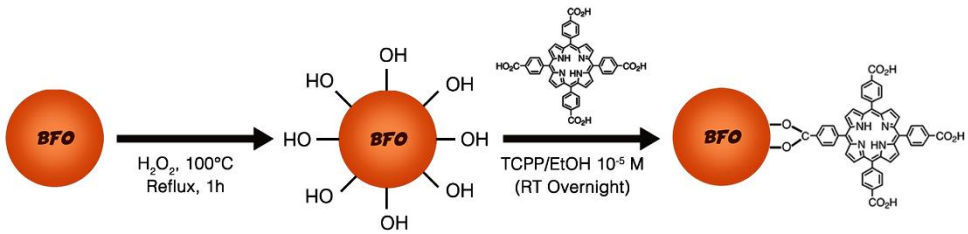

Fig.3.1. Schematic representation for the anchoring of TCPP on Bismuth ferrite

The activated particles (BFO-H_2O_2) were then treated with a TCPP solution to anchor the photosensitizing agent to the activated surface through its carboxylic fractions.

Fig. 3.2a and 3.2b present the SEM images, which reveal the morphology of the obtained BFO and BFO@TCPP powders. According to the figures, it can be noticed how the observed particles are uniform with a

rather narrow dimensional distribution with average particle size of the two samples is between 150 and 200 nm.

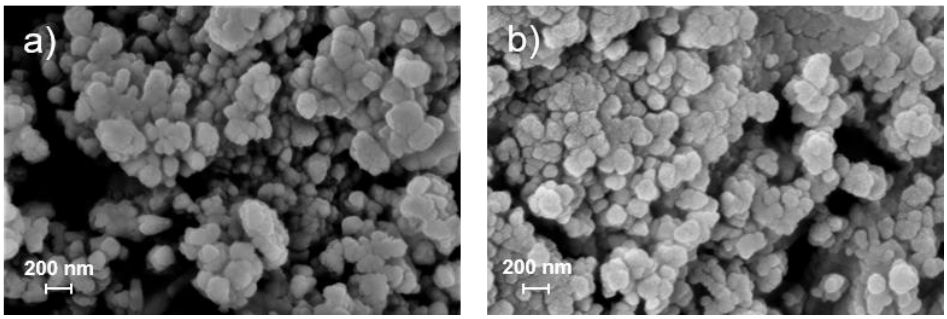

Fig.3.2. SEM images of a) bare BFO and b) TCPP@BFO powders.

The XRD measurements were performed to characterize the crystalline structure of the calcined powders. As can be seen from the comparison of the BFO XRD patterns before and after the functionalization process on Fig.3.2a and 3.2b respectively, all of them can be indexed to the perovskite rhomboidal structure (space group: R3c), in good agreement with the powder data of the JCPDS card number 20-169.

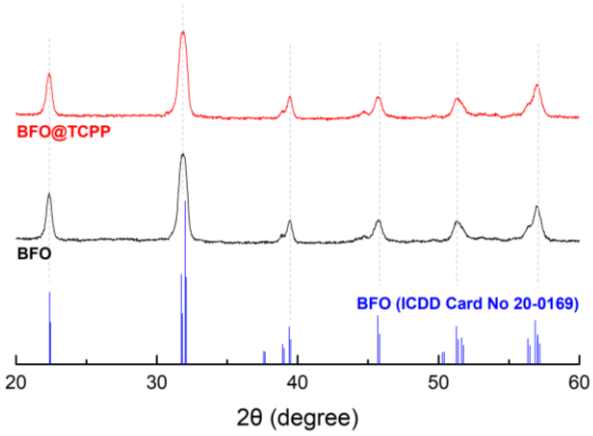

Fig.3.3. XRD patterns of bare BFO (black line) and TCPP-functionalized BFO (red line) powders. The simulated spectrum calculated from ICDD data (Card No 20-0169) was added at the bottom (blue line).

This finding proves that the anchoring process occurs without the degradation of the BFO structure.

BFO and BFO@TCPP thermal behaviors have been characterized by TGA. In particular, the TGA curve for the naked BFO shows (Fig. 3.4) that the weight of the sample remains constant throughout the temperature range, except for small single weight loss steps at 120 ºC (about 0.2%), caused by evaporation of the adsorbed solvent attached to the particle surfaces. The TGA curve of BFO@TCPP has two stages of weight loss. Similarly observed for pure BFO, the first mass loss (around 120 ºC) is due to physisorbed solvents, while the second mass loss, observed in the temperature range 200-400 ºC, (about 0,8 %) is the result of the decomposition of porphyrin. From the comparison of the two curves, it is possible to determine with good approximation that the quantity of molecules of TCPP grafted on the particles of BFO is about 8 mg/g.

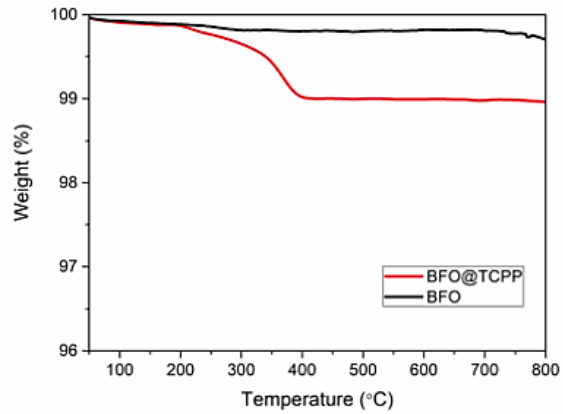

Fig.3.4. TGA curves of bare BFO (black line) and TCPP-functionalized BFO (red line) powders.

The surface areas of the two samples were estimated through BET analysis. As shown in Figure 3.5a and 3.5b the adsorption isotherms N_2 show that the surface area of the samples, before and after the functionalization, are

respectively 5 and 4 m^2/g and the corresponding pore volumes are 0,028 cm^3/g and 0,011 cm^3/g.

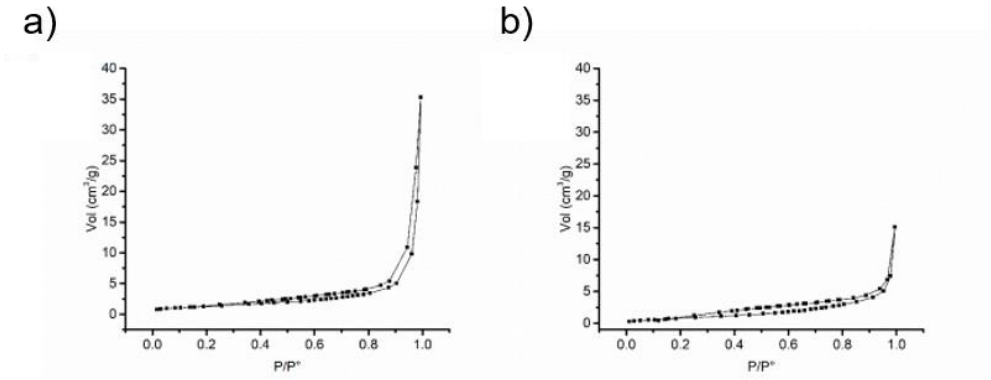

Fig.3.5. N_2 adsorption isotherms of (a) BFO and (b) TCPP@BFO powders.

After each functionalization step, the BFO samples were characterized through X-ray photoelectron spectroscopy (XPS) and FT-IR spectroscopy. Table 1 reports the atomic surface composition of bare BFO, BFO-H_2O_2 and BFO@TCPP. The Bi/Fe atomic ratio (about 1.4) of the BFO surface is slightly higher than the expected stoichiometric value as often found in annealed BFO particles. [34] This ratio becomes much higher (about 6) after the H_2O_2 activation step due to the Bi segregation towards the surface as previously reported. [34]

After the anchoring process, the atomic surface ratio Bi/Fe does not change, confirming the XRD findings that the functionalization process does not affect the structure of the BFO. On the other hand, the increment of the C 1s intensity and the presence of N 1s signals after the TCPP anchor are reliable indications of the presence of TCPP molecules on the BFO surface.

The changes in the XPS bands O1s and C1s (Fig.3.6) after each reaction stage clearly show the surface modifications. The O1s region of bare BFO particles is composed of two bands centered at 530.1 eV and 532.3 eV

which are associated to lattice and chemisorbed oxygen atoms, respectively. [21]

	BFO	**BFO-H_2O_2**	**BFO@TCPP** as prepared	**BFO@TCPP** after photocatalysis	
				pH 7	pH 3
Bi 4f	12.9	21.0	6.5	7.4	8.3
Fe $2p_{3/2}$	9.4	3.6	1.2	1.3	1.6
C 1s	30.8	31.6	67.4	65.3	56.3
N 1s	.	-	3.6	3.4	3.5
O 2p	46.9	44.1	21.3	22.6	28.1
Bi/Fe	1.4	5.8	5.4	5.7	5.1

*Table 1. XPS atomic percentage of BFO, as-prepared TCPP@BFO and TCPP@BFO particles after the photocatalytic processes at pH 7 and 3. *XPS analysis also showed the presence of about 1% of Cl atoms due to the HCl used to decrease pH to 3.*

After the activation step with H_2O_2, the intensity of the band centered at 532.3 eV increases due to generating –OH groups on the surface. This band at 532.3 eV is significantly higher in the TCPP@BFO spectrum because of the presence of the carboxylic and carboxylate groups of TCPP.

XPS C1s bands of BFO and BFO@TCPP (Fig.3.6) show significant differences. As regards the bare BFO, it consists of a main component centered at 285.0 eV due to the "adventitious" carbon [39,40] and a shoulder at 286.6 eV due to oxidized carbon contaminants.

After TCPP grafting, not only the intensity of the C1s band is increased (Table 1), but also its shape (Fig.3.6. bottom) is different from the analogue bands of naked BFO. This band is made up of three components. The first one, found at 285.0 eV, is due to both the aromatic carbon atoms of TCPP and the "adventitious" carbon. The second one, found at 286.6 eV, is due to the C-N of the porphyrin ring and to the oxidized carbon contaminants. The

third component, which is not present in the spectra of bare BFO is centered at 288.6 eV can be assigned to the four carboxylic/carboxylate moieties of the grafted TCPP molecules. [42,43]

In addition, the observed B.E. value (288.6 eV) of the third component is lower than that one expected for free carboxylic acids [34,41,42] and physisorbed TCPP molecules.

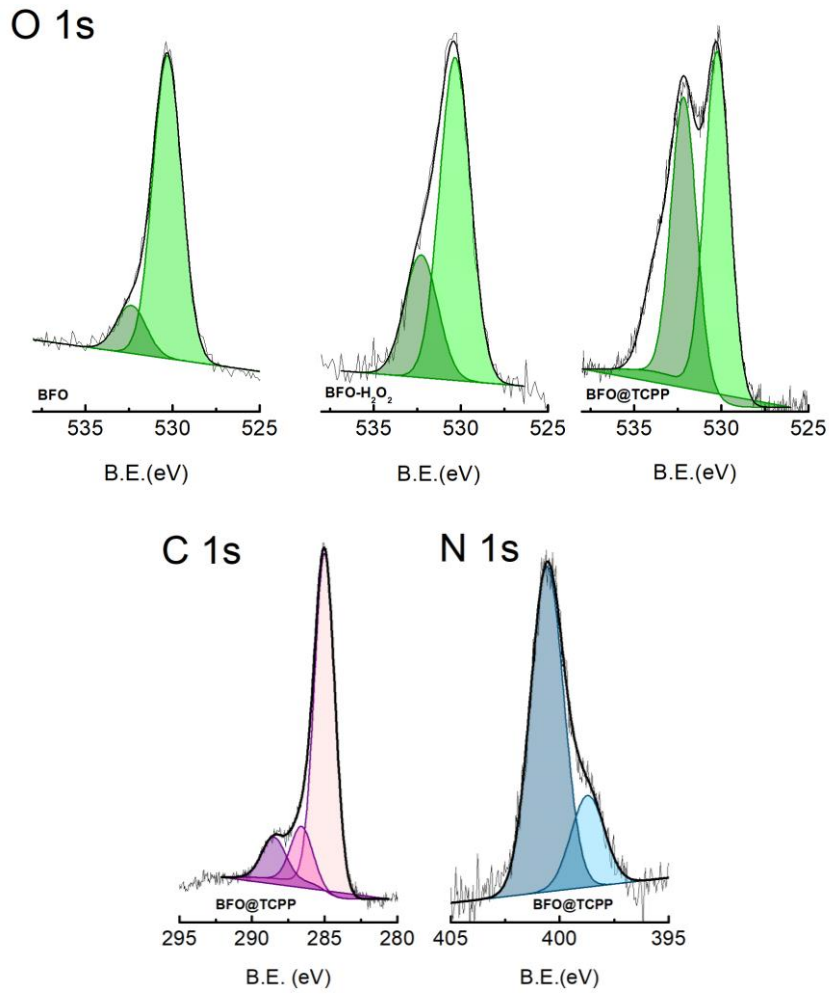

Fig.3.6. O1s XPS spectral region of as-synthetized BFO (left), BFO-H_2O_2 (middle) and BFO@TCPP (right). C1s (left) and N1s (right) XPS spectral regions of BFO@TCPP (bottom).

This suggests that TCPP molecules are not physisorbed on BFO, but the TCPP carboxylic moieties interact with the surface of BFO through deprotonation and formation of C-O-M bonds (with M=Bi or Fe). [34]

The XPS N 1s signal of the TCPP@BFO is reported in Fig.3.6. This band shows two features: a main peak which is centred at 400.5 eV and a shoulder located at 398.7 eV. The band shapes suggest the presence of at least two species of nitrogen atoms and the B.E. values, located in the range reported for pyrrolic (-NH-) and iminic (-N=) nitrogen species, are typical of the porphyrinic tetrapyrrolic ring. [41, 44-46]

The FT-IR analysis for BFO and TCPP@BFO confirmed that TCPP is anchored through the carboxylic groups, as is showed in Fig.3.7.

In particular, although the band at 1690-1710 cm^{-1} is typical of the C=O stretching of the free carboxylic moieties are is still present, two strong bands in the 1610-1520 range and at 1390-1430 cm^{-1} typical of the asymmetric and symmetric $\nu(COO^-)$ stretches of carboxylate groups are also present. [48-51]

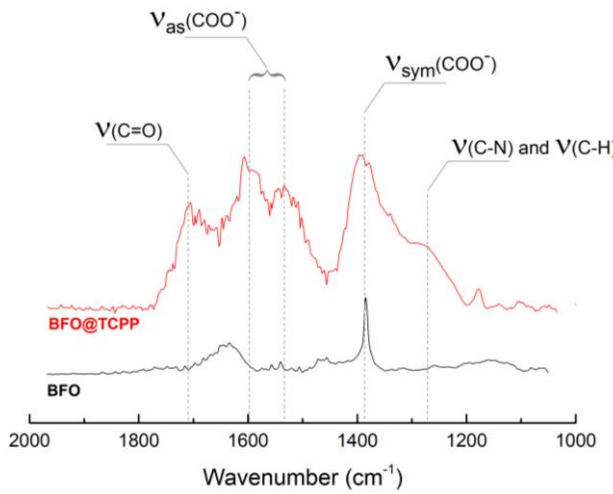

Fig.3.7. FTIR spectra in the 2000-1000 cm^{-1} range of bare BFO (black line) and BFO@TCPP (red line).

The presence of these bands and the absence of the analogous peaks in the bare BFO spectra indicate the success of TCPP anchorage through carboxylate groups. The C=C, C-C and C-N stretching signals of the porphyrin ring (also these in the range 1600-1400 and 1300-1200 cm^{-1} respectively) are not clearly observable because they are overlapped by the stronger ν(COO^-) bands. [48] Note that the narrow peak at 1400 cm^{-1} in the IR spectrum of the bare BFO has a different shape than the broad ν(COO^-) signal. The sharp signal in BFO is attributable to the presence of impurities of sodium carbonate in KBr.

The photocatalytic performance of the obtained photocatalysts was evaluated by the photocatalytic degradation study of MB and Rhd-B dyes under simulated sunlight irradiation.

Fig. 3.8 shows the evolution of the residual concentrations of MB (Fig. 3.8a) and Rhd-B (Fig. 3.8b) versus with the illumination time. In each graph, C indicates the dye concentration (MB or Rhd-B) at time t, while C_0 is the initial dye concentration.

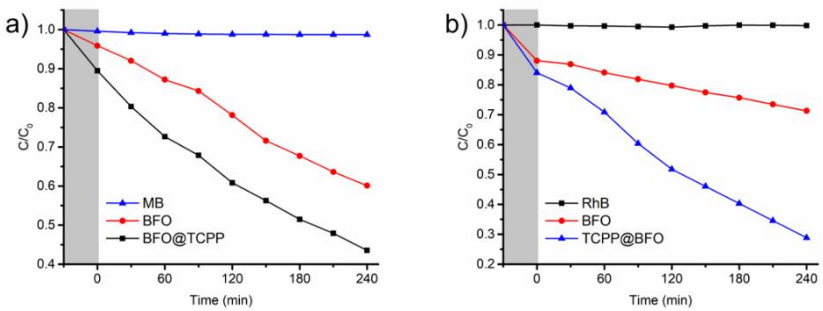

Fig.3.8. MB (a) and Rhd-B (b) dyes photo-degradation under simulated solar light irradiation (50 mW/cm^2) for three aqueous solutions (pH=7) with pure dye (blue triangles), dye with BFO particles (red circles) and dye with BFO@TCPP particles (black squares).

The change of dye concentrations is negligible during the whole irradiation time, when no photocatalyst is added. In particular, bare BFO particles lead to approximately 40% degradation for MB and 30%

degradation for Rhd-B after 240 min irradiation, whereas BFO@TCPP particles determine a significant increase in the degradation efficiency (about 60% for MB and 70% for Rhd-B) over bare BFO. These results demonstrate the significant role of porphyrin in improving the catalytic performance of BFO.

The UV–vis DRS of pure BFO and TCPP@BFO are illustrated in Fig.3.9. The band-gap energy of the two systems was computed using Tauc's equation, [52] and can be fitted as a graph of $(\alpha h\nu)^2$ versus photo energy ($h\nu$) in the inset of Fig.3.9. The band-gap energy for pure BFO was estimated to be approximately 2.30 eV, which is similar to the other reported values. [18] The calculated band-gap energy of BFO@TCPP was 2.24 eV, which is less than the of bare BFO particles. These results suggest that the functionalization with the TCPP favors the absorption of visible light and thus promotes the full use of the solar energy.

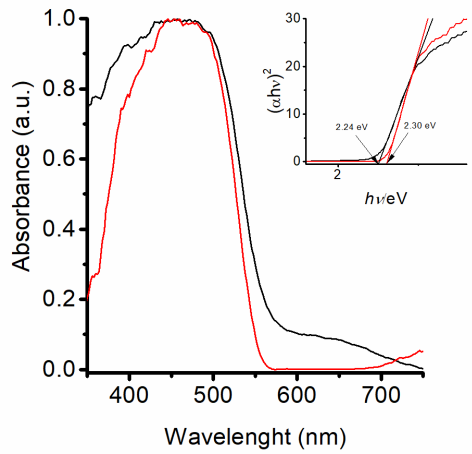

Fig.3.9. UV–vis DRS spectrum of BFO (red line) and BFO@TCPP (black line); inset shows calculation of the band gap of both systems.

The stability of the photocatalyst is a crucial factor for its practical application. In order to verify the stability of the TCPP@BFO composite,

cyclic tests of photocatalytic degradation of the MB were carried out under simulated sunlight. After four cycles, as shown in Fig.3.10, the photocatalytic activity of BFO@TCPP is virtually unchanged, which indicates that the composite is an efficient and stable photocatalyst under simulated solar light.

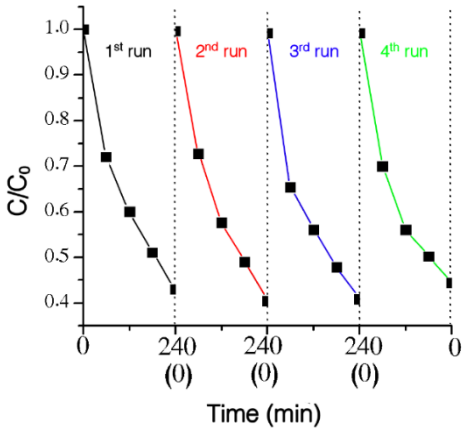

Fig.3.10. Stability test of TCPP@BFO after 4 cycles of MB decolouration.

The pH of the aqueous solution is one of the main operating parameters that affect the heterogeneous photocatalysis process, because it influences the surface charge of the photocatalyst and the position of the conductance and valence bands. In addition, the pH of industrial wastewater can be acidic or basic, so the pH effect should be considered. Therefore, a series of MB photocatalytic degradation experiments were conducted at several pH values: 3, 7 and 12. Fig.3.11 demonstrates that the photocatalytic performance increases at higher pH and decreases at acidic pH (pH=3). The positive impact of high pH values on catalytic performance is probably due to the high concentration of hydroxyl ions, which make photogeneration of hydroxyl radicals easier. On the other hand, at low pH (pH=3), the low quantity of hydroxyl ions and the possible dissolution of BFO may reduce the degradation efficiency (note that no evidence of desorption of TCPP from the surface was found under the pH conditions investigated).

However, to provide further evidence of the stability of the TCPP layer anchored to the BFO surface, XPS analysis of BFO@TCPP particles was carried out after photocatalytic processes at pH 7 and pH 3.

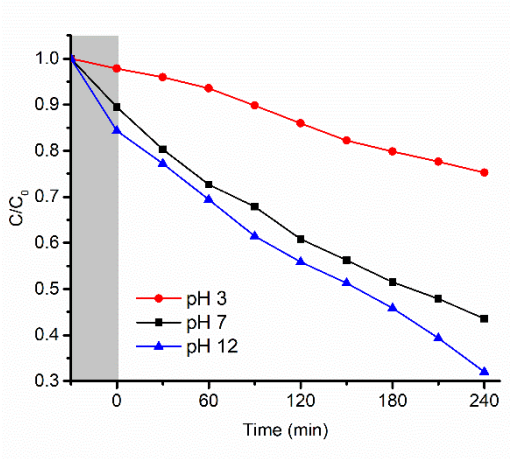

Fig.3.11. MB photo-degradation under simulated sun light irradiation by TCPP@BFO in MB aqueous solution with different pH: 3 (red circles), 7.5 (black squares), and 12 (blue triangles).

The C 1s and N 1s peak shapes of the samples analysed after the photocatalytic processes (unreported) are both similar to the C 1s and N 1s peaks of the as prepared samples, which indicates that TCPP molecules are still anchored on the BFO surface. Furthermore, the atomic percentage of N is also similar before and after photocatalytic processes at pH 7 and 3 (Table 1). As the N 1s peak shape indicates that the observed N is due to the four nitrogen atoms in the TCPP ring, it may be assumed that the N percentage is proportional to the amount of TCPP grafted. As a result, the data in Table 1 suggest that grafted TCPP molecules do not desorb during photocatalysis, even at pH 3.

To obtain information about the photodegradation mechanism catalysed by TCPP@BFO particles, the effect of the presence of 2-propanol (an OH• radical scavenger) was evaluated. Fig.3.12 compares the residual Rhd-B

concentration after 120 minutes of irradiation in the presence of 4 different catalyst/scavenger combinations: i) TCPP@BFO (1 mg/ml), ii) TCPP@BFO (1 mg/ml) and 2-propanol ($2x10^{-3}$ M), iii) free TCPP (0.1 mg/ml) and iv) free TCPP (0.1 mg/ml) and 2-propanol ($2x10^{-3}$ M).

It can be seen from the figure that 2-propanol severely degrades the catalytic performance of catalysts TCPP@BFO and pure TCPP, indicating that in both cases, OH• radicals play a critical role in the photodegradation process.

From the above results, a tentative mechanism for the catalytic process BFO@TCPP is proposed (Fig.3.13). The estimated BFO valence (VB) and conduction (CB) bands edge potentials versus the normal hydrogen electrode (NHE) are 2.64 V and 0.4 V respectively. [53,54] The TCPP ground and excited singlet states redox potential versus NHE are 0.96 V and -1.36 V respectively. [55,56]

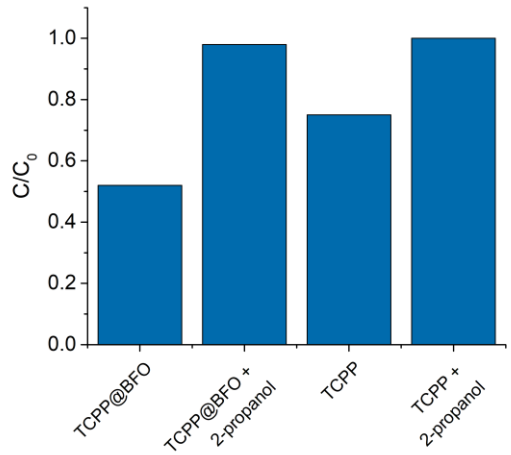

Fig.3.12. Comparison of the residual concentration of Rhd-B after a 120 min irradiation in the presence of 4 different catalyst/scavenger combinations: i) BFO@TCPP (1 mg/ml), ii) BFO@TCPP (1 mg/ml) and 2-propanol ($2x10^{-3}$ M), iii) free TCPP (0.1 mg/ml) and iv) free TCPP (0.1 mg/ml) and 2-propanol ($2x10^{-3}$ M).

When the BFO@TCPP catalyst is exposed to visible light, the BFO semiconductor and the TCPP molecules can be excited. The BFO VB redox potential (2.64 V) is higher than the $OH^{\bullet}/OH^{-}$ standard reduction potential (1.9 V). [57] As a result, the VB holes (h+) are reduced by OH^{-} producing $OH^{\bullet}$ radicals that trigger dye degradation.

On the other hand, the formation of superoxide radicals from excited electrons in the BFO CB is not favored, due to the $O_2/O_2^{\bullet}$ redox potential (-0.33 V) [57] is lower than the CB potential (0.4 V). However, superoxide radicals may be formed by excited TCPP, which has a redox potential (-1.36 V) that is less than $O_2/O_2^{\bullet}$. Superoxide radicals can either degrade pollutants directly or, more likely, generate OH radicals, which in turn degrade pollutants.

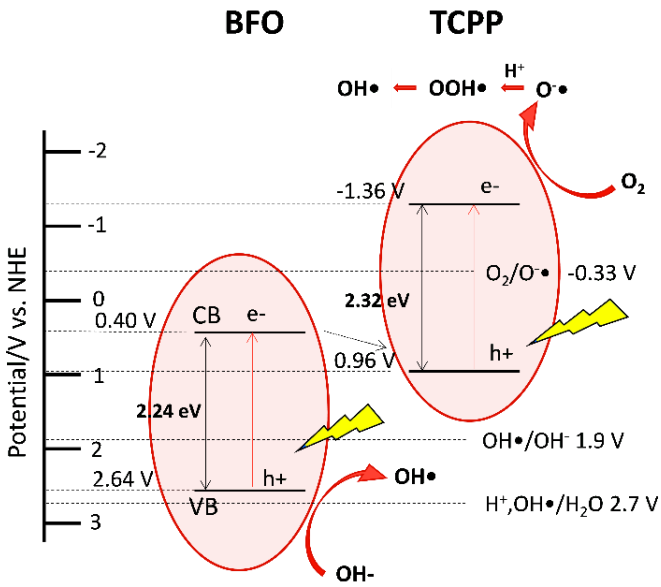

Fig.3.13. Diagram reporting the potentials of TCPP ground and excited singlet states and of the BFO conduction and valence bands versus the normal hydrogen electrode (NHE) and a schematic mechanism for the TCPP@BFO catalytic process.

This second pathway is consistent with the findings presented in Fig.3.12, which indicate that $OH^{\bullet}$ radicals are the active species that participate in the decomposition of the dye in the presence of TCPP@BFO or free TCPP.

3.3. Conclusions

In this chapter, bismuth ferrite (BFO) particles were prepared using a sol-gel method and functionalized with meso-Tetraphenylporphine-4,4′,4″,4‴-tetracarboxylic acid.

XRD characterization demonstrated that the functionalization protocol does not affect the structure of the catalyst.

The combination of TGA, XPS and FT-IR confirms that BFO particles have been successfully modified with porphyrin TCPP.

In particular, our findings demonstrate that the functionalization process occurs through the anchoring of the TCCP carboxylic groups to the OH activated BFO surface resulting in the deprotonation of the tethering carboxylic groups.

The functionalization with TCPP alters the BFO band-gap from 2.30 eV for pure BFO to 2.24 eV for the functionalized one, in this way, BFO adsorption and, in turn, catalytic efficiency under solar irradiation are improved. Furthermore, anchored TCPP molecules can also be catalytic centers, which further increases the photocatalytic activity of the combined BFO@TCPP catalyst.

Indeed, after 240min of irradiation, in the case of pure BFO, the residual quantities of MB and Rhd-B were 60% for MB and 70% for Rhd-B, while for BFO@TCPP it has decreased to 40% for MB and 30% for Rhd-B.

In addition, cyclical experiments (4 cycles) have proven that this new hybrid photocatalyst is reusable and stable in water.

Moreover, the influence of pH conditions has been tested showing that the photocatalytic performance of the decorated BFO improves when the pH is increased to 12.

Experiments using 2-propanol as a radical scavenger have demonstrated that OH• radicals play a key role in the degradation process and a tentative mechanism has been suggested.

Our study proposes a new method for preparing functionalized porphyrin BFO photocatalysts, which can be very effective for degrading dyes in water, or for treating industrial wastewater.

Additionally, the proposed BFO surface modification approach does not impact the ferroelectric/piezoelectric properties of the material, [33] thus paving the way for possible multifunctional systems combining environmental control and piezo-electric energy harvesting.

References

1. M. A. Shannon, P. W. Bohn, M. Elimelech, J. G. Georgiadis, B. J. Marinas and A. M. Mayes, Nature, 2008, 452, 301–310.

2. S. Bolisetty, M. Peydayesh and R. Mezzenga, Chem. Soc. Rev., 2019, 48, 463.

3. World Health Organization https://www.who.int/newsroom/detail/28-08-2019-weak-systems-and-funding-gapsjeopardize-drinking-water-and-sanitation-in-theworld%E2%80%99s-poorest-countries (accessed August, 2019).

4. United Nations: https://www.un.org/en/sections/issuesdepth/water/index.html (accessed May 2019).

5. J. Margot, C. Kienle, A. Magnet, M. Weil, L. Rossi, L. F. de Alencastro, D. Thonney, N. Chèvre, M. Schärer and D. A. Barry, Sci. Total Environ., 2013, 461, 480.

6. R. P. Schwarzenbach, et al., Science, 2006, 313, 1072–1077.

7. S. Bagheri, A. Termeh Yousefi, T. O. Do, Catal. Sci. Technol., 2017,7, 4548.

8. J.L. Wang, L.J. Xu, Critical Reviews in Environmental Science and Technology, 2012, 42, 251.

9. I. O. Oribe, A. Mosquera-Corral, J. L. Rodicio, S. Espluges, AIChE, 2015, 61, 3146.

10. N. Zhang, D. Chen, F. Niu, S. Wang, L. Qin and Y. Huang, Sci. Rep., 2016, 6, 26467.

11. L. Q. Jing, W. Zhou, G. H. Tian and H. G. Fu, Chem. Soc. Rev., 2013, 42, 9509.

12. L. Wang, D. K. Nagesha, S. Selvarasah, M. R. Dokmeci and R. L. Carrier J. bionanotechnology, 2008, 6, 11.

13. L. V. Bora, R. K. Mewada, Renewable and Sustainable Energy Reviews, 2017, 76, 1393-1421.

14. J. Kreisel, M. Alexe and P. A. Thomas, Nat. Mater., 2012, 11, 260.

15. F. Gao, X. Y. Chen, K. B. Yin, S. Dong, Z. F. Ren, F. Yuan and J. M. Liu, Adv. Mater., 2007, 19, 2889.

16. S. M. Young, A. M. Rappe, Phys. Rev. Lett., 2012, 109, 116601.

17. S.Irfan, S. Rizwan, Y. Shen, L. Li, S. Butt and C. W. Nan, Sci. Rep., 2017, 7, 42493.

18. S. V. Pavana, C. Mocherla, R. Karthik, M. S. Ubic, R. Ramachandra and C. Sudakar, Appl. Phys. Lett., 2013, 103, 022910.

19. I. Papadas, J. A. Christodoulides, G. Kioseoglou, and G. S. Armatas, J. Mater. Chem. A, 2015, 3, 1587.

20. S.Irfan, L. Li, A. S. Saleemi and C. W. Nan, J. Mater. Chem. A, 2017, 5, 11143.

21. Y. H. Si, Y. Xia, S. K. Shang, X. B. Xiong, X. R. Zeng, J. Zhou and Y. Y. Li, Nanomaterials, 2018, 8, 526.

22. X. Wang, W. Mao, J. Zhang, Y. Han, C. Quan, Q. Zhang, T. Yang, J. Yang, X. Li, W. Huang, J. Colloid. Interface Sci.,2015, 448, 17.

23. T. Soltani, B.-K. Lee, Chem. Eng. J., 2016, 306, 204.

24. Z. Li, Y. Shen, C. Yang, Y. Lei, Y. Guan, Y. Lin, D. Liu and C.W. Nan J. Mater. Chem. ,2013, 1, 823.

25. X. G. Zhang, B. Wang, X. Z. Wang, X. H. Xiao, Z. G. Dai, W. Wu, J. F. Zheng, F. Ren and C. Z. Jiang, J. Am. Ceram. Soc., 2015, 98, 2255.

26. Z. Zhang, H. Liu, J. Xu, N. Zhang, Photochem. Photobiol. Sci., 2017, 16, 1194.

27. S. Radhica, J. Thomas, J. Envir. Chem. Eng., 2017, 5,4239.

28. S. Afzal, W. A. Daoud, and S. J. Langford, ACS Appl. Mater. Interfaces, 2013, 5, 4753.

29. Y. Cho, W. Choi, C. H. Lee, T. Hyeon and H. I. Lee, Environ. Sci. Technol., 2001, 35, 966.

30. M. A. Ahmed, Z. M. Abou-Gamra, H. A. A. Medien and M. A. Hamza, Journal of Photochemistry & Photobiology B: Biology, 2017, 176, 25.

31. L. Zhang, J. M. Cole, ACS Appl. Mater. Interfaces, 2015, 7, 3427.

32. L. G. Devi, M. L. ArunaKumari, B. G. Anitha, R. Shyamala and G. Poornima, 2016, Surf. Interf., 1, 52.

33. ZHU, Kun, et al. A novel copper-bridged graphitic carbon nitride/porphyrin nanocomposite with dramatically enhanced photocatalytic hydrogen generation. Applied Catalysis B: Environmental, 2020, 268: 118434.

34. C. Tudisco, A. L. Pellegrino, G. Malandrino and G. G. Condorelli, Surf. Coat. Technol., 2018, 343, 75.

35. M. Hassanpour, H. Safardoust-Hojaghan, M. Salavati, Niasari, J. Mol. Liq., 2017, 229, 293.

36. D. Mitoraj, U. Lamdab, W. Kangwansupamonkon, M. Pacia, W. Macyk, N. Wetchakun, R. Beranek J. Photochem. Photobiol. A, 2018, 366, 103.

37. W. Li, D. Li, S. Meng, W. Chen, X. Fu, and Y. Shao Environ. Sci. Technol., 2011, 45, 2987.

38. T. Poursaberi, M. Hassanisadi, K. Torkestani and M. Zare, Chemical Engineering Journal, 2012, 189, 117.

39. I. L. Swift, Surf. Interface Anal. 1982, 4, 47.

40. D. Briggs, G. Beamson, Anal. Chem. 1992, 64, 1729.

41. G. Pellegrino, G. G. Condorelli, V. Privitera, B. Cafra and A. Alberti, J. Phys. Chem. C, 2011, 115, 7760.

42. S. Fleutot, J.-C. Dupin, G. Renaudin, H. Martinez, Phys. Chem. Chem. Phys., 2011, 13, 17564.

43. X. Guan, G. Chen and C. Shang, J. Environ. Sci., 2007, 19, 438.

44. H. Tian, J. Oscarsson, E. Gabrielsson, S. K. Eriksson, R. Lindblad, B. Xu, Y. Hao, G. Boschloo, E. M. J. Johansson, J. M. Gardner, A. Hagfeldt, H. Rensmo and L. Sun, Sci. Rep. 2014, 4, 4282.

45. C. S. Gopinath, R. P. Pandian, and P. T. Manoharan, J. Chem. Soc., Dalton Trans., 1996, 1255.

46. J. R. Eskelsen, Y. Wang, Y. Qui, M. Ray, M. Handlin, K.W. Hipps and U. Mazur, J. Porphyrins Phthalocyanines, 2012, 16, 1233.

47. K. Lewandowska, N. Rosiak, A. Bogucki, J. Cielecka-Piontek, M. Mizera, W. Bednarski, M. Suchecki and K. Szaciłowski, molecules, 2019, 24, 688.

48. K. Nakamoto, Infrared and Raman Spectra of Inorganic and Coordination Compounds, John Wiley & Sons, Inc., New York, USA, 1978.

49. J. Roales, J. M. Pedrosa, M. G. Guillén, T. Lopes-Costa,P. Castillero, A. Barranco and A. R. González-Elipe Sensors 2015, 15, 11118

50. G. Granados-Oliveros, F. Martínez Ortega, E- Páez-Mozo, C. Ferronato and J.-M. Chovelon Open Mater. Sci. J., 2010, 4, 15.

51. A. J. Said, G. Poize, C. Martini, D. Ferry, W. Marine, S. Giorgio, F. Fages, J. Hocq, J. Boucle´, J. Nelson, J. R. Durrant and J. Ackermann J. Phys. Chem. C, 2010, 114, 11273.

52. D.A. Chang, P. Lin, T.Y. Tseng, J. Appl. Phys., 1995, 77, 4445.

53. S. Li, Y.-H. Lin, B.-P. Zhang, J.-F. Li, and C.-W. Nan J. Appl. Phys. 2009, 105, 054310

54. J. Shang, H. Chen, T. Chen, X. Wang, G. Feng, M. Zhu, Y. Yang, X. Jia, Appl. Phys. A, 2019, 125, 133.

55. C. E. Diaz-Uribe, M. C. Daza, F. Martínez, E. A. Páez-Mozo, C.L.B. Guedes, E. Di Mauro J. Photochem. Photobiol. A, 2010, 215, 172.

56. A. Kathiravan, R. Renganathan, J. Colloid. Interface Sci.,2009, 331, 401.

57. B.H.J. Bielski, D.E. Cabelli, in Active Oxygen in Chemistry. Structure Energetics and Reactivity in Chemistry Series (SEARCH Series) vol 2, ed. C.S. Foote, J. S. Valentine, A. Greenberg, J. F. Liebman, Springer, Dordrech 1995, chapter 3, p. 66-104.

CHAPTER 4:

Enhancement of the visible light photo-induced antibacterial activity of $BiFeO_3$ nanocrystals by surface modification with MIL-101.

4.1. Introduction

Antibiotic resistance is a critical challenge for modern medicine. [1,2] Many are the pathogens responsible for serious infections and diseases, which can lead to the death of the affected patient. Efficient strategies are therefore needed to obtain advanced molecules to control bacterial infections that are a serious threat to human health. [3]

Several photoactive materials have been extensively studied for their antimicrobial properties, [4,5] which are enhanced because of photo exposure. The irradiation of optical-active compounds causes the production in large quantities of various reactive oxygen species (ROS). ROS exert antimicrobial activity, managing to attack a wide range of cellular targets, causing oxidative damage to DNA, lipids, proteins and other cellular components. [6,7] The result is an extensive cellular damage leading to microbial cell death. Bacteria can counteract low levels of ROS via endogenous antioxidant defences, [8] including catalase enzymes, peroxidases and superoxide dismutase, which aim to remove superoxide radicals and hydrogen peroxide. However, when excessive production of ROS occurs, the intracellular redox state is modified, resulting in oxidative stress and attack on lipids and various membrane constituents. The integrity of the bacterial membrane is thus altered, facilitating the cell penetration of various reactive species, and, in

turn, resulting in DNA damage and cell death. [9] However, these photoactive materials must be irradiated with a very intense visible light source or UV radiation to be truly efficient. [10,11] This result is not always easy to achieve, and scientific research is directing towards the design and implementation of materials that are able to perform their action even under mild exposure conditions.

In this chapter is reported a novel synthetic strategies adopted to the growth of carboxylate-based MOF (MIL-101) on BFO nanoparticles surface.

The MILs are a family of metal organic frameworks formed by the assembly of trivalent clusters of Fe^{3+} and 2-aminoterephthalic acid as organic ligand. [12,13]

As previously written, the BFO is a material with promising optical properties, [14,15] limited by the rapid recombination of its charge carriers. The aim of the modified system is to increase the photoactive (both antibacterial and catalytic) properties of BFO and retain its nanoscale dimensions.

In order to understand the effect of MOF growth time process, was performed a synthesis at different times. In particular, here we report the comparison between two sample (BFO@MIL[a] and BFO@MIL[b]), the first left to react for 2h and the second for 4h.

BFO@MIL-101 was applied as an anti-bacterial material [16-18] under natural sunlight radiation against several bacterial strains of Staphylococcus Aureus, Staphylococcus Haemolyticus and Escherichia Coli.

4.2. Results and Discussion

The adopted method for the synthesis of MOF-functionalized Bismuth Ferrite nanoparticles (BFO) is schematized in Fig.4.1.

The adopted pathway has as a key point the use of BFO inorganic nanoparticles as both Fe^{3+} ion source and nucleation center for the growth of the MIL structure.

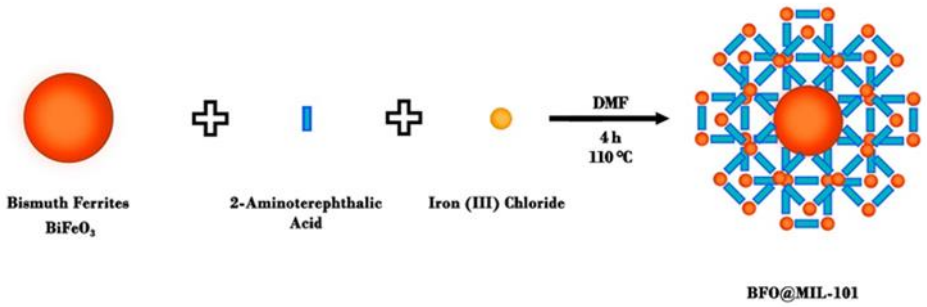

Fig.4.1. Schematic representation for the synthesis of hybrid nanomaterial BFO@MIL-101

The first step of this route is the synthesis of BFO particles by a sol-gel method, followed by the surface modification through the growth of a metal organic framework using 2-aminoterephthalic acid as organic precursor. A small amount of $FeCl_3$ has been also added to the reaction mixture. Details of the synthetic procedure are described in the paragraph 2.2.2.

The XRD patterns of BFO before and after the MOF growth process are shown in Fig.4.2. The main diffraction peaks at low angles (8.9°, 9.8° and 16.4°) are typical of MIL family [19,20] and the novel material exhibits a very similar profile with the MIL simulated pattern. The peaks above 20° are instead assignable to the BFO phase. [21] The presence of the diffraction peaks of both precursors is a clear indication that the growth process has occurred successfully and without degradation of the crystalline structure of the inorganic core.

The morphology and size of the nanoparticles of BFO@MIL-101 and bare BFO, used as a reference sample, were observed by electron scanning microscopy (SEM).

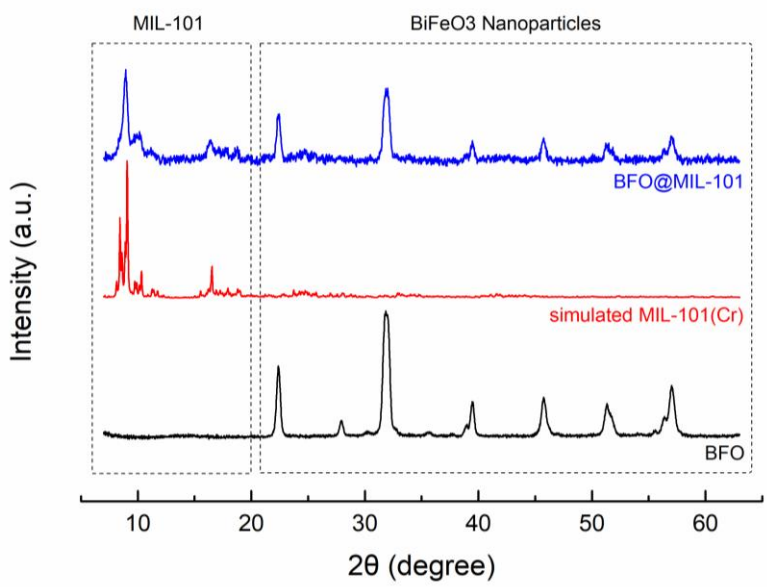

Fig.4.2. X-ray diffractograms of bare bismuth ferrite powder (black line), simulated MIL-101(Cr) (red line) and BFO@MIL-101 (blue line).

In both cases grains of average size around 100-200 nm are visible in the images. There are no evident morphological differences between the two samples, although, the grains of the BFO@MIL-101 appear to be more squared.

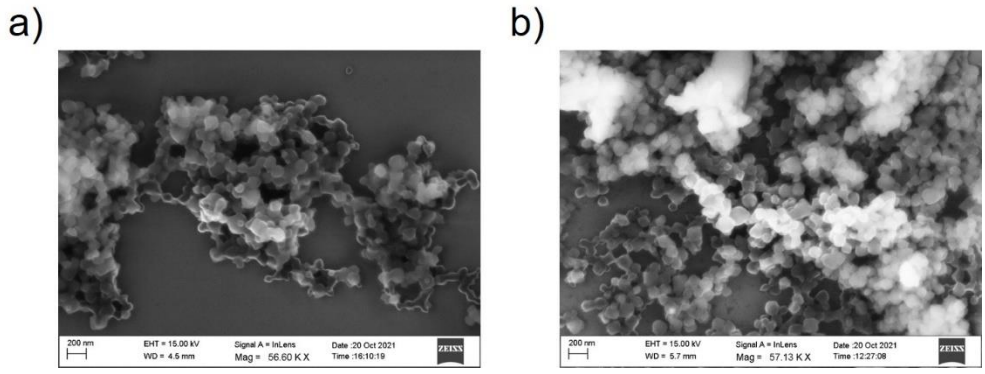

Fig.4.3. SEM morphology of (a) bare bismuth ferrite and (b) BFO@MIL-101

The atomic composition of BFO surfaces before and after MIL growth was investigated by XPS. The values obtained from the quantitative analysis are given in Table 1. After the formation of the MIL coating the C concentration is increased, as expected for the formation of an organic layer.

	XPS Atomic Concentrations						
	C 1s	O 1s	Fe 2p	Bi 4f	N 1s	Cl 2p	Bi / Fe
BFO	30.30	51.10	6.60	12.1	-	-	1.80
BFO@MIL-101	52.76	37.92	4.40	0.10	3.71	1.11	0.002

Table1. XPS atomic concentration of BFO and BFO@MIL-101 particles

Both iron ad bismuth concentration decreased. The iron concentration slightly decreases because of the lower iron density in the MIL structure, while the bismuth concentration decreases significantly due to the MIL coverage of the BFO particle. A significant amount of nitrogen appears in BFO@MIL spectrum, due to amino groups of aminoterephthalate ligands. [22] Another difference between modified sample and BFO bare is the presence of chlorine, which is in the coordination sphere of the iron cluster, according to the MIL structure. [23]

High-resolution spectra of Bi 4f, Fe $2p_{3/2}$, N 1s, Cl 2p, C 1s, and O 1s regions before and after MOF modification are shown in Figures 4.4 and 4.5.

The position of Bi 4f 7/2 and 5/2 peaks of bare BFO are 164.5 eV and 154.2 eV consistent with the presence of Bi^{3+}. [24] After MOF modification the peaks position does not change, but the intensity is strongly decreased due to the MOF formation as above mentioned.

In the Fe2p spectrum for BFO bare (Fig. 5.4c) appeared two peaks at 711.9 and 725.7 eV which corresponding to Fe $2p_{3/2}$ and Fe $2p_{1/2}$ signals. [25]

After MIL growth the centroid of the peak at 711.9 eV are shifted (Fig.5.4d), likely due to the convolution of Fe^{3+} in the MIL structure (typically around 712.6 eV) and the Fe^{3+} ions of BFO.

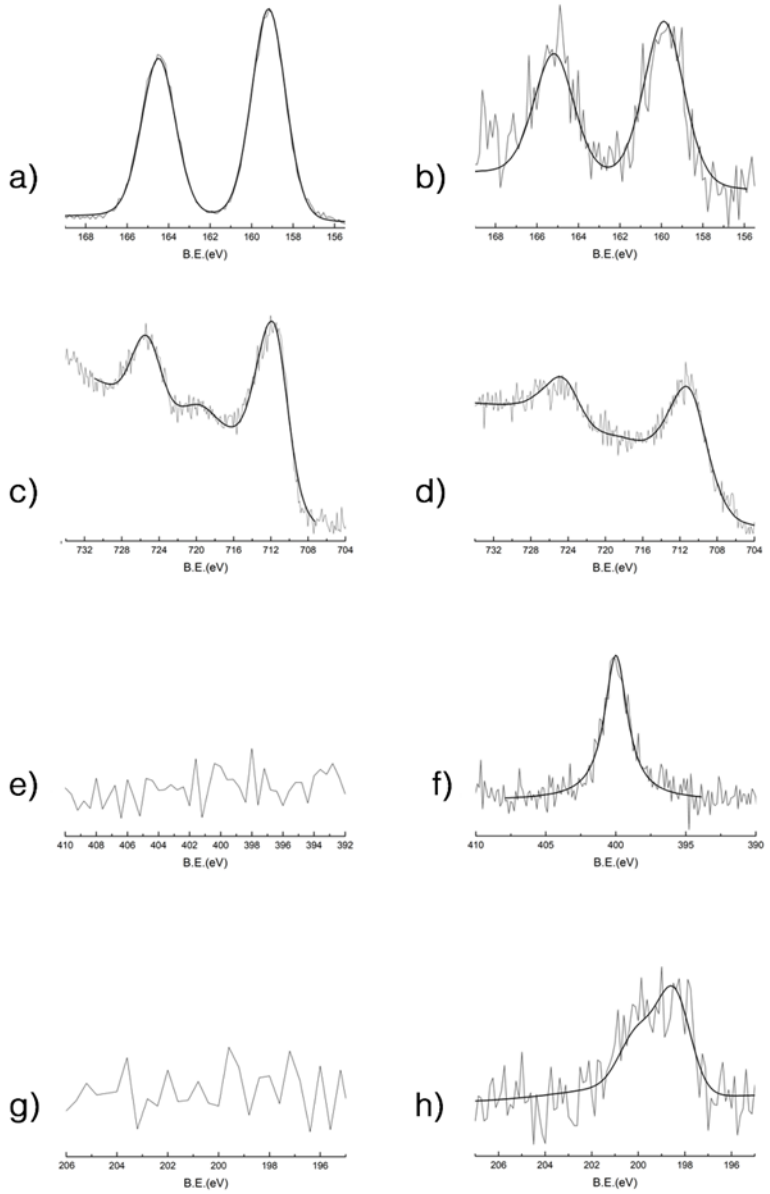

Fig.4.4. XPS spectra of Bi 4f (a, b), Fe 2p (c, d), N 1s (e, f) and Cl 2p (g, h), of bare MNPs (left) and MNPs@MIL (right).

The evolution of the C 1s signal before and after the formation of the MIL coating is shown in Fig.4.5. Before growing MIL, the C 1s signal on bare BFO is due to adventitious carbon always present in XPS spectra. It consists of a main peak at 285 eV and a small component at 286.2 eV due to oxidized carbons. [26,27] There is also a low-intensity tail around 288-289 eV, probably due to the surface carbonate formation. After growing MIL, the shape of the C 1s peak is changed. In particular, this band consists of three components at 285, 286.5 and 288.6 eV. The highest peak at 285 eV is attributable to aliphatic and aromatic hydrocarbon atoms (adventitious carbon). The component cantered at 286.5 eV is due to is due to both the C-O groups and the C-N atoms of the amino-terephthalic moieties. The characteristic peak at 288.6 eV is due to carboxylate groups (-COO). [28] In addition, a large and weak signal is detected at 289.4 eV and attributable to unreacted carboxylic acid (-COOH). [29]

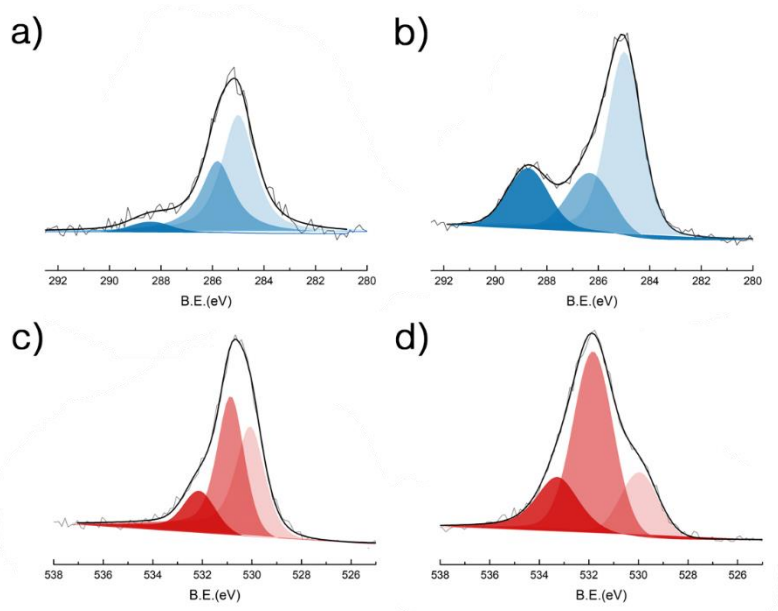

Fig.4.5. XPS spectra of C 1s (a, b) and O 1s (c, d) of bare MNPs (left) and MNPs@MIL (right).

In order to understand the effect of time on the MOF growth process, syntheses with various duration were performed. In particular, Figures 4.6 and 4.7 report the comparison between two sample (BFO@MIL[a] and BFO@MIL[b]), the first left to react for 2h and the second for 4h.

Fig.4.6 compares FT-IR spectra of bare BFO nanoparticles and the two hybrid compounds [a] and [b].

The intense peak at 600 cm^{-1} is common to all three samples and is related to Fe–O stretching modes. This peak, typical for iron oxides, appears to be less intense in the BFO@MIL[b] sample due to increased organic coverage.

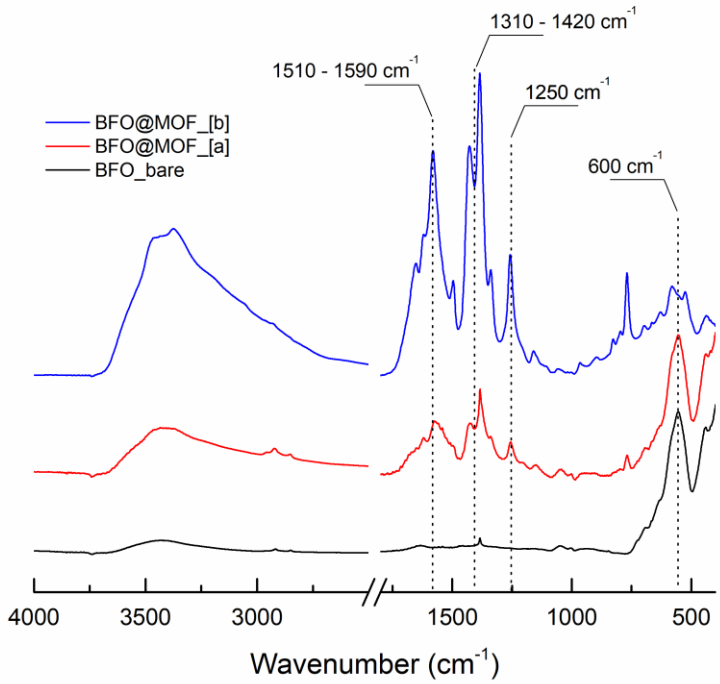

Fig.6. *FTIR spectra of bismuth ferrite nanoparticles (black line), hybrid BFO@MIL-101 after 2h (red line) and hybrid BFO@MIL-101 after 4h (blue line).*

The strong band at 1250 cm^{-1}, 1310–1420 cm^{-1} and 1510–1590 cm^{-1} are the typical vibrational modes of the aminoterephthalate ligands and correspond respectively to C-N symmetric and asymmetric stretching of the

amino group and to the COO− symmetric and asymmetric stretching of the terephthalate. [31,32] It can be noted that the peaks in this area are more intense and sharp in the BFO@MIL[b] sample due to the greater coverage of the metal organic framework. Finally, the peaks at 3456 cm^{-1} and 3373 cm^{-1}, in both modified samples, can be ascribed to the asymmetrical and symmetrical stretching of the amine groups. These peaks overlap the broad band in the 3000-3500 cm^{-1} region due to the O-H stretching of water.

The dependence of the MOF growth on the reaction time is also showed by a morphological study (figures 4.7a-c) performed by transmission electron microscopy (TEM). [33] The bare BFO particles (Fig.4.7a) are covered with small MOF crystal already after 2 hours of reaction (Fig.4.7b).

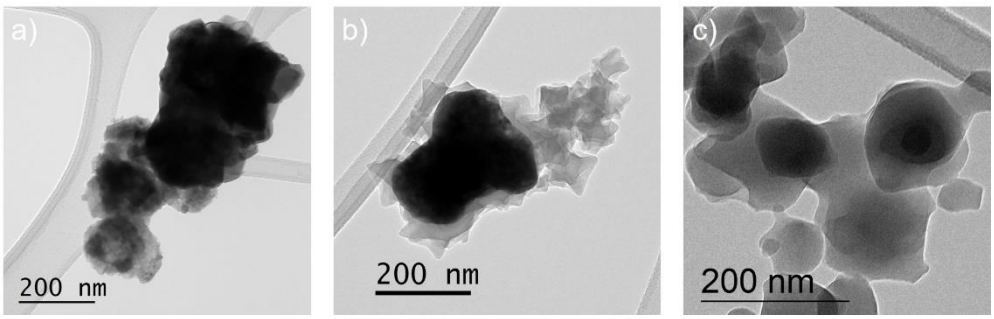

Fig.4.7. *TEM images of (a) bare bismuth ferrite, (b) hybrid BFO@MIL-101 after 2h and (c) hybrid BFO@MIL-101 after 4h.*

This coverage became more evident after 4 hours of reaction as shown in Fig.4.7c. The BFO@MIL[b] sample has a thicker and more homogeneous coating than the BFO@MIL[a]. There are less dense structures due to the presence of MOF and smaller darker particles due to the residual BFO that appears to be incorporated inside MOF.

Antimicrobial Tests were performed to evaluate the photoactive properties. The antibacterial activity of BFO and BFO@MIL-101 was tested in duplicate on four strains of Staphylococci (species Gram+) and four strains of E. Coli (species Gram-). Table 2 shows the values of Minimum Inhibitory

Concentration (MIC) and Minimum Bactericidal Concentration (MBC) obtained after 24 h of bacterial incubation with the two nanoparticles in the dark and following exposure to natural sunlight. As shown in the table, both nanoparticles did not exhibit any bacteriostatic or bactericidal activity in the dark condition, even at the highest concentration tested (100µg/ml). The antibacterial activity of both compounds shows a significant increase (in terms of decrease of MIC and MBC values) following irradiation with natural sunlight, which confirm the photoactivity of these materials.

	DARK					SUNLIGHT			
Bacterial strains	BFO		BFO@MIL-101			BFO		BFO@MIL-101	
	MIC (µg/ml)	MBC (µg/ml)	MIC (µg/ml)	MBC (µg/ml)		MIC (µg/ml)	MBC (µg/ml)	MIC (µg/ml)	MBC (µg/ml)
S.aureus ATCC 29213	›100	›100	›100	›100		0,20	›100	0,20	0,20
S.aureus ATCC 25923	›100	›100	›100	›100		0,39	›100	0,20	0,20
S. haemolyticus ATCC 29970	›100	›100	›100	›100		0,39	›100	0,20	0,39
S. haemolyticus ATCC 31874	›100	›100	›100	›100		0,39	›100	0,20	0,39
E.Coli ATCC 25922	›100	›100	›100	›100		›100	›100	100	›100
E.Coli ATCC 35218	›100	›100	›100	›100		›100	›100	100	›100
E.Coli ATCC 8739	›100	›100	›100	›100		›100	›100	100	›100
E.Coli ATCC 11229	›100	›100	›100	›100		›100	›100	100	›100

Table.2. Minimum Inhibitory Concentration (MIC) and Minimum Bactericidal Concentration (MBC) of BFO and BFO@MIL in dark condition and under sunlight irradiation.

The data obtained in this study shows that BFO@MIL-101 has a better antibacterial profile when compared to its unmodified BFO, as they exhibit increased antibacterial activity against both Gram+ and Gram- species tested.

In particular, BFO bare has a reduction in the MIC value (from >100 µg/ml in dark condition to 0.39 µg/ml under irradiation) for all strains of Staphylococcus tested. This value is significantly lower for BFO@MIL (from >100 µg/ml in dark condition to 0.20 µg/ml under irradiation). In addition, under irradiation BFO@MIL nanoparticles have lower MBC values (0.39µg/ml) compared to BFO bare (> 100 µg/ml) on all strains of staphylococcus tested. However, the most relevant aspect for BFO@MIL is the ability to begin inhibiting the growth of the four E.Coli strains, albeit at the highest concentration tested (100 µg/ml). Despite the presence of lipopolysaccharide in the outer membrane of Gram-negative bacteria, which gives protection against various antimicrobial agents, BFO@MIL nanoparticles photoactivated with natural sunlight, unlike nanoparticles, equally photoactivated, of pure BFO, are able to exert a bacteriostatic action (inhibiting bacterial growth) on all four strains of E. Coli used in the study. These results suggest that the antibacterial properties of BFO resulting from photoactivation with natural sunlight are substantially improved by MOF functionalization.

4.3. Conclusions

This chapter reports the synthesis of a new hybrid material obtained through the direct growth of a metallic organic structure of the MIL-101 family. Chemical characterizations confirmed that the growth of the organic coating was successful. Studies using FT-IR spectroscopy and transmission electron microscopy (TEM) have shown that the growth of MOF on the composite material is dependent on the reaction time. In addition, the morphological analysis conducted with TEM suggested that the growth of MIL-101 occurred at the expense of the bismuth ferrite inorganic core.

BFO@MIL-101 was applied as an anti-bacterial material under natural sunlight radiation against the bacterial strains of Staphylococcus Aureus, Staphylococcus Haemolyticus and Escherichia Coli. Tests have shown that the hybrid nanomaterial possess a significant increased antibacterial photoactivity, in terms of reduction of MIC and MBC values, compared to the bare BFO.

In particular, BFO@MIL-101 showed a lower MIC (0.20 µg/ml) and MBC(0.39µg/ml) compared BFO bare ((0,39µg/ml and >100 µg/ml, respectively) for all strains of Staphylococcus tested. However, the most relevant aspect for BFO@MIL-101 is the ability to inhibit the growth of the four E.Coli strains, albeit at the highest concentration tested (100 µg/ml).

The data obtained on antibacterial activity are promising, making the material suitable for use in disinfection processes against a wide range of bacterial strains to prevent and control the persistence of bacterial infections.

References

1. Fair, R. J., & Tor, Y. (2014). Antibiotics and bacterial resistance in the 21st century. Perspectives in medicinal chemistry, 6, PMC-S14459.

2. Jones, R. N., & Pfaller, M. A. (1998). Bacterial resistance: a worldwide problem. Diagnostic microbiology and infectious disease, 31(2), 379-388.

3. Frieri, M., Kumar, K., & Boutin, A. (2017). Antibiotic resistance. Journal of infection and public health, 10(4), 369-378.

4. Villatte, G., Massard, C., Descamps, S., Sibaud, Y., Forestier, C., & Awitor, K. O. (2015). Photoactive TiO_2 antibacterial coating on surgical external fixation pins for clinical application. International journal of nanomedicine, 10, 3367.

5. Nair, M. G., Nirmala, M., Rekha, K., & Anukaliani, A. (2011). Structural, optical, photo catalytic and antibacterial activity of ZnO

and Co doped ZnO nanoparticles. Materials Letters, 65(12), 1797-1800.

6. Dharmaraja, A. T. (2017). Role of reactive oxygen species (ROS) in therapeutics and drug resistance in cancer and bacteria. Journal of Medicinal Chemistry, 60(8), 3221-3240.

7. Van Acker, H., & Coenye, T. (2017). The role of reactive oxygen species in antibiotic-mediated killing of bacteria. Trends in microbiology, 25(6), 456-466.

8. Zhao, X., & Drlica, K. (2014). Reactive oxygen species and the bacterial response to lethal stress. Current opinion in microbiology, 21, 1-6.

9. Vatansever, F., de Melo, W. C., Avci, P., Vecchio, D., Sadasivam, M., Gupta, A., ... & Hamblin, M. R. (2013). Antimicrobial strategies centered around reactive oxygen species–bactericidal antibiotics, photodynamic therapy, and beyond. FEMS microbiology reviews, 37(6), 955-989.

10. Hwang, G. B., Noimark, S., Page, K., Sehmi, S., Macrobert, A. J., Allan, E., & Parkin, I. P. (2016). White light-activated antimicrobial surfaces: effect of nanoparticle types on activity. Journal of Materials Chemistry B, 4(12), 2199-2207.

11. Perni, S., Prokopovich, P., Piccirillo, C., Pratten, J., Parkin, I. P., & Wilson, M. (2009). Toluidine blue-containing polymers exhibit potent bactericidal activity when irradiated with red laser light. Journal of Materials Chemistry, 19(18), 2715-2723.

12. Fu, Z., & Xu, G. (2017). Crystalline, highly oriented MOF thin film: The fabrication and application. The Chemical Record, 17(5), 518-534.

13. Horcajada, P., Gref, R., Baati, T., Allan, P. K., Maurin, G., Couvreur, P., ... & Serre, C. (2012). Metal–organic frameworks in biomedicine. Chemical reviews, 112(2), 1232-1268.

14. Papadas, I., Christodoulides, J. A., Kioseoglou, G., & Armatas, G. S. (2015). A high surface area ordered mesoporous $BiFeO_3$ semiconductor with efficient water oxidation activity. Journal of Materials Chemistry A, 3(4), 1587-1593.

15. Irfan, S., Rizwan, S., Shen, Y., Li, L., Butt, S., & Nan, C. W. (2017). The gadolinium (Gd^{3+}) and Tin (Sn^{4+}) Co-doped $BiFeO_3$ nanoparticles as new solar light active photocatalyst. Scientific reports, 7(1), 1-12.

16. Jaffari, Z. H., Lam, S. M., Sin, J. C., & Zeng, H. (2019). Boosting visible light photocatalytic and antibacterial performance by decoration of silver on magnetic spindle-like bismuth ferrite. Materials Science in Semiconductor Processing, 101, 103-115.

17. Biswas, K., De, D., Bandyopadhyay, J., Dutta, N., Rana, S., Sen, P., ... & Chakraborty, P. K. (2017). Enhanced polarization, magnetic response and pronounced antibacterial activity of bismuth ferrite nanorods. Materials Chemistry and Physics, 195, 207-212.

18. Xiao, S., Fakhri, A., & Janani, B. J. (2021). Synthesis of spinel Tin ferrite decorated on Bismuth ferrite nanostructures for synergetic photocatalytic, superior drug delivery, and antibacterial efficiencies. Surfaces and Interfaces, 27, 101490.

19. Li, S.; Bi, K.; Xiao, L.; Shi, X. Facile preparation of magnetic metal organic frameworks core–shell nanoparticles for stimuliresponsive drug carrier. Nanotechnology 2017, 28, 495601.

20. Monforte, F.; Urso, M.; Alberti, A.; Smecca, E.; Mirabella, S.; Bongiorno, C.; Mannino, G.; Condorelli, G.G. New Synthetic Route for the Growth of FeOOH/NH_2-Mil-101 Films on Copper Foil for High Surface Area Electrodes. ACS Omega 2019, 4, 18495–18501.

21. Hao, S., Yi, J., Chao, X., Wei, L., & Yang, Z. (2016). Multiferroic properties in Mn-modified 0.7 $BiFeO_3$-$_{0.3}(Ba_{0.85}Ca_{0.15})(Zr_{0.1}Ti_{0.9})O_3$ ceramics. Materials Research Bulletin, 84, 25-31.

22. Tudisco, C., Pellegrino, A. L., Malandrino, G., & Condorelli, G. G. (2018). Surface anchoring of bi-functional organic linkers on piezoelectric $BiFeO_3$ films and particles: Comparison between carboxylic and phosphonic tethering groups. Surface and Coatings Technology, 343, 75-82.

23. Ezugwu, C. I., Zhang, S., Li, S., Shi, S., Li, C., Verpoort, F., ... & Liu, S. (2019). Efficient transformative HCHO capture by defective NH_2-UiO-66 (Zr) at room temperature. Environmental Science: Nano, 6(10), 2931-2936.

[24] Monforte, F., Falsaperna, M., Pellegrino, A. L., Bongiorno, C., Motta, A., Mannino, G., & Condorelli, G. G. (2019). Direct growth on Si (100) of isolated octahedral Mil-101 (Fe) crystals for the separation of aromatic vapors. The Journal of Physical Chemistry C, 123(47), 28836-28845.

[25] Grosvenor, A. P., Kobe, B. A., Biesinger, M. C., & McIntyre, N. S. (2004). Investigation of multiplet splitting of Fe 2p XPS spectra and bonding in iron compounds. Surface and Interface Analysis: An International Journal devoted to the development and application of techniques for the analysis of surfaces, interfaces and thin films, 36(12), 1564-1574.

[26] Swift, P. (1982). Adventitious carbon—the panacea for energy referencing?. Surface and Interface Analysis, 4(2), 47-51.

[27] Briggs, D., & Beamson, G. (1992). Primary and secondary oxygen-induced C1s binding energy shifts in x-ray photoelectron spectroscopy of polymers. Analytical chemistry, 64(15), 1729-1736.

[28] Monforte, F., Falsaperna, M., Pellegrino, A. L., Bongiorno, C., Motta, A., Mannino, G., & Condorelli, G. G. (2019). Direct growth on Si (100) of isolated octahedral Mil-101 (Fe) crystals for the separation of aromatic vapors. The Journal of Physical Chemistry C, 123(47), 28836-28845.

[29] Rojas, J. V., Toro-Gonzalez, M., Molina-Higgins, M. C., & Castano, C. E. (2016). Facile radiolytic synthesis of ruthenium nanoparticles on graphene oxide and carbon nanotubes. Materials Science and Engineering: B, 205, 28-35.

[30] Si, Y. H., Xia, Y., Shang, S. K., Xiong, X. B., Zeng, X. R., Zhou, J., & Li, Y. Y. (2018). Enhanced visible light driven photocatalytic behavior of $BiFeO_3$/reduced graphene oxide composites. Nanomaterials, 8(7), 526.

[31] Monforte, F., Urso, M., Alberti, A., Smecca, E., Mirabella, S., Bongiorno, C., ... & Condorelli, G. G. (2019). New synthetic route for the growth of α-FeOOH/NH_2-MIL-101 films on copper foil for high surface area electrodes. ACS omega, 4(20), 18495-18501.

[32] Nakamoto, K. (2009). Infrared and Raman spectra of inorganic and coordination compounds, part B: applications in coordination, organometallic, and bioinorganic chemistry. John Wiley & Sons.

33. Liu, L., Zhang, D., Zhu, Y., & Han, Y. (2020). Bulk and local structures of metal–organic frameworks unravelled by high-resolution electron microscopy. Communications Chemistry, 3(1), 1-14.

CHAPTER 5:

Intracellular Transport: The Interplay between Sodium Butyrate, Folic Acid and a Multifunctional Paramagnetic Fe_3O_4 - Based System

5.1. Introduction

Colorectal cancer (CRC) and liver and lung metastases (CLM) are a major cause of death in cancer patients; however, there is no agreed approach to the treatment of CLM. [1] One of the main problems of cancer therapies is the emergence of resistance to chemotherapy drugs (multidrug resistance, MDR). For the treatment a wide variety of cancers, the combined use of nanoparticles (NPs) and drugs [2] provides a promising strategy for overcoming MDR, increasing drug efficacy and reducing high-dose systemic toxicity. [3,4]

As concerned combined therapies, liposomes are the most used NPs, but recently the uses of other classes of these nanomaterials (such as carbon based nanostructures, micelles and metal and metal oxides NPs [2]) have attracted the interest of many researchers. Among them, the use of organic functionalized superparamagnetic iron oxide nanoparticles (SPIONs) has received increasing attention [5,6] because of they combine the versatility of surface functionalization with the magnetic properties and the biocompatible and environmentally friendly nature of the Fe_3O_4 core. [7,8]

Functionalized MNPs were investigated and, in some cases, are already in use for several biomedical applications such as proteins and cell sorting and manipulation, [9,10] cell labelling, [11,12] magnetic dialysis, [13]

magnetically controlled drug delivery, [14,15] Magnetic Resonance Imaging (MRI) [16–18] and magnetic thermotherapy. [19–22]

In combination with iron oxide nanoparticles, butyrate can be used as a potential anticancer agent, due to its interesting properties of reduction of the risk and the prevention of CRC. [23] It is found in fruits and vegetables along with other natural substances such as folate, selenium, vitamin D and other short-chain fatty acids (SCFAs). Butyric acid, which is the main energy source for normal colonocytes, can promote growth and proliferation, while in cancerous colon cells it inhibits proliferation and induces differentiation and apoptosis. [24–26] For this reason, although butyrate does not have a toxic effect on cancer cells, it can be used in anticancer therapy since it is useful for healthy cells, as it was widely demonstrated in cancer cell cultures and animal models of cancer. [24,27,28]

Taking into account these evidences, the cooperation of multifunctional MNPs with Sodium Butirrate (NaBu), can be a valuable tool for future cancer treatment.

This chapter is mainly focused on two issues: (i) the development of a versatile synthetic route based on a layer of phosphonic linkers able to connect different functional molecules that lead to the design of multifunctional magnetic biocompatible systems and (ii) the study of the effects, on the intracellular uptake and cell vitality, of the combined use of these MNPs modified with two different coatings, and NaBu used as a free formulation.

The Fe_3O_4 magnetic core was first functionalized with a monolayer consisting of a phosphonic acids having terminal amino groups, which provide an active platform for further functionalization with organic molecules. Then, an N-hydroxysuccinimide (NHS) activated forms of

Polyethylene glycol (PEG), folic acid (FA) and carboxy-X-rhodamine (Rhod) were covalently anchored on amine moieties.

The effects of FA as an optimizing ligand were also been investigated because it is one of the best-characterized ligands used to target cancer cells. [29] Moreover, the expression of folate receptors (FRs) in LoVo cells was correlated with the presence of folate in MNP coatings and, in turn, with cellular absorption.

Finally, in order to show that the combined use of MNPs and NaBu is a possible strategy to contrast cancer cells, the effects of NaBu as a free formulation or in association with this novel biocompatible magnetic nanoparticles, on the growth of LoVo cells were investigated.

5.2. Results and Discussion

Each step of the above synthetic pathway (see chapter 2 - paragraph 2.2.3) was monitored by XPS spectroscopy. The atomic compositions of bare MNPs, MNP@PA, MNP@PEG, MNP@PEG-FA and MNPs@PEG-FA with Rhodamine are shown in Table 1.

The signal of P2p is negligible and the signal of N1s (due to adventitious species) is very low in bare Fe_3O_4 nanoparticles. After anchoring of the phosphonic acid the observed N and P signals are clear indications of the presence of the NH_2-PA layer. In addition, the N/P atomic ratio close to 1 is consistent with the theoretical N/P ratio of the NH_2-PA molecule. For MNP@PEG-FA and MNPs@PEG-FA with Rhodamine, the increase in the N/P atomic ratio compared to MNPs@PA and MNP@PEG is attributable to the anchoring of functional species (FA and Rhodamine) containing carbon atoms. High resolution P2p, C1s and N1s XPS region provide further indications of the success of the functionalization steps. After the anchoring process of NH_2-PA, the P2p band at 133.2 eV was observed (Fig.5.1. left),

thus indicating the presence of the phosphonic acid on the surface. In addition, the B.E. position is shifted towards lower values compared to those typical for phosphonic acid, suggesting that both terminal –POH groups are deprotonated due to the occurrence of two P–O–Fe bonds. [40,42]

	MNPs	**MNP@PA**	**MNP@PEG**	**MNP@PEG-FA**	**MNP@PEG-FA with Rhod**
Fe 2p $_{3/2}$	17.2	16.2	16.1	13.2	12.1
O 1s	69.3	46.2	40.8	41.4	39.8
C 1s	12.9	31.1	37.3	38.9	42.2
P 2p	-	3.1	2.4	2.0	1.5
N 1s	0.5	3.0	2.1	2.6	2.9

Table 1. XPS estimated surface atomic concentrations of a) MNP@PA, b) MNP@PEG, c) MNP@PEG-FA and d) MNP@PEG-FA with Rhodamine.

The P2p band does not change after the anchoring of the other functional molecules (Fig.5.1 spectra b-d, left), thus indicating that the phosphonic acid is not removed during the immobilization of the functional molecules.

The N1s band of MNPs@PA (Fig.5.1 a, right) consists of two components of comparable intensity. In particular, the component at 399.9 eV is associated with the primary amine ($–NH_2$) groups of the anchored aminopropylphosphate, while the component centered at 401.5 eV is due to the amino groups interacting with the Fe_3O_4 surface through protonation or formation of –H bonds. [42] Some changes of the N1s shape (Fig.5.1, spectra b-d right) have been observed after the grafting of functional molecules PEG, FA and Rhodamine. The component at about 399.9 eV increases due to the formation of amide bonds (400.2 eV) [40] between the functional molecules

and PA-NH_2. Note that the intensity enhancement of this component is more evident for MNPs@PEG-FA and MNPs@PEG-FA with Rhodamine compared to MNPs@PEG, due to the presence of several nitrogen atoms in FA (B.E. ranging from 400 to 399 eV). [40] The C1s XPS regions of the different coatings namely MNP@PA, MNP@PEG, MNP@PEG-FA and MNP@PEG-FA with Rhodamine are reported in Fig.2 a-d, middle. The C1s band of PA@MNPs (Fig.5.1 a) consists of a single peak at 285.0 eV, assigned to aliphatic carbons.

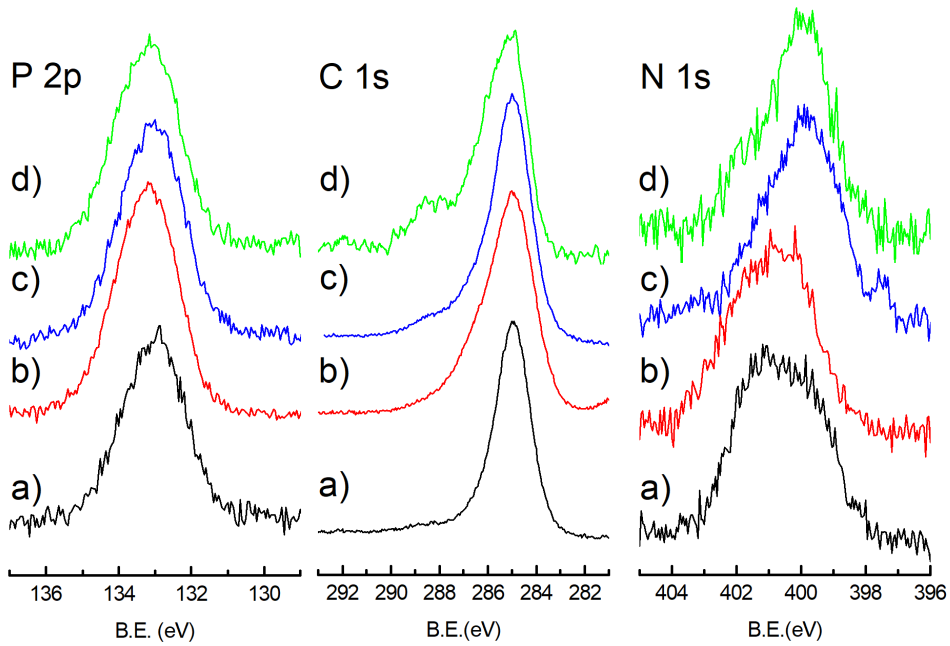

Fig.5.1. High resolution P 2p, C 1s and N 1s spectral regions of (a) MNP@PA (black line), (b) MNP@PEG (red line), (c) MNP@PEG-FA (blue line) and (d) MNP@PEG-FA with Rhodamine (green line).

The spectra of MNP@PEG, MNP@PEG-FA and MNP@PEG-FA with rhodamine (Fig. 5.1 b-d) show, beside the main peak at 285.0 eV due to aliphatic and aromatic carbons, an enlargement towards higher B.E. due to a component around 286 eV arising from the oxygen-bonded carbons of PEG.

In addition, in the case of MNP@PEG-FA and MNP@PEG-FA with Rhodamine, a component around 288.6 eV due to carboxylic and amidic groups of FA and Rhodamine can be observed.

The anchoring of FA on the functionalized MNPs has been also proved by UV-Vis spectra of a MNPs@PEG, MNP@PEG-FA and MNP@PEG-FA with Rhodamine. Fig. 5.2 compares the spectra of the three samples. The spectrum of a FA solution (2 μM) was added as reference. An evident band at 274 nm typical of the FA is clearly visible in the reference and in the MNP@PEG-FA and MNP@PEG-FA with Rhodamine, thus confirming the presence of FA in the MNPs.

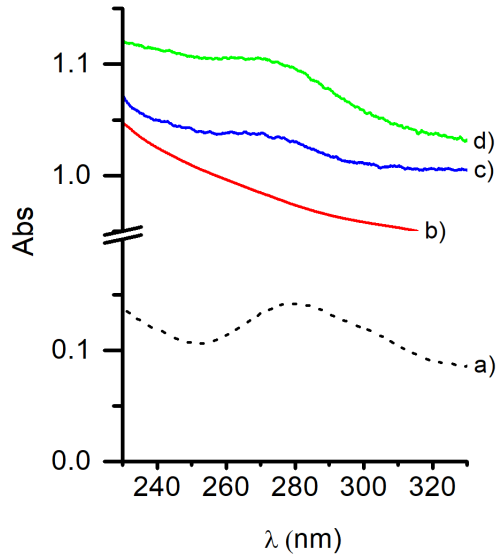

Fig.5.2. UV/Vis spectra of a) FA-NHS solution (2 μM) and b) MNP@PEG (red line), c) MNP@PEG-FA with Rhodamine (blue line) and d) MNP@PEG-FA (green line).

Figure 5.3 shows the viability of LoVo cells exposed for 48 h and 72 h to various concentrations of NaBu (blue line) as measured by the 3-(4,5-Dimethylthiazol-2-yl)-2,5-Diphenyltetrazolium Bromide (MTT) test. Viability of human colon adenocarcinoma cells in the presence of FA (violet

line), or MNP@PEG-FA (red line) or MNP@PEG (green line) together with the free formulations of NaBu are also shown.

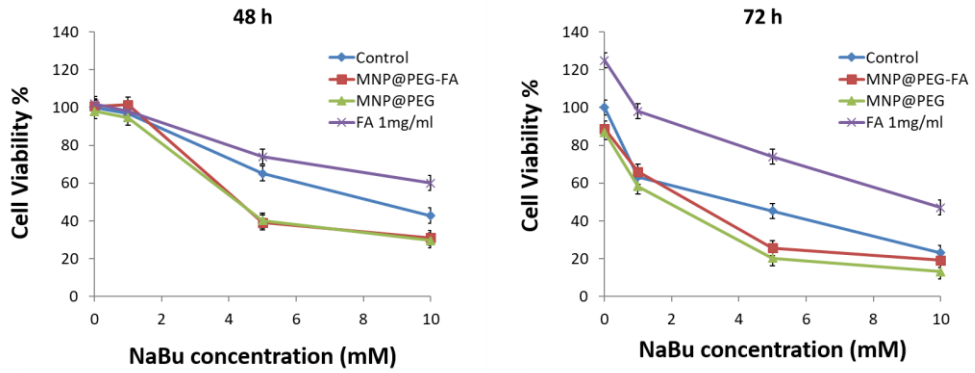

Fig.5.3. Viability of LoVo cells (MTT assay) incubated for 48 h and 72 h with various NaBu concentrations in the absence (blue line) and the presence of FA (violet line), MNP@PEG-FA (red line) and MNP@PEG (green line).

The effect of NaBu on LoVo cells was very significant, as evidenced by the relevant decrease in curves observed after 48 hours and even more evident after 72 hours. According to Fig.5.3, it is also clear that the reduction in viability is dose-depends. On the other hand, for all NaBu concentrations, LoVo cells exposed simultaneously to NaBu and folate (1 μg/mL) exhibited higher vitality compared to cells treated only with NaBu. Therefore, we can assume that folic acid shielded cancer cells from the cytotoxic effect of NaBu. In the presence of MNP@PEG-FA (red line) and MNP@PEG (green line), NaBu causes a significant cellular viability drop, particularly evident at 5 mM. Both MNPs (in the absence of NaBu) showed a low toxicity at 72 h, as previously demonstrated. [30,32] This behaviour indicates that the combination of NaBu with MNPs may lead to increased cytotoxic effects. In particular, the combined effect is more evident at a 5mM NaBu concentration, which is close to the physiological concentration. In fact, in normal colonocytes butyrate has a concentration gradient ranging from 5 mM

in the lumen to 0.5 mM in the basal part of the crypt. [33] From Fig.5.3, reporting the results obtained after 72 h of exposure, it is also clear that despite the similar profiles, cytotoxicity of the MNP@PEG-FA and the NaBu system was slightly lower than that of MNP@PEG and the NaBu system, likely because of the FA protective effect.

The cellular absorption of MNPs has been studied preliminarily by combining measurements of scanning electron microscopy (SEM), energy dispersive X-ray analysis (EDX) and confocal laser scanning microscopy (CLSM). All functionalized MNPs (15 μg/ml) were incubated for 72 hours with Lovo cells.

Figure 5.4 presents morphological SEM images and EDX maps of Fe distributions of untreated cells (controls), and of cells treated with MNP@PEG and MNP@PEG-FA. SEM images of MNP@PEG-FA treated samples show flattened cells and more rounded cells than other samples, including controls.

EDX maps show that the presence of Fe was evident in the cells treated with MNP@PEG-FA (Fig 5.4 B, C). This indicates a significant uptake of MNP@PEG-FA in LoVo cells, while it was much less evident for samples treated with MNP without FA. In this case, the amount of Fe inside the cells was greatly reduced (Figure 5.4 B, C), in agreement with our previous paper. [30]

A more quantitative comparison of the different MNPs behaviours was obtained by comparing the mean atomic ratio Fe/Au (Fig.5.5) measured in correspondence to the various cells. The presence of Au was due to the metallization process which produces a homogeneous coating which can be used as an internal standard. Typical examples of the area analysed to determine the Fe/Au ratio in a cell are presented in Fig.5.5. The results indicate that the presence of modified MNPs is nearly 10 times greater than that of MNPs without FA.

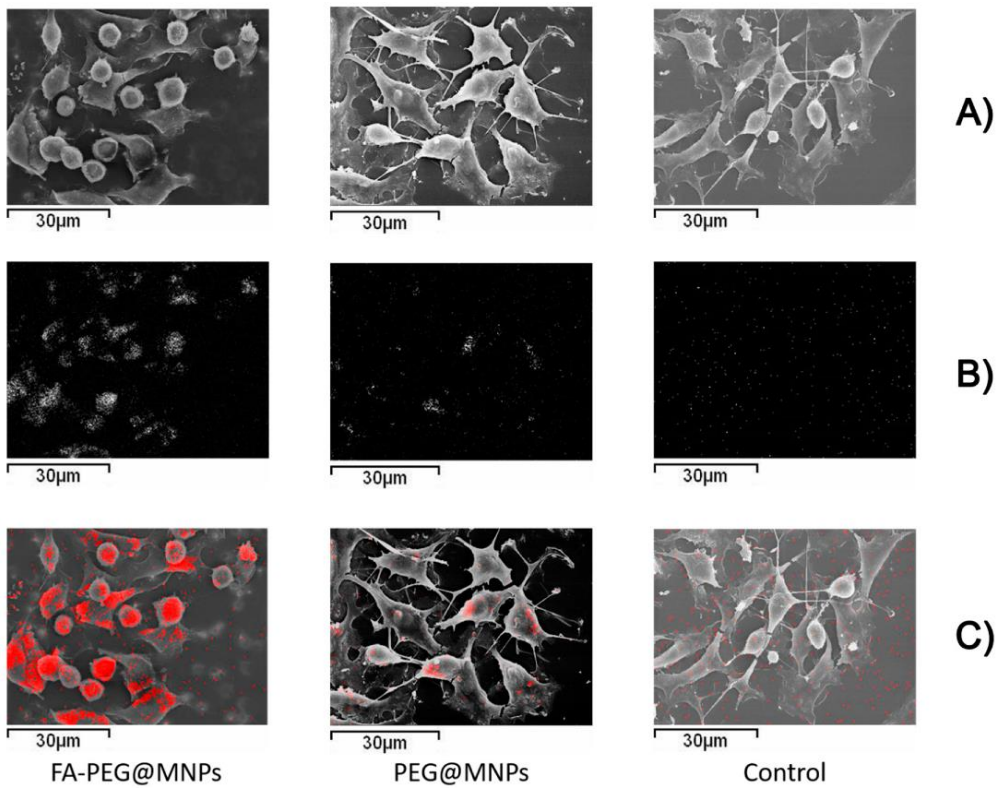

*Fig.5.4. (A) SEM images, (B) EDX maps of Fe distribution (bright spots), and (**C**) overlay images of SEM and EDX Fe distribution (Fe spots colored red) of samples of untreated cells (control) and cells incubated with either FA-PEG@MNPs or PEG@MNPs.*

In the presence of 10 mM NaBu with both types of MNPs (MNP@PEG and MNP@PEG-FA), the few cells detected by SEM-EDX were found to have elevated iron levels (Fig.5.5). The observed distribution was not homogenous, but accumulations was observed in some areas.

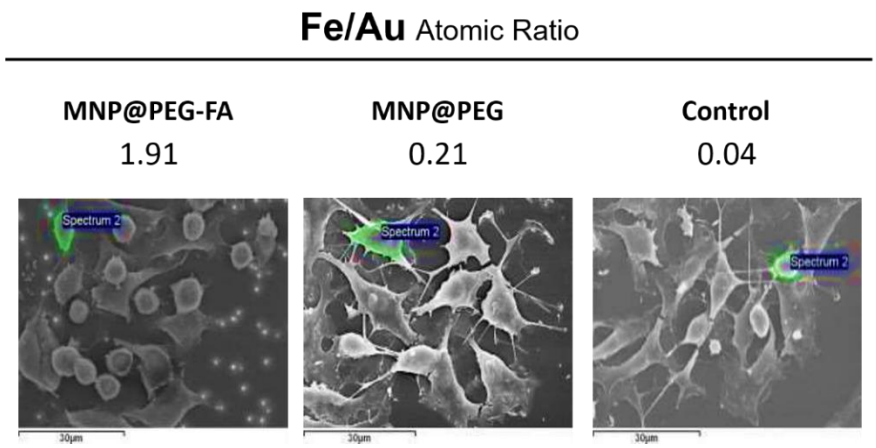

Fig.5.5. Average Fe/Au values of control and MNPs-treated samples obtained from EDX analyses performed in correspondence of the cells. Examples of the typical region analyzed for determining the Fe/Au ratio in a cell are reported in the SEM images.

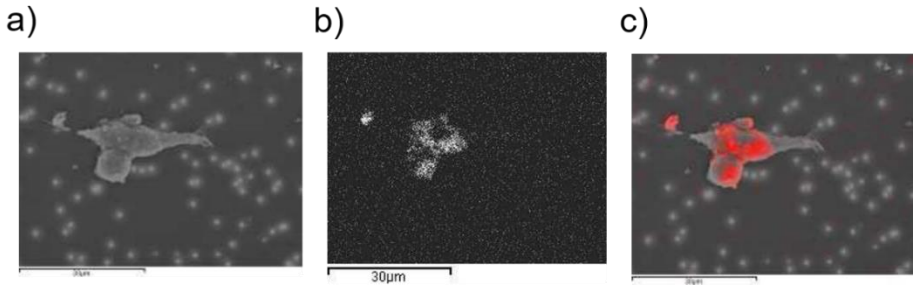

Fig.5.6. a) typical SEM images, b) EDX maps of Fe distribution (bright spots) and c) overlay images of SEM and EDX Fe distribution (Fe spots colored in red) of samples of cells incubate with MNP@PEG and NaBu (10mM). Similar images were observed for cells incubate with MNP@PEG-FA and NaBu (10mM).

The analytical approach, which combined SEM and EDX measures, provided a semi-quantitative estimate of cellular uptake without the use of luminescent probes. However, from the EDX measurements it is not possible to determine if MNPs are located inside the cell or anchored to the cell membrane due to the great depth of EDX sampling (about 2 μm [34]). Hence CLSM and TEM measurements were also performed to confirm

MNP@PEG-FA cell uptake and to obtain information on their localizations in the cells.

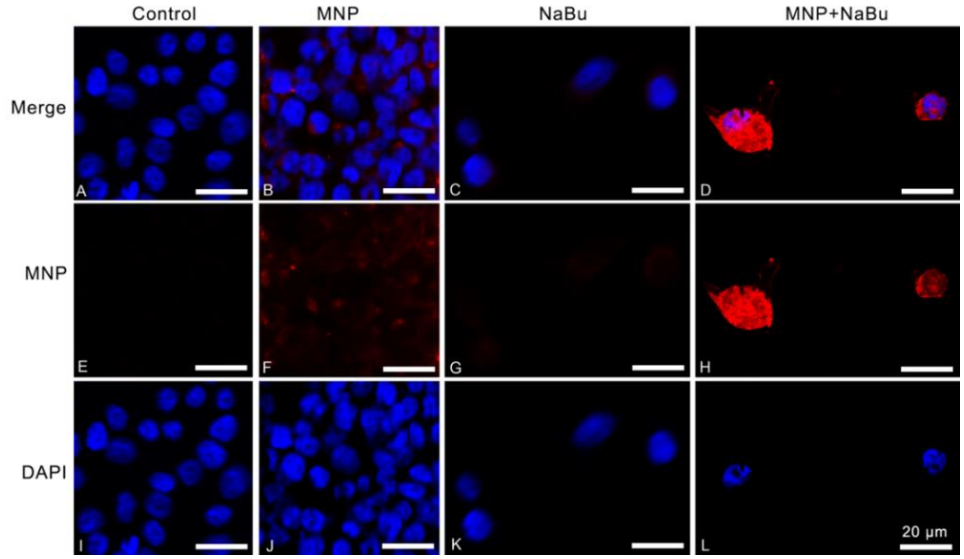

Fig.5.7. LoVo cells incubated with rhodamine-conjugated MNP@PEG-FA and/or NaBu. (A): LoVo cells not exposed to MNP@PEG-FA and/or NaBu (negative control). (B–D): LoVo cells incubated with MNPs, NaBu, and MNPs + NaBu, respectively. Red, and blue signals are due to rhodamine-conjugated MNP@PEG-FA, and to DAPI stained nuclei, respectively (E–H): the same images shown in A, B, C, and D, respectively, showing only the red fluorescence due to MNPs. (I–L): the same images shown in A, B, C, and D, respectively, showing only the blue fluorescence of DAPI staining the cell nuclei. Images were acquired with a Confocal Laser Scanning Microscopy using 405 and 555 nm wavelength lasers to detect the cell nucleus and the MNP@PEG-FA, respectively. Scale bar: 20 µm.

To enable fluorescence monitoring, carboxy-X-rhodamine was anchored to the MNP@PEG-FA shell. Confocal images show a fluorescent signal with widespread localization in the cytoplasm for MNP@PEG-FA-treated cells, while no signal was observed in the control (Fig.5.7). This is consistent with our previous research. In the presence of both NaBu and MNPs, the fluorescent signal indicated that also in this case MNPs were inside LoVo cells (Fig.5.7). Moreover, CLSM imagery at different focal

planes showed that MNPs were also localized in the nucleus (Fig.5.8), suggesting that the decrease in cell viability in the presence of NaBu and MNPs was caused by growth inhibition and apoptosis.

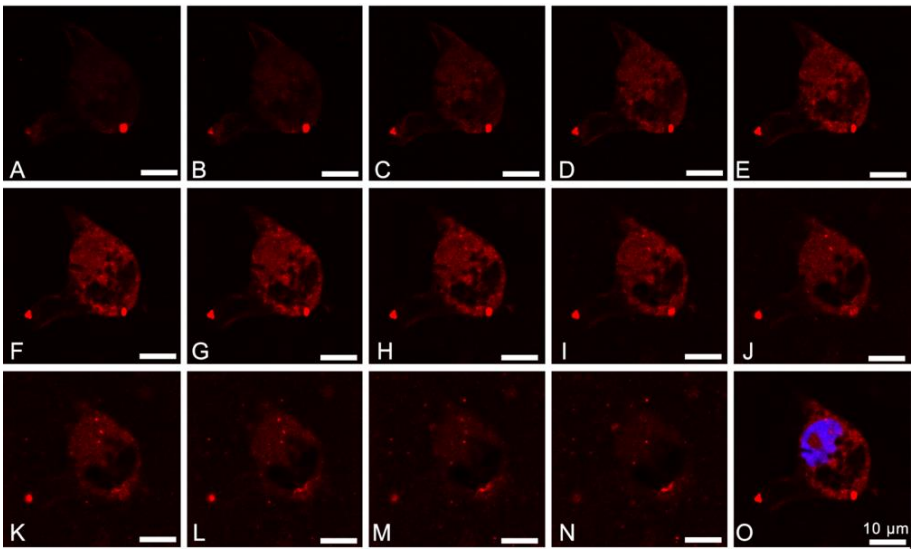

Fig.5.8. (A–N): Serial sections with 0.30 µm/section of a LoVo cell co-incubated with MNP@PEG-FA conjugated with Rhodamine, and with NaBu. (O): Panel corresponding to the central serial section H with the visualization of the nucleus (stained in blue with DAPI). Scale bar: 10 µm.

The cellular location of MNPs was also studied using TEM observations. After passing through the plasma membrane, nanoparticles spread into the cytoplasm either as monodispersed MNP or as aggregates. The structure and function of cytoplasmic organelles, in particular mitochondria, have therefore been altered to a different extent by the presence of MNP more or less as shown in TEM micrographs (Fig.5.9). MNP@PEG-FA presence in mitochondria and nucleus is shown by TEM images in fig 5.10a and 5.10b respectively.

Instead, Fig. 5.10c shows a non-treated cell used as a control. In the mitochondrial matrix (Fig. 11a and inset) MNPs are visible as small spots or externally bounded to ribosomes of rough reticulum.

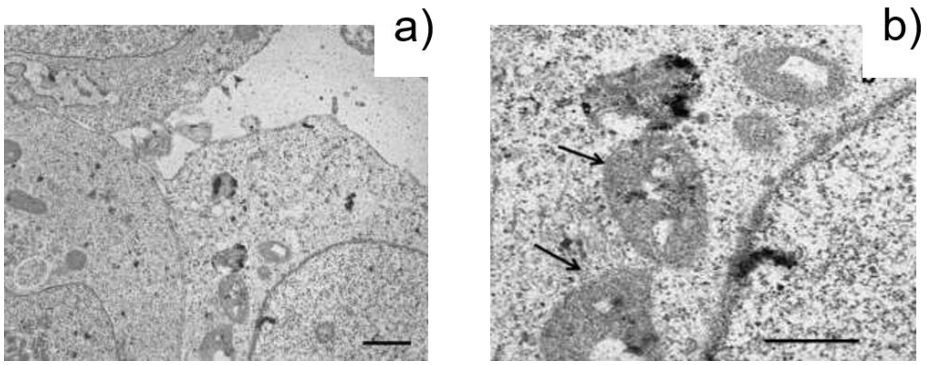

Fig.5.9. TEM Images of uptake of MNP@PEG-FA after 72 h in Lovo cells (a) and in (b) mitochondria (black arrows) with enlarged cristae and aggregates of MNPs in the matrix. Scale bar: a = 1 μm, b = 0.5 μm

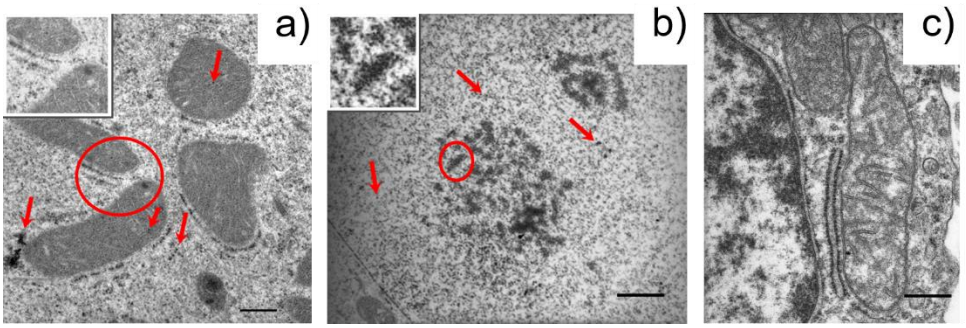

Fig.5.10. TEM micrographs of (a, b) LoVo cellular uptake of MNP@PEG-FA after 72 h of incubation, (c) control cells. A group of mitochondria (a) and the surrounding cytoplasm contain MNPs (red arrows). In the nucleus (b) MNP@PEG-FA spreads between chromatin (red arrows). The magnified images (white border frame) of the area indicated by red circles. Scale bar: a = 0.6 μm, inset: 1.4×; b = 0.7 μm, inset 2.5×; c = 0.6 μm

In the nucleus, the functionalized nanoparticles were dispersed between the filamentous chromatin (Fig. 5.10b). In particular, where the chromatin is more condensed, as in the nucleolar area, they appear concentrated and distinctly observable because of their higher electron density (inset Fig.

5.10b). TEM and CLSM imagery suggested that butyrate-transcriptional activation in combination with MNPs is actually capable of increasing programmed cell death, likely because of the presence of nuclear and mitochondrial ferromagnetic nanoparticles.

An CLSM analysis was also performed to assess the presence of the folate receptor in LoVo cells and the effects of NaBu and folate on FRs expression. FRs, known as the high-affinity membrane proteins for folate, are known to be overexpressed in tumor tissue. [29] Figure 5.11 compares the presence of FRs in LoVo cells. The green fluorescent signal, which appears after treatment with MNP@PEG-FA and MNP@PEG, clearly indicates the presence of this receptor.

For the cells treated with MNP@PEG-FA (Fig. 5.11 G–I), the fluorescence signal was stronger compared to the cells treated with MNP@PEG (Fig. 5.11 D–F) and to the control (Fig. 5.11 A–C) for the same incubation time. This effect is even more evident (Fig. 5.11 J–L) for LoVo cells treated with FA used as a free formulation (1 μg/mL). This behavior indicates that the presence of FA, whether anchored to MNPs or added as a free formulation, increases the expression of FRs. In turn, FRs-induced overexpression can increase the uptake of MNP@PEG-FA in LoVo cells, as shown in the EDX and confocal analyses (Fig. 5.4 and Fig. 5.7). In fact, FRs act as MNP@PEG-FA transporters that determine a greater uptake of these specifically modified nanoparticles via receptor-mediated endocytosis. [35] In previous studies, multiple roles were assigned to FRs. Once linked to their ligand, they internalize and locate themselves in the nuclear region, acting as transcription factors, [36] regulating the expression of some promoter regions. This behavior may explain the observed presence of functionalized MNPs in the nucleus (Fig. 5.8 and Fig. 5.10b). MNP@PEG-FA diffuse into the nucleus, together with FRs, remaining mainly in the nucleolar zone. FRs can

form macromolecular complexes where they can trigger intracellular signaling.

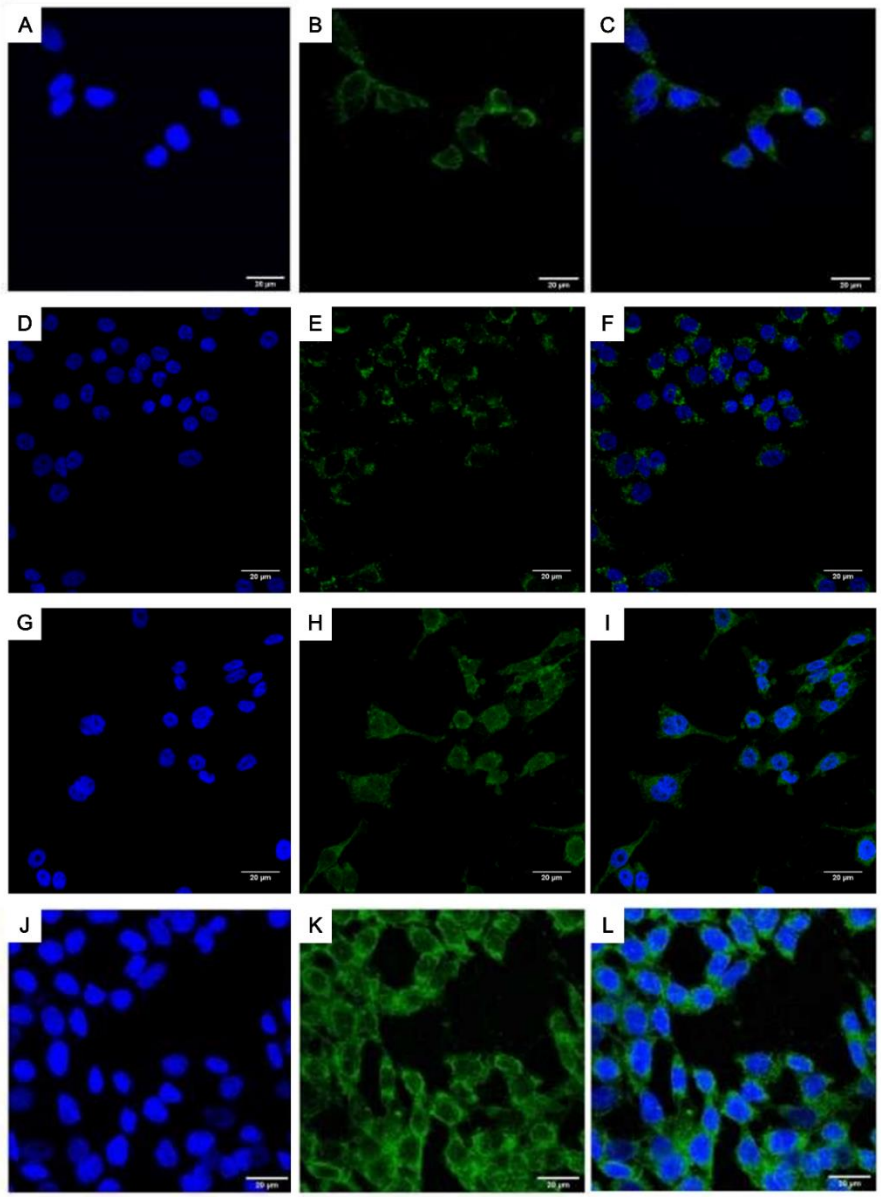

Fig.5.11. Folate receptors (FRs) analysis (CLSM) in LoVo cells incubated for 48 h (A–C) alone (control) and with (D–F) MNP@PEG, (G–I) MNP@PEG-FA and (J–L) FA used as a free formulation (1 μg/mL). In A, D, G and J nuclei are stained with DAPI (blue); B, E, H and K green florescence of FRs; in C, F, I, and L a merge was made. Scale bar 20 μm.

Earlier studies strongly suggest that FRs can function not only as a carrier of folates, but may also confer signaling and growth advantages to malignant cells [37] and serves as a useful marker for cancer. [38]

In the presence of 10 mM NaBu (Fig.5.12), similar intensities of the fluorescence signal were observed for cells treated with MNP@PEG and MNP@PEG-FA.

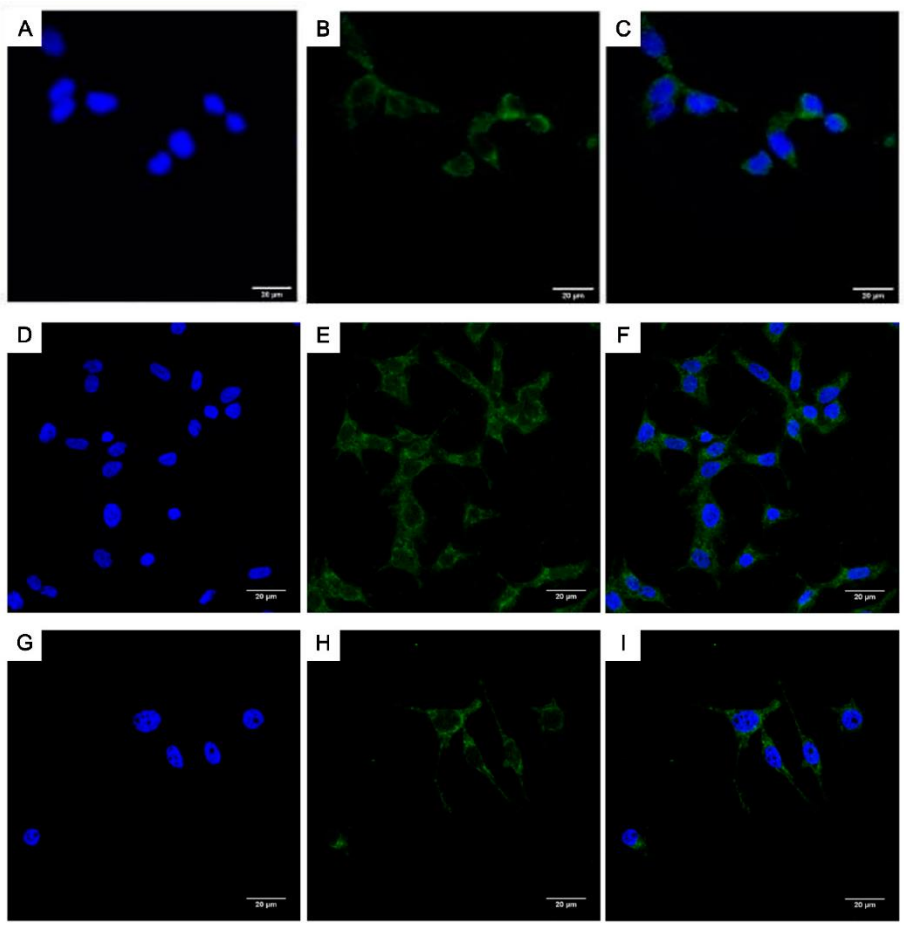

Fig.5.12. FRs analysis (CLSM) of LoVo cells incubated for 48 h (A–C) alone (control), and with (D–F) PEG@MNP or (G–I) MNP@PEG-FA in the presence of NaBu. In A, D and G nuclei are stained with DAPI (blue); B, E and H green florescence of FRs; in C, F and I a merge was made. Scale bar 20 µm.

CLSM analysis indicated that without NaBu, FRs were more expressed on the cells treated with MNP@PEG-FA, while in presence of NaBu no differences were observed between the cells treated with MNP@PG-FA and MNP@PEG. It is likely that these effects were due to NaBu-induced differentiation that led to similar uptake of the two types of MNPs. [39]

The combined effects of 1 µg/mL of FA and 10 mM NaBu (both used as a free formulations) on cell morphology after 48 h of treatment were studied by SEM (Fig.5.13). The morphologies of untreated LoVo cells (Fig. 5.13A) and cells exposed to FA (Fig.5.13B) present similar morphologies. Significant differences have appeared in the presence of NaBu (Fig.5.13C). In this case, SEM observations revealed a small number of flattened and elongated cells on the surface with a smooth plasma membrane. Round cells of altered size and shape were also found, probably apoptotic bodies or deformed cells.

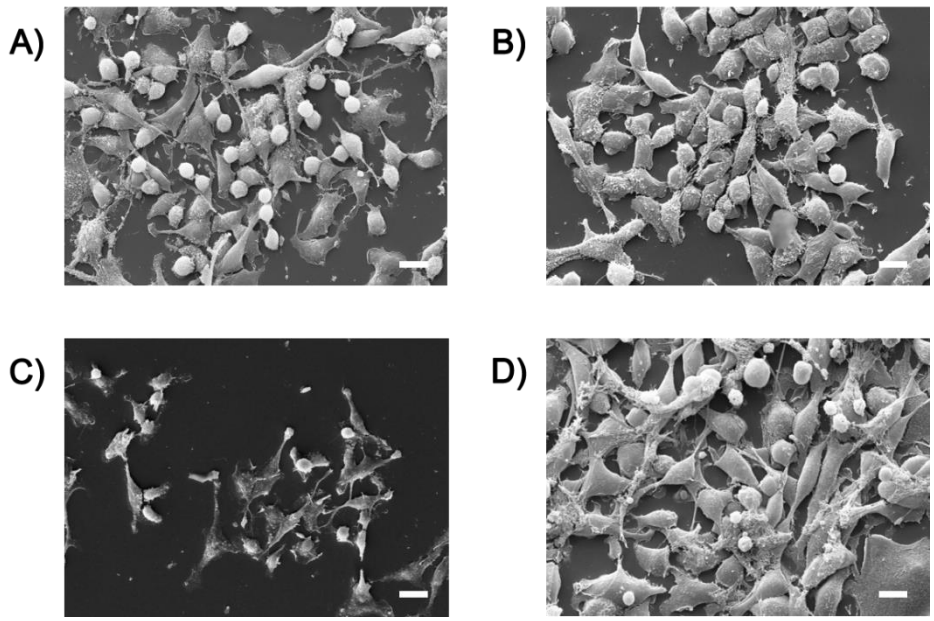

Fig.5.13. SEM images of (A) LoVo cells alone (control) and LoVo cells exposed for 48 h to (B) FA, (C) NaBu alone and (D) NaBu and FA. Scale bar 10 µm.

The combined treatment (Fig.5.13D) of FA and NaBu led to the growth of cells with an almost normal morphology (similar to Fig.5.13A and 5.13B), but accompanied by the presence of several round cells similar to those seen on Fig.5.13C.

These results are consistent with data from MTT. Since exposure to NaBu leads to significant changes in cell growth, the presence of FA, which acts as a protective agent, has reduced these changes. The combined effect of NaBu and folate was shown to modulate the cytotoxic action of fatty acids, as demonstrated by MTT and morphological analysis of SEM. The combined effect of NaBu and folate indicated that the latter seemed to modulate the cytotoxic action of fatty acids as demonstrated by MTT and SEM morphological analysis.

Using 10 mM NaBu, butyrate-induced differentiation stopped cell proliferation, resulting in apoptosis and detachment, especially when used in conjunction with MNPs. At this concentration, SEM samples showed only a few scattered cells and cellular debris. Because of these problems the analysis was performed at 1 mM NaBu. Figure 5.14A presents untreated in vitro cultured LoVo cells forming (after 72 h) more or less confluent monolayers. The shape of the cells varied from flattened to rounded in accordance with their replication stage. Similar images were seen when adenocarcinoma cells were exposed to MNP@PEG-FA or MNP@PEG (Fig. 5.14B and 5.14C) without adding NaBu. Obvious effects occurred when the cells were exposed to the action of NaBu 1 mM (Fig.5.14D). Cell morphology and number were significantly altered, and normal round cells, a sign of mitotic activity, were hardly present. These features were likely caused by the differentiating effect of NaBu. The cells were of a variety of shapes and sizes, flattened on the substrate with cytoplasmic areas extending in all directions. The plasma membrane had almost no specialization and often seemed to swell to form small blebs. Combined therapy with MNP@PEG-FA and NaBu induced the

same alteration as the cellular form, but the cells appeared less flattened, with a more three-dimensional aspect (Fig.5.14E). Following simultaneous exposure to PEG@MNPs and NaBu, the LoVo cells exhibited significant shape and size changes and appeared to be more stressed than with butyrate alone (Fig.5.14F).

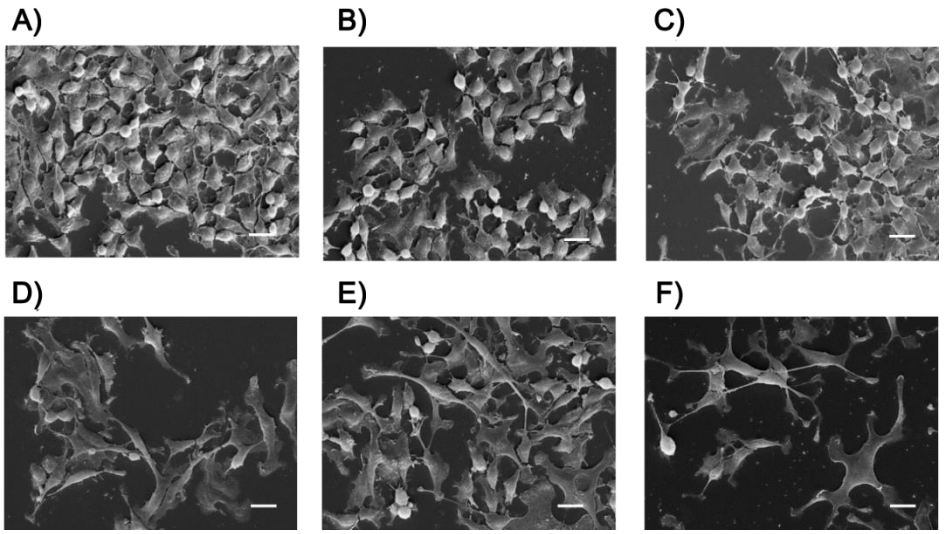

*Fig.5.14. LoVo cells visualized by scanning electron microscopy. Control cells (**A**) in the presence of MNP@PEG-FA (**B**) and MNP@PEG (**C**). The cells after NaBu treatment (**D**) and the combined action of MNP@PEG-FA (**E**) and MNP@PEG (**F**) with NaBu. Scale bar 10 µm.*

The typical differentiation induced by NaBu and, consequently, its cytotoxic action initially caused cell distension and adhesion on the substrate as well as reduced proliferation. These characteristics triggered the apoptotic process and, as a result, the loss of cell-cell and cell–substrate contact.

The addition of folic acid appeared to inhibit or decrease the action of butyrate by maintaining some degree of proliferation and delaying apoptosis.

The combined treatment with NaBu and PEG@MNP demonstrated the greatest cytotoxic effect on LoVo cell morphology (Fig.5.8F), supporting the

MTT results shown in Fig.5.3. On the other hand, the presence of MNPs@PEG-FA, thanks to their ability to enter the nucleus, increased proliferation, counterbalancing the effects on transcription due to the presence of NaBu. This behavior resulted in a slightly less cytotoxic effect of the NaBu/MNP@PEG-FA combination compared to the NaBu/MNP@PEG one.

5.3. Conclusions

In this chapter it is reported the synthesis of a magnetic biocompatible systems, based on a phosphonic monolayer having a -NH_2 terminal moieties, which allow the anchoring of various functional molecules (PEG, FA and Rhod), thus improving the versatility and the multi-functionality of the system. This novel material was used to investigate the effects of the interplay between MNPs modified with multifunctional layers containing or not FA and NaBu used as a free formulation.

Without NaBu, MNPs with pure PEG coating did not show significant cellular uptake, while the introduction of FA molecules into the organic coating was able to increase cellular uptake by almost ten times, as found through label free SEM/EDX investigation. Moreover, an important characteristic of our system is that, due to the addition of folic acid in the MNP coating, the amount of FRs in LoVo cells has increases on cell membranes, as demonstrated by confocal microscopy.

When NaBu was present, the differences between the two types of MNPs containing or not FA were greatly reduced. We demonstrated that contemporary exposure of adenocarcinoma cells to NaBu and MNPs with or without FA caused a significant decrease in the viability of LoVo cells, whereas an equal expression of FRs was highlighted. It is likely that these

effects are due to butyrate-induced differentiation leading to similar uptake of both types of MNPs. [39]

Furthermore, our results suggest that folate in the coating or used as a free formulation may modulate the cytotoxic action of NaBu.

Following these findings, NaBu treatment when used in combination with magnetic nanoparticles with or without FA, depending on the particular properties of the cancer cells, could represent a useful therapeutic tool in future cancer treatment.

References

1. Van Cutsem, E.; Oliveira, J. ESMO Guidelines Working Group. Advanced colorectal cancer: ESMO clinical recommendations for diagnosis, treatment and follow-up. Ann. Oncol. 2009, 20 (Suppl. 4), 61–63.

2. Gurunathan, S.; Kang, M.H.; Qasim, M.; Kim, J.H. Nanoparticle-Mediated combination therapy: Two-in-one approach for cancer. Int. J. Mol. Sci. 2018, 19, 3264.

3. Xu, X.; Ho, W.; Zhang, X.; Bertrand, N.; Farokhzad, O. Cancer nanomedicine: From targeted delivery to combination therapy. Trends Mol. Med. 2015, 21, 223–232.

4. Colone, M.; Calcabrini, A.; Stringaro, A. Drug Delivery Systems of Natural Products in Oncology. Molecules 2020, 25, 4560.

5. Yiu, H.H.P. Engineering the multifunctional surface on magnetic nanoparticles for targeted biomedical applications: A chemical approach. Nanomedicine 2011, 6, 1429–1446.

6. Santhosh, P.B.; Ulrih, N.P. Multifunctional superparamagnetic iron oxide nanoparticles: Promising tools in cancer theranostics. Cancer Lett. 2013, 336, 8–17.

7. Reddy, L.H.; Arias, J.L.; Nicolas, J.; Couvreur, P. Magnetic nanoparticles: Design and characterization, toxicity and biocompatibility, pharmaceutical and biomedical applications. Chem. Rev. 2012, 112, 5818–5878.

8. Daishun, L.; Nohyun, L.; Taeghwan, H. Chemical synthesis and assembly of uniformly sized iron oxide nanoparticles for medical applications. Acc. Chem. Res. 2015, 48, 1276–1285.

9. Pan, Y.; Du, X.; Zhao, F.; Xu, B.Magnetic nanoparticles for the manipulation of proteins and cells. Chem. Soc. Rev. 2012, 41, 2912–2942.

10. Huang, Z.; Pei, N.; Wang, Y.; Xie, X.; Sun, A.; Shen, L.; Zhang, S.; Liu, X.; Zou, Y.; Qian, J.; et al. Deep magnetic capture of magnetically loaded cells for spatially targeted therapeutics. Biomaterials 2010, 31, 2130–2140.

11. Wilhelm, C.; Gazeau, F. Universal cell labelling with anionic magnetic nanoparticles. Biomaterials 2008, 29, 3161–3174.

12. Neoh, K.G.; Kang, E.T. Surface modification of magnetic nanoparticles for stem cell labeling. Soft Matter. 2012, 8, 2057–2069.

13. Herrmann, I.K.; Bernabei, R.E.; Urner, M.; Grass, R.N.; Beck-Schimmer, B.; Stark, W.J. Device for continuous extracorporeal blood purification using target-specific metal nanomagnets. Nephrol. Dial. Transplant. 2011, 26, 2948–2954.

14. N'Guyen, T.T.T.; Duong, H.T.T.; Basuki, J.; Montembault, V.; Pascual, S.; Guibert, C.; Fresnais, J.; Boyer, C.; Whittaker, M.R.; Davis, T.P.; et al. Functional iron oxide magnetic nanoparticles with hyperthermia-induced drug release ability by using a combination of orthogonal click reactions. Angew. Chem. Int. Ed. Engl. 2013, 52, 14152–14156.

15. Mody, V.V.; Cox, A.; Shah, S.; Singh, A.; Bevins, W.; Parihar, H. Magnetic nanoparticle drug delivery systems for targeting tumor. Appl. Nanosci. 2014, 4, 385–392.

16. Arosio, P.; Thévenot, J.; Orlando, T.; Orsinia, F.; Cortid, M.; Marianie, M.; Bordonalid, L.; Innocenti, C.; Sangregorio, C.; Oliveira, H.; et al. Hybrid iron oxide-copolymer micelles and vesicles as contrast agents for MRI: Impact of the nanostructure on the relaxometric properties. J. Mater. Chem. B 2013, 1, 5317–5328.

17. Tassa, C.; Shaw, S.Y.; Weissleder, R. Dextran-coated iron oxide nanoparticles: A versatile platform for targeted molecular imaging,

molecular diagnostics, and therapy. Acc. Chem. Res. 2011, 44, 842–852.

18. Naseri, N.; Ajorlou, E.; Asghari, F.; Pilehvar-Soltanahmadi, Y. An update on nanoparticle-based contrast agents in medical imaging. Artif. Cells Nanomed. Biotechnol. 2018, 46, 1111–1121.

19. Troyer, D.L.; Bossman, S.H. Utilization of magnetic nanoparticles for cancer therapy. In Nanomedicine and Cancer; Srirajaskanthan, R.P., Victor, R., Eds.; Science Publisher and CRC Press Taylor & Francis Group: Boca Raton, FL, USA, 2012.

20. 20. Creixell, M.; Bohòrquez, A.C.; Torres-Lugo, M.; Rinaldi, C. EGFR-targeted magnetic nanoparticle heaters kill cancer cells without a perceptible temperature rise. ACS Nano 2011, 5, 7124–7129.

21. Yoo, D.; Jeong, H.; Noh, S.H.; Rinaldi, C. Magnetically triggered dual functional nanoparticles for resistance-free apoptotic hyperthermia. Angew Chem. Int. Ed. 2013, 52, 13047–13051.

22. Fantechi, E.; Innocenti, C.; Zanardelli, M.; Fittipaldi, M.; Falvo, E.; Carbo, M.; Shullani, V.; Di Cesare Mannelli, L.; Ghelardini, C.; Ferretti, A.M.; et al. A smart platform for hyperthermia application in cancer treatment: Cobalt-doped ferrite nanoparticles mineralized in human ferritin cages. ACS Nano 2014, 8, 4705–4719.

23. Lamprecht, S.A.; Lipki, M. Chemoprevention of colon cancer by calcium, vitamin D and folate: Molecular mechanisms. Nat. Rev. Cancer 2003, 8, 601–614.

24. Donohoe, D.R.; Holley, D.; Collins, L.B.; Montgomery, S.A.; Whitmore, A.C.; Hillhouse, A.; Curry, K.P.; Renner, S.W.; Greenwalt, A.; Ryan, E.P.; et al. A gnotobiotic mouse model demonstrates that dietary fiber protects against colorectal tumorigenesis in a microbiota- and butyrate-dependent manner. Cancer Discov. 2014, 4, 1387–1397.

25. Corrêa-Oliveira, R.; Fachi, J.L.; Vieira, A.; Takeo Sato, F.; Vinolo, M.A.R. Regulation of immune cell function by short-chain fatty acids. Clin. Transl. Immunol. 2016, 5, e73.

26. Donohoe, D.R.; Collins, L.B.; Wali, A.; Bigler, R.; Sun, W.; Bultman, S.J. The Warburg effect dictates the mechanism of butyrate mediated

histone acetylation and cell proliferation. Mol. Cell 2012, 48, 612–626.

27. Encarnacao, J.C.; Abrantes, A.M.; Pires, A.S.; Botelho, M.F. Revisit dietary fiber on colorectal cancer: Butyrate and its role on prevention and treatment. Cancer Metastasis Rev. 2015, 34, 465–478.

28. Ma, X.; Zhou, Z.; Zhang, X.; Fan, M.; Hong, Y.; Feng, Y.; Dong, Q.; Diao, H.; Wang, G. Sodium butyrate modulates gut microbiota and immune response in colorectal cancer liver metastatic mice. Cell Biol. Toxicol. 2020, 36, 509–515.

29. Stella, B.; Arpicco, S.; Peracchia, M.T.; Desmaële, D.; Hoebeke, J.; Renoir, M.; D'Angelo, J.; Cattel, L.; Couvreur, P. Design of folic acid-conjugated nanoparticles for drug targeting. J. Pharm. Sci. 2000, 89, 1452–1464.

30. Tudisco, C.; Cambria, M.T.; Sinatra, F.; Bertani, F.; Alba, A.; Giuffrida, A.E.; Saccone, S.; Fantechi, E.; Innocenti, C.; Sangregorio, C.; et al. Multifunctional magnetic nanoparticles for enhanced intracellular drug transport. J. Mater. Chem. B 2015, 3, 4134–4145.

31. Tudisco, C.; Cambria, M.T.; Giuffrida, A.E.; Sinatra, F.; Anfuso, C.D.; Lupo, G.; Caporarello, N.; Falanga, A.; Galdiero, S.; Oliveri, V.; et al. Comparison between folic acid and gH625 peptide-based functionalization of Fe_3O_4 magnetic nanoparticles for enhanced cell internalization. Nanoscale Res. Lett. 2018, 13, 45.

32. Tudisco, C.; Bertani, F.; Cambria, M.T.; Sinatra, F.; Fantechi, E.; Innocenti, C.; Sangregorio, C.; Dalcanale, E.; Condorelli, G.G. Functionalization of pegylated Fe_3O_4 magnetic nanoparticles with tetraphosphonate cavitand for biomedical application. Nanoscale 2013, 5, 11438–11446.

33. Bultman, S.J. Molecular pathways: Gene-environment interactions regulating dietary fiber induction of proliferation and apoptosis via butyrate for cancer prevention. Clin. Cancer Res. 2014, 20, 799–803.

34. Titus, D.; Jebaseelan, E.J.; Selvaraj, S.; Roopan, M. Chapter 12 Nanoparticle Characterization Techniques; Micro and Nano Technologies. In Green Synthesis, Characterization and Applications of Nanoparticles; Elsevier: Amsterdam, The Netherlands, 2019; pp. 303–319.

35. Low, P.S.; Kularatne, S.A. Folate-targeted therapeutic and imaging agents for cancer. Curr. Opin. Chem. Biol. 2009, 13, 256–262.

36. Boshnjaku, V.; Shim, K.W.; Tsurubuchi, T.; Ichi, S.; Szany, E.V.; Xi, G.; Mania-Farnell, B.; McLone, D.G.; Tomita, T.; Mayanil, S. Nuclear localization of folate receptor alpha: A new role as a transcription factor. Sci. Rep. 2012, 2, 980.

37. Vergote, I.B.; Marth, C.; Coleman, R.L. Role of the folate receptor in ovarian cancer treatment: Evidence, mechanism, and clinical implications. Cancer Metastasis Rev. 2015, 34, 41–52.

38. Cheung, A.; Bax, H.J.; Josephs, D.H.; Ilieva, K.M.; Pellizzari, G.; Opzoomer, J.; Bloomfield, J.; Fittall, M.; Grigoriadis, A.; Figini, M.; et al. Targeting folate receptor alpha for cancer treatment. Oncotarget 2016, 7, 52553–52574.

39. Foglietta, F.; Serpe, L.; Canaparo, R.; Vivenza, N.; Riccio, G.; Imbalzano, E.; Gasco, P.; Zara, G.P. Modulation of butyrate anticancer activity by solid lipid nanoparticle delivery: An in vitro investigation on human breast cancer and leukemia cell lines. J. Pharm. Pharm. Sci. 2014, 17, 231–247.

40. Peng, Z.G.; Hidajat, K.; Uddin, M.S. Adsorption of bovine serum albumin on nanosized magnetic particles. J. Colloid Interface Sci. 2004, 271, 277–283.

41. Lee, R.J.; Low, P.S. Delivery of liposomes into cultured KB cells via folate receptor-mediated endocytosis. J. Biol. Chem. 1994, 5, 3198–3204.

CHAPTER 6:

Enhancement of Temozolomide absorption and efficiency in glioblastoma treatment by MIL-modified Fe_3O_4 magnetic nanoparticles

6.1. Introduction

Glioblastoma multiforme (GBM) is one of the most common brain tumours, fatal and difficult to treat. [1]

Surgical removal of the tumor, followed by radiotherapy and oral administration of temozolomide (TMZ), is the current pharmacological procedure, but it only improves the patient's overall survival. [2] Patients with glioblastoma have a current median survival (MS) of approximately 15 months and the average survival over five years is less than 5%. [3,4] TMZ is the primary chemotherapeutic agent in GBM which, at physiological pH, is naturally hydrolyzed to 5-(3-methyltria-zen-1-yl) imidazole-4-carboxamide (MTIC), which quickly degrades to 5-aminoimidazole-4-carboxamide (AIC) and methyldiazonium ion, an alkylating species of DNA (Fig.6.1). [5]

Compared to TMZ, MTIC has low penetration of the blood brain barrier and reduced cellular absorption. Therefore, the accumulation of effective therapeutic quantities of MTIC at the tumor site depends on the stability of the TMZ. However, because of the rapid elimination rate and the short half-life of about two hours, most oral TMZ do not reach the tumor. [6] In fact, only approximately 20% of the administered dose of TMZ is generally detected in cerebrospinal fluid and high doses of TMZ need to be administered several times to obtain an effective anticancer effect, causing

unwanted effects like myelosuppression. [7,8] Consequently, a major challenge for the treatment of GBM is the development of an appropriate carrier to protect and deliver a specific drug like TMZ.

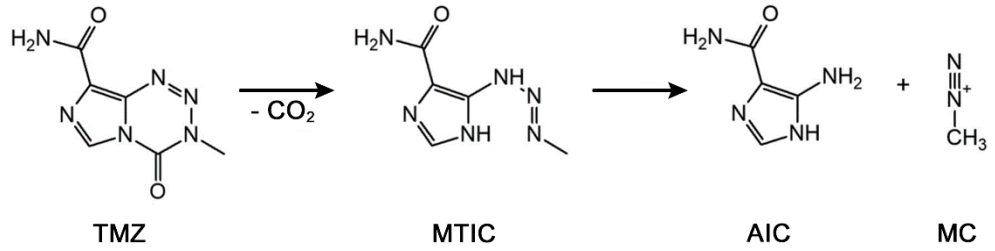

Fig.6.1. Schematic representation for TMZ hydrolysis to 5-(3-methyltriazen-1-yl) imidazole-4-carboxamide (MITC), 5-amino-imidazole-4-carboxamide (AIC) and methyldiazonium ion (MC) in aqueous solution.

In this regard nanostructured systems such as liposomes, polymeric and functionalized inorganic nanoparticles yielded promising results in the delivery of active drugs to the brain [10–13] and, in particular, more attention has been paid to functionalized organic Fe_3O_4 nanoparticles [14,15] due to the combination of magnetic properties and the biocompatibility of the iron core with the versatility of the functional shells. [16,17]

Recently, Metal-Organic Frameworks (MOFs) coordination polymers made up of metal nodes and polydentate organic linkers organized into open porous structures [18,19] and, among them, MILs (Materials Institute Lavoisier) an MOF subclass consisting of trivalent transition metals and bi- or tri-carboxylic ligands, has demonstrated a high potential for biomedical applications, both as pure crystals or as composite materials, thanks to their biocompatibility and their ability to load molecules into their porous structure. [20–24] Moreover, some articles have reported the potential to combine magnetic nanoparticles with MILs structures either as composite materials made of MILs crystals decorated or loaded with magnetic Fe_3O_4

nanoparticles [25–28] or core-shell systems where a Fe_3O_4 core is covered by a MIL shell. [29–35]

In both cases, particulate sizes generally varied from 200 to 500 nm. These systems have been used with success for applications ranging from environmental remediation to catalysis and biosensing. However, the large size of these compounds does not allow their use for drug-delivery applications, especially for brain cancer therapy.

In view of the remarkable properties of magnetic nanoparticles modified MILs, the combination of these elements can be a key strategy to build an effective delivery system for TMZ if nanosized composites can be designed.

In this chapter, a synthetic pathway to modify Fe_3O_4 magnetic nanoparticles with MIL-based structures (formed by Fe^{+3} and 2-aminoterephthalate) avoiding the growth of large MIL crystals has been developed.

Fe MILs obtained using terephthalate ligands usually occur in a variety of stereoisomers (most common of which are MIL-101, 88B and 53) with the general formula $[Fe_3(O)X\text{-}(Solv)_2(C_8H_5NO_4)_3]$, [20,36,37] (X = Cl^- or OH^-, and Solv = EtOH, DMF or H_2O) all with high porosity and surface area.

The aim is to prepare a hybrid system (MNPs@MIL) of nanoscale dimensions (50 nm) that retains the magnetic properties of the iron core in order to allow magnetic separations and the loading capability of porous Fe-MILs. Furthermore, as previous results suggested, the toxicity of Fe_3O_4 nanoparticles and iron-based MIL is generally considered to be very low thanks to biocompatibility of their components (iron and terephthalic acid) that have negligible toxicity at the investigated concentrations. [13,38-41]

Load/release properties has been determined using a Rhodamine dye as luminescent probe.

Cell viability was evaluated by 3-(4,5-dimethylthiazol-2-yl)-2,5-diphenyltetrazolium bromide (MTT) tests.

The cellular internalization and the high capacity of MNP@MILs to deliver TMZ for the treatment of GBM were analyzed by optical microscopy.

6.2. Results and Discussion

The adopted synthesis pathways for the modification of the iron oxide magnetic nanoparticles (MNPs) are schematized in Fig. 6.2.

The MNPs were obtained by co-precipitation method. They are the magnetic core of the nanosystem, but they are also an Fe^{3+} source for MIL growth. In particular, modified nanoparticles were obtained through two similar routes both using 2-aminoterephthalic acid as organic precursor.

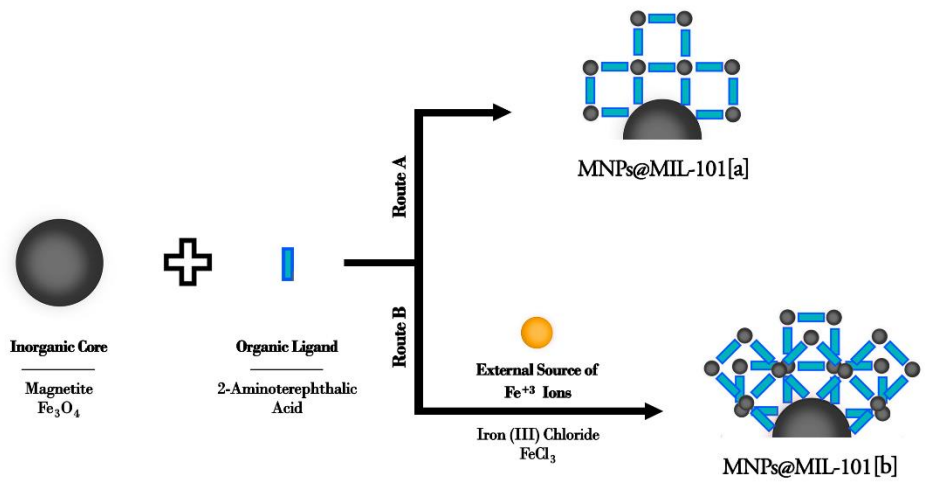

Fig.6.2. Schematic representation for the two synthetic routes proposed for the preparation of functionalized MNPs.

In the first route Fe_3O_4 nanoparticles are the only source of the Fe^{3+} ions (Fig.6.2 route a) while in the second route (b) besides Fe_3O_4, another external source of Fe^{3+} ions ($FeCl_3$) was added. The use of the iron

nanoparticles themselves as Fe^{3+} ion source is a key point for the growth of the MIL structure on the MNPs. In addition, the synthetic protocols involve very low temperatures and short reaction times, thus preserving the structure and the properties of the iron oxide magnetic core.

The XRD diffraction patterns of the bare MNPs and the hybrid systems are reported in Fig. 6.3a. Patterns of MNPs show peaks at 2θ = 30.3°, 35.7° and 43.3° associated with (220), (311) and (400) planes of crystalline Fe_3O_4 nanoparticles, confirming the presence of the magnetite phase. [43] Following the functionalization of MNP with MILs through route (a) (MNPs@MIL[a]), no sharp reflections were detected, which indicates that the formation of isolated fully crystallized MOFs was prevented. [35,44,45]

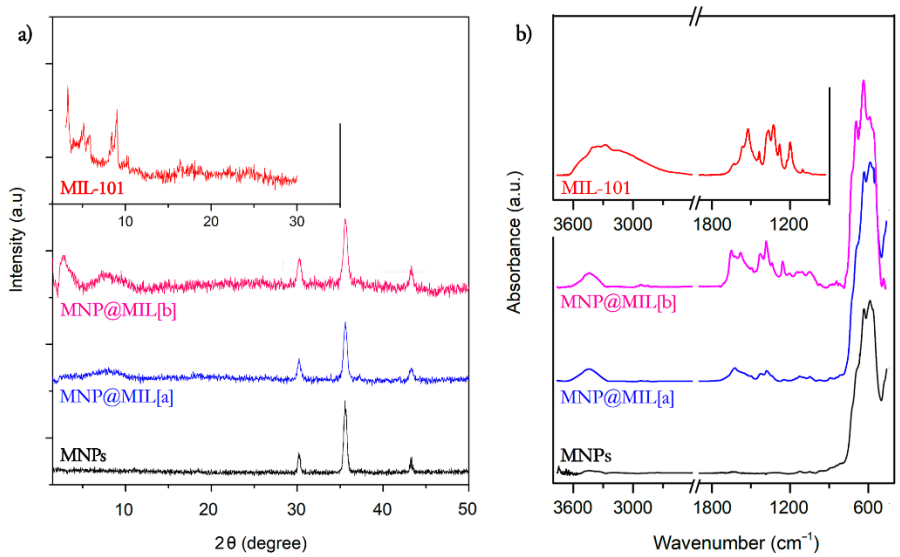

Fig.6.3. (a) XRD diffraction pattern of MNP nanoparticles (black line) and MNPs functionalized with MILs, obtained in the absence of $FeCl_3$ (route a, blue line) and in the presence of $FeCl_3$ (route b, magenta line). The insert is the XRD diffraction pattern of MIL-101. (b) FTIR spectra of MNPs nanoparticles (black line) and hybrid MNPs@MIL obtained through a (blue line) and b synthesis protocols (magenta line). The insert is the FT-IR spectra of MIL-101.

A broad and very weak signal was detected below 10° in the diffractogram of MNPs@MIL[a] and a slightly stronger wide signals in the range 4-5° and 6-8° in the case of MNPs@MIL[b] obtained with $FeCl_3$. These broad signals at low values of 2θ are in the typical region observed for the MIL phases and especially for the MIL-101 phase. [35,46] The XRD patterns of MIL-101 powders are provided as a reference in the insert of Fig. 6.3a. Note that in comparison with powders, the signals were much broader and weaker because the MIL structures are grown on the MNPs and may not crystallize in 3D grains, which are generally larger than 200-400 nm. [47]

The presence of MILs on the magnetic nanoparticles was verified by FTIR spectroscopy. Fig. 6.3b shows the FTIR spectra of the bare Fe_3O_4 and of the MNPs@MIL systems. The most intense peak in the spectrum of Fe_3O_4 nanoparticles at 600 cm^{-1} is associated with Fe-O stretching modes, typical of iron oxides. The MNPs@MIL spectra demonstrate for both syntheses the formation of MIL showing the typical vibrationas modes of aminoterephthalate ligands. In particular, the peak at 1250 cm^{-1} is characteristic of C-N symmetric and asymmetric stretching of the amino group. Moreover, the 1310–1420 cm^{-1} and 1510–1590 cm^{-1} signals are due to the COO^- symmetric and asymmetric stretching of the terephthalate ligands. [46,47] The chemical nature of MIL layers coating magnetic nanoparticles has been studied by XPS, which is a surface sensitive technique. Table 1 presents the atomic composition of Fe_3O_4 surfaces before and after MIL growth. Following the growth of MOF, the superficial composition changes, indicating the formation of MIL layers. In particular, the MIL functionalized NMP surface analyses showed an increase in C concentration, as might be expected for the formation of a layer containing an organic ligand, and the decrease in iron concentration due to the lower density of iron in the MIL layers in comparison to the bare Fe_3O_4 oxides.

XPS Atomic Concentration					
	C 1s	O 1s	N 1s	Fe 2p3	Cl 2p
MNPs	12.1	64.9	0.2	22.5	
MNP@MIL[a]	27.2	53.8	2.0	17.0	-
MNP@MIL[b]	35.3	51.3	2.1	10.7	0.6

Table 1. XPS atomic concentration of MNPs, MNPs@MIL [a] and [b].

In addition, the two MNPs@MIL spectra exhibit a significant amount of N because of the amino groups of the aminoterephthalate ligands, while only a negligible concentration of N (around 0.2%) is present on bare NMP due to adventitious contamination. The major difference between MNPs@MIL[a] and MNPs@MIL[b] resides in the presence of chlorine.

As might be expected, the sample MNPs@MIL[b] showed the presence of Cl^- in the lattice, according to the general formula $[Fe_3(O)X(Solv)_2(C_8H_5NO_4)_3]$ with Solv = EtOH or DMF and $X = Cl^-$ as a result of the addition of $FeCl_3$ during synthesis, whereas MNPs@MIL[a] showed no chlorine suggesting $X = OH^-$ in the general formula.

Figure 6.4 compares N 1s (a) and Fe 2p (b) bands of all the samples synthetized: bare MNPs, MNPs@MIL [a] and [b] respectively. As regard, N 1s peak of both samples MNPs@MIL [a] and [b], it consists of a broad signal at about 400.1 eV, typical of 2-aminoterphthalic ligand. [47,48] Similarly, also the Fe 2p signal (Fig. 6.3b) showed a broad peak for all samples as observed for most of the iron compounds because of the presence of typical multiplet splittings [49]. The centroid of the signal is at 711.1 eV for bare Fe_3O_4 due to the convolution of the Fe^{2+} and Fe^{3+} [49] ions.

After growing MIL, the centroid moved towards 712.0 eV, probably because of the convolution of Fe^{3+} in the MIL structure (usually around 712.6 eV) and Fe^{3+}/Fe^{2+} ions of Fe_3O_4.

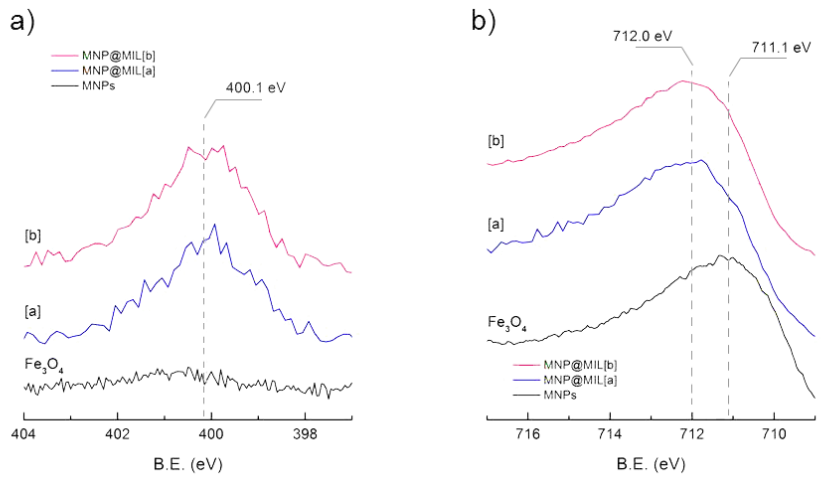

Fig.6.4. XPS spectra of N 1s (a), Fe 2p (b) of bare MNPs (bottom), MNPs@MIL[a] (middle) and MNPs@MIL[b] (top).

The evolution of the C 1s signal after the formation of the hybrid MIL structure was reported in Fig. 6.4. Before growing MIL, the C 1s signal on naked NPs is mainly due to adventitious carbon. [50,51] which is always present in XPS spectra and usually consists of a main peak at 285 eV and a small component at 286.2 eV due to oxidized carbons. A low-intensity tail around 288-289 eV is also likely observed because of surface carbonate formation.

After growing MIL, in addition to a significant increase in signal intensity (Table 1), the shape of the C 1s peak itself has changed. In particular, for both MNPs@MIL [a] and [b] samples, the band (Fig.6.5) consists mainly of three components at 285, 286.5 and 288.6 eV. The strongest peak at 285 eV is due to aliphatic and aromatic hydrocarbon atoms and "adventitious" carbon. [50,51] The component centered at 286.5 eV is attributable to C-N atoms of the amino terephthalic moieties and C-O groups of ethanol, used as solvent and probably adsorbed into the MIL cavities. The peak at 288.6 eV is characteristic of carboxylate groups ($-COO^-$). [47]

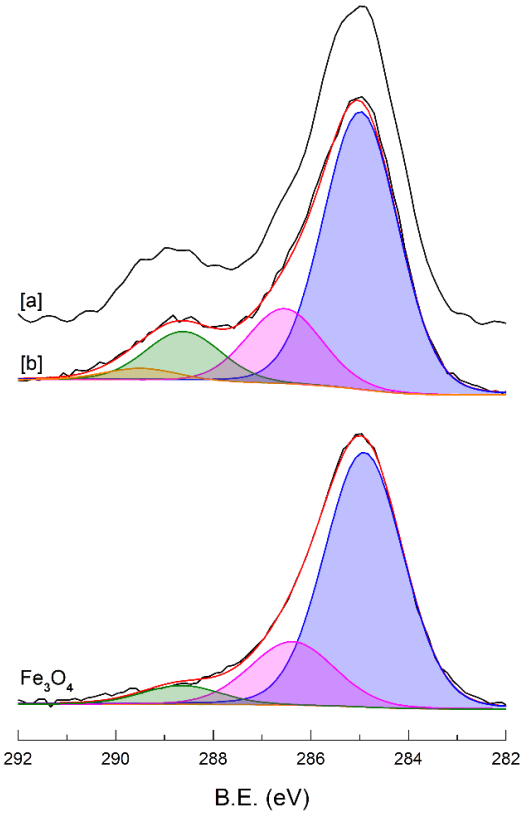

Fig.6.5. XPS spectra of C1s region of bare MNPs (bottom), MNPs@MIL[b] (middle) and MNPs@MIL[a] (top).

Furthermore, a broad and weak signal is detected at 289.4 eV and is caused by unreacted carboxylic acid (-COOH). [52]

Figures 6.6 a–c illustrates SEM morphologies of magnetic nanoparticles before (Fig. 6.5a) and after their functionalization with MIL frameworks through the synthetic pathways [a] and [b] (Fig. 6.6b and 6.6c). For all samples, SEM images show homogeneous powders with similar sized and morphological grains, with no presence of spurious crystals.

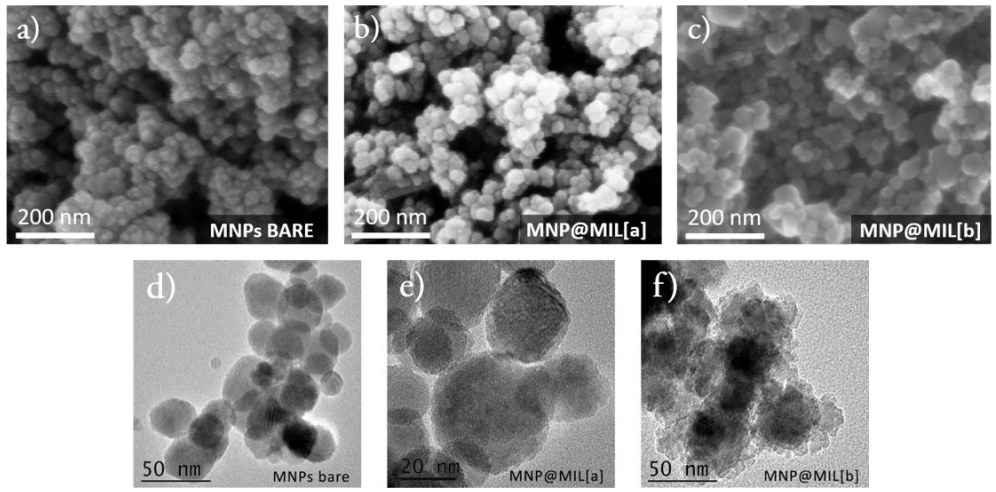

Fig.6.6. SEM morphology of (a) MNPs, (b) MNPs@MIL [a] and (c) MNPs@MIL [b]. TEM images of (d) bare MNPs, (e) hybrid MNPs@MIL[a] and (f) MNPs@MIL[b].

At the nanometric level, TEM images (Fig. 6.6d–f) showed some morphological differences between MNPs before (Fig. 6.6d) and after (Fig. 6.5e and 6.5f) MIL formation. MNPs@MIL [a] particles exhibit a mildly rough and porous structure, which is much more evident for MNPs@MIL [b] samples indicating the occurrence of MNP modifications correlated to the formation of the iron-based MILs. The particle size distributions estimated from the SEM and TEM images using Gwyddion [53] are centered at approximately 25 nm, 30 nm and 40 nm for bare MNPs, MNPs@MIL [a] and MNPs@MIL [b], respectively, with a full half width of about 10 nm in all cases. Unfortunately, it was not possible to study the crystalline structure of these hybrid systems by selected area electron diffraction (SAED) likely caused of the well-known lability of MOF structures under electron beam analysis. [54]

The quantity of organic material in the system was determined using TGA. The TGA curve for bare MNPs in the range of 25°C to 500°C shows (Fig. 6.7) a total weight loss below 250°C of about 2.2%, probably due to evaporation of adsorbed solvents and water molecules. The MNPs@MIL[a]

and [b] TGA curves display the same behavior of bare Fe_3O_4 particles up to approximately 250°C.

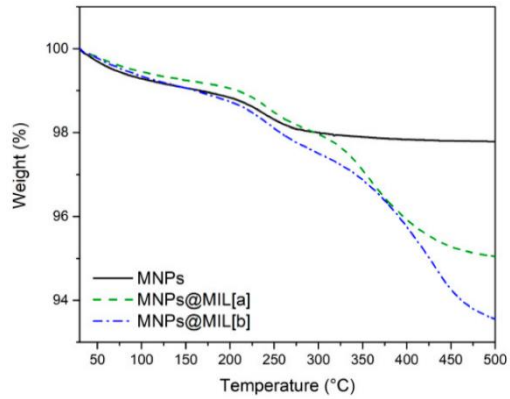

Fig.6.7. TGA plots of bare MNPs (black line), hybrid MNPs@MIL[a] (green line) and MNPs@MIL[b] (blue line).

Above this temperature, there is a greater weight loss than bare MNPs for both MNPs@MIL systems, because of the degradation of the MILs' organic ligands. For MNPs@MIL[a] and [b], the total weight loss amounts to 4.9% and 6.4%, respectively. Comparing the values with that of bare MNPs indicates that the organic component represents 2.7% of the total mass for MNPs@MIL[a] and 4.2% for MNPs@MIL[b]. Assuming the general formula $[Fe_3(O)X\text{-}(ethanol)_2(C_8H_5NO_4)_3]$ with $X = OH^-$ for MNPs@MIL[a] and $X = Cl^-$ for MNPs@MIL[b], the estimated weight percentage of the MIL in the MNPs@MIL powders is 3.6% for route (a) and 5.7% and (b).

The ability of the MNPs@MIL hybrid system of loading guest molecules was assessed using Rhodamine B (Rhod) as an optical probe. In particular, the loading capacity of MNPs@MIL[a] and [b] was compared with bare MNPs in order to determine the improvement of the loading capability resulting from the presence of a porous MIL-based system. Fig. 6.8a displays the change in residual concentrations (C) of Rhod as C/C_0 (where C_0 is the initial concentration = $6x10^{-6}$ M) versus loading time. Bare

nanoparticles (black line) show negligible adsorption capacity as no change in Rhod concentration is observed during the entire adsorption time. The MNPs@MIL[b] (blue line) has a fast initial load during the first 30 minutes, followed by a continuous load with a lower rate in the next 90 minutes. Conversely, the MNPs@MIL[a] loading (green line) is slower and slightly less effective. The difference in behaviour between the two materials can be explained by the increase in the percentage of organic component that covers nanoparticles and the higher degree of crystallinity of the MIL, as evidenced by the TGA and the XRD pattern. Fig 6.8b compares the release profile for MNPs@MIL[a] and MNPs@MIL[b] into water.

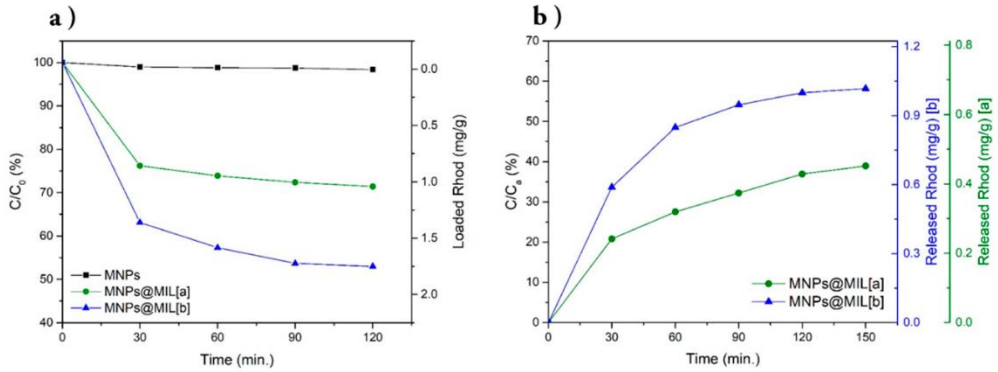

Fig.6.8. (a) Dependence of the residual Rhod concentrations (C) as C/C_0 (where C_0 is the initial concentration = 6×10^{-6} M) upon loading times using bare MNPs (black line), MNPs@MIL[a] (green line) and MNPs@MIL[b] (blue line); the right axis indicates the amount of loaded Rhod (mg/g); (b) Release plots of bare MNPs (black line), MNPs@MIL[a] (green line) and MNPs@MIL[b] (blue line). The amount of released probe is indicated as percentage of the loaded probe (C/C_a where C_a is the concentration (mg/g) of loaded Rhod); the right axes indicate the amount of released Rhod (mg/g).

As indicated, the quantity of Rhod released by MNPs@MIL[a] (green line) is 0.4 mg/g, which represents approximately 40% of the amount of Rhod loaded (Ca = 1.0 mg/g). Conversely, the MNP@MIL[b] system results in a more effective release of approximately 1.0 mg/g, which represents 60%

of the quantity of Rhod loaded (Ca = 1.8 mg/g) and is two and a half times higher than MNPs@MIL[a].Therefore, both systems MNPs@MIL[a] and [b] demonstrated improved loading capabilities over the bare Fe_3O_4 MNPs, thanks to the presence of the MIL porous structure. In particular, MNPs@MIL[b] exhibits the best performance in terms of amount of loaded and released materials and, for this reason, the functional properties of MNP@MIL[b] were applied for the in vitro treatment of glioblastoma cells using TMZ as antitumor drug.

Fig. 6.9 illustrates the TMZ loading rate by bare MNPs and MNPs@MIL[b]. In the case of bare nanoparticles, no drug loading was observed, while for MNPs@MIL[b] the percentage of drug loaded increased considerably over a total period of 2 hours. The amount of drug loaded over time is in line with what was learned during the tests with the optical probe and, after 120 minutes, 23% of the original drug concentration (about 12 mg/g) was already loaded on the surface of MNPs@MIL[b].

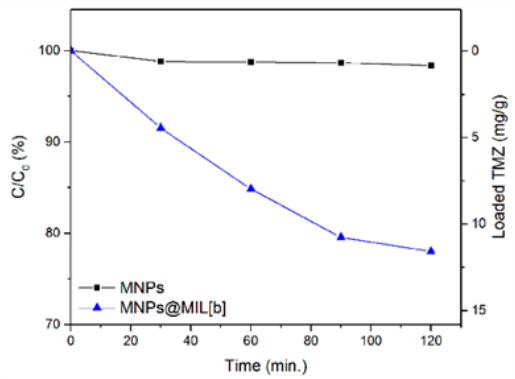

Fig.6.9. Dependence of the residual TMZ concentrations (C) as C/C_0 (where C_0 is the initial concentration = 2×10^{-4} M) upon loading times using bare MNPs (black line) and MNPs@MIL[b] (blue line); the right axis indicates the amount of loaded TMZ (mg/g).

Unfortunately, it was not possible to study TMZ release because of its low absorption coefficient and its maximum position (372 nm) which

overlaps with that of the free aminoterephthalic ligand present in MIL solutions (see chapter 2).

With the goal of assess cellular uptake, human glioblastoma cells (A-172) were incubated both with MNPs@MIL[b] and MNPs to study the fate of the endocytosed nanoparticles at different time points. The uptake was evaluated via the PerkinElmer Operetta High-Content Imaging System. As shown in Fig. 6.10, we found that MNPs@MIL[b] internalization occurs both in the cytoplasm and in the nucleus is more evident than in the bare MNPs at all the concentrations investigated. This behaviour suggests that MNPs@MIL[b] is able to target brain tumors more efficiently than MNP.

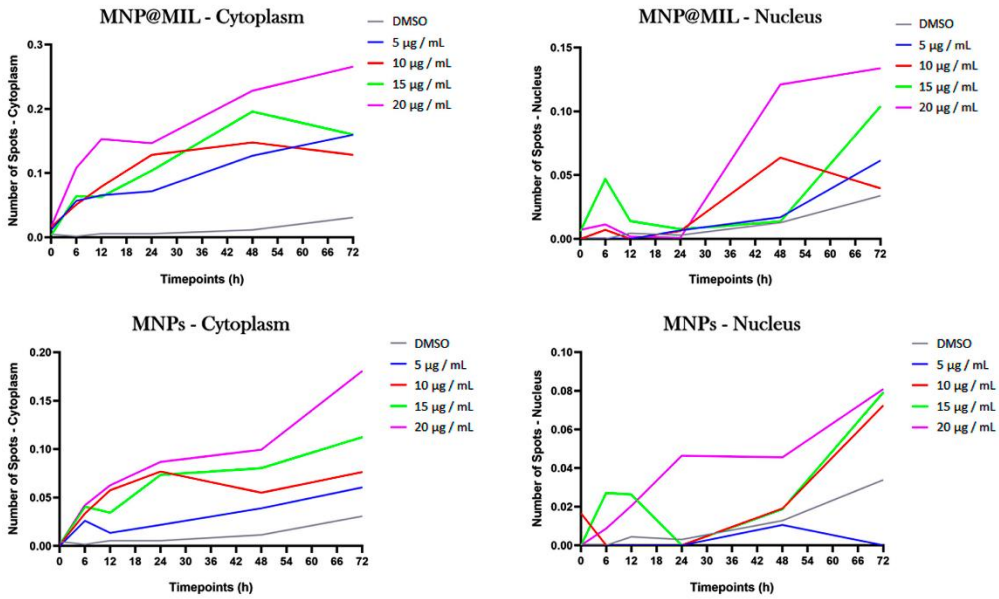

Fig.6.10. Internalization rate of MNPs@MIL[b] and MNPs in A-172 glioblastoma cells as measured by Operetta High-Content Imaging System. Data are reported as number of spots detected in cell cytoplasm and nucleus (time course 0–72 h). Data are presented as the average of four different replicates.

To determine whether TMZ, MNPs@MIL[b] and TMZ-loaded MNPs@MIL[b] affect the viability of human glioblastoma cells, we examined their effects on A172 cells. The cell line was treated with different concentrations of MNPs@MIL[b] (5–20 μg/mL) and TMZ (0.125–0.5 μM) for 72 hours and then, throught MTT assay, the cell viability was assessed.

This was illustrated in Fig. 6.11. All tested concentrations of MNPs@MIL[b] reduced cell viability in a dose-dependent manner only at 48 hours, whereas DMSO treatment, used as a vehicle, had no significant differences from untreated cells (control).

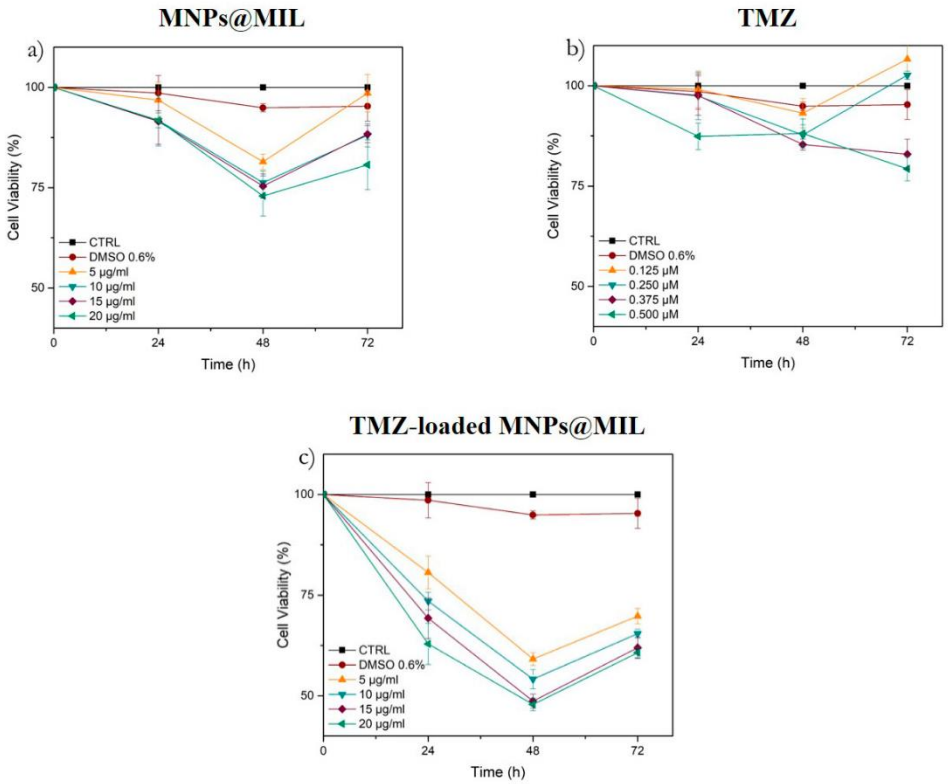

Fig.6.11. Cytotoxicity analysis of MNPs@MIL[b] (a), TMZ (b) and TMZ-loaded MNPs@MIL[b] (c) in human glioblastoma cells (A172) after 24 h, 48 h and 72 h. Data are presented as the average of three different replicates.

All TMZ concentrations slightly decreased cell viability after 48 h. Only TMZ concentrations of 0.375 and 0.5 μM caused a detectable decrease of cell viability after 72 hours. When MNPs@MIL[b] was loaded with TMZ, cytotoxicity in A172 cells was significantly increased relative to the simple drug solution and base material.

In particular, after 48 hours of combined treatment, we found that MNPs@MIL[b] (15 and 20 μg/mL) decreased the viability of A172 to approximately 50%.

6.3. Conclusions

In this chapter, a new hybrid nanosystem with a Fe-based MIL grown on a magnetic Fe_3O_4 core was successfully synthesized.

MIL growth on nanoparticles was performed through two similar routes using 2-aminoterephthalic acid as an organic precursor. In the first route, Fe_3O_4 nanoparticles are the only source of the Fe^{3+} ions, while in the second route, in addition to Fe_3O_4, an external source of Fe^{3+} ions ($FeCl_3$) was added.

The chemical characterization of bulk and surface indicated, for both synthetic pathways, the formation of an iron-based MIL of poor crystalline structure on the Fe_3O_4 NPs, which have preserved both their crystallographic structure and their magnetic properties since they can be easily separated magnetically.

Both SEM and TEM images revealed no isolated MOF crystals, but the nanoparticles showed a rough and porous structure probably due to MIL growth, which was evaluated by TGA between 3.6% and 5.7% depending on the synthetic route. In particular, MNPs@MIL nanopowders produced with the route (b) have a higher amount of MIL than MNPs@MIL[a]. Therefore, the different synthetic pathways also influenced the loading/release properties of this hybrid material. The two systems, MNPs@MIL[a] and [b], showed

enhanced loading capacities compared to bare Fe_3O_4 MNPs, probably due to the presence of the porous MIL structure, and MNPs@MIL[b] showed the best performance in terms of quantity of materials loaded and released.

Moreover, compared to the previously reported composite materials, our combined system retains the nanometer size ($\leq$ 50 nm) after MIL growth.

The functional properties of MNPs@MIL[b] were exploited through in vitro drug delivery experiments using TMZ as a drug to treat glioblastoma.

Experiments indicated that this hybrid system is able to penetrate the A172 cell line more effectively than bare MNPs, and the use of TMZ-loaded MIL@MNPs increase the effectiveness of the drug over the free TMZ.

Finally, our findings suggest that the combination of MIL frameworks with magnetic nanoparticles represents a promising approach for the development of new drug delivery systems.

References

1. Burger, P.C.; Vogel, F.S.; Green, S.B.; Strike, T.A. Glioblastoma multiforme and anaplastic astrocytoma, Pathologic criteria and prognostic implications. Cancer 1985, 56, 1106–1111.

2. Stupp, R.; Hegi, M.E.; Mason, W.P.; van den Bent, M.J.; Taphoorn, M.J.; Janzer, R.C.; Ludwin, S.K.; Allgeier, A.; Fisher, B.; Belanger, K.; et al. Effects of radiotherapy with concomitant and adjuvant temozolomide versus radiotherapy alone on survival in glioblastoma in a randomised phase III study: 5-year analysis of the EORTC-NCIC trial. Lancet Oncol. 2009, 10, 459–466.

3. Krex, D.; Klink, B.; Hartmann, C.; von Deimling, A.; Pietsch, T.; Simon, M.; Sabel, M.; Steinbach, J.P.; Heese, O.; Reifenberger, G.; et al. for the German Glioma Network, Long-term survival with glioblastoma multiforme. Brain 2007, 130, 2596–2606.

4. Delgado-Lopez, P.D.; Corrales-Garcia, E.M. Survival in glioblastoma: A review on the impact of treatment modalities. Clin. Transl. Oncol. 2016, 18, 1062–1071.

5. Lopes, I.C.; De Oliveira, S.C.B.; Oliveira-Brett, A.M. Temozolomide chemical degradation to 5-aminoimidazole-4-carboxamide - Electrochemical study. J. Electroanal. Chem. 2013, 704, 183–189.

6. Omuro, A.; DeAngelis, L.M. Glioblastoma and Other Malignant Gliomas: A Clinical Review. JAMA 2013, 310, 1842–1850.

7. Chamberlain, M.C. Temozolomide: Therapeutic limitations in the treatment of adult high-grade gliomas. Expert Rev. Neurother. 2010, 10, 1537–1544.

8. Lonardi, S.; Tosoni, A.; Brandes, A.A. Adjuvant chemotherapy in the treatment of high-grade gliomas. Cancer Treat. Rev. 2005, 31, 79–89.

9. Genovese, C.; Cambria, M.T.; D'angeli, F.; Addamo, A.P.; Malfa, G.A.; Siracusa, L.; Pulvirenti, L.; Anfuso, C.D.; Lupo, G.; Salmeri, M. The double effect of walnut septum extract (Juglans regia L.) counteracts A172 glioblastoma cell survival and bacterial growth. Int. J. Oncol. 2020, 57, 1129–1144.

10. Fang, C.; Wang, K.; Stephen, Z.R.; Mu, Q.; Kievit, F.M.; Chiu, D.T.; Press, O.W.; Zhang, M. Temozolomide nanoparticles for targeted glioblastoma therapy. ACS Appl. Mater. Interfaces 2015, 7, 6674–6682.

11. Martinho, O.; Vilaça, N.; Castro, P.J.G.; Amorim, R.; Fonseca, A.M.; Baltazar, F.; Reis, R.M.; Neves, I.C. In vitro and in vivo studies of temozolomide loading in zeolite structures as drug delivery systems for glioblastoma. RSC Adv. 2015, 5, 28219–28227.

12. Lam, F.C.; Morton, S.W.; Wyckoff, J.; Han, L.T.V.; Hwang, M.K.; Maffa, A.; Balkanska-Sinclair, E.; Yaffe, M.B.; Floyd, S.R.; Hammond, P.T. Enhanced efficacy of combined temozolomide and bromodomain inhibitor therapy for gliomas using targeted nanoparticles. Nat. Commun. 2018, 9, 1991.

13. Tudisco, C.; Cambria, M.T.; Giuffrida, A.E.; Sinatra, F.; Anfuso, C.D.; Lupo, G.; Caporarello, N.; Falanga, A.; Galdiero, S.; Oliveri, V.; et al. Comparison Between Folic Acid and gH625 Peptide-Based Functionalization of Fe3O4 Magnetic Nanoparticles for Enhanced Cell Internalization. Nanoscale Res. Lett. 2018, 13, 45.

14. Yiu, H.H.P. Engineering the multifunctional surface on magnetic nanoparticles for targeted biomedical applications: A chemical approach. Nanomedicine 2011, 6, 1429–1446.

15. Santhosh, P.B.; Ulrih, N.P. Multifunctional superparamagnetic iron oxide nanoparticles: Promising tools in cancer theranostics. Cancer Lett. 2013, 336, 8–17.

16. Cambria, M.T.; Villaggio, G.; Laudani, S.; Pulvirenti, L.; Federico, C.; Saccone, S.; Condorelli, G.G.; Sinatra, F. The Interplay between Fe_3O_4 Superparamagnetic Nanoparticles, Sodium Butyrate, and Folic Acid for Intracellular Transport. Int. J. Mol. Sci. 2020, 21, 8473.

17. Tudisco, C.; Cambria, M.T.; Sinatra, F.; Bertani, F.; Alba, A.; Giuffrida, A.E.; Saccone, S.; Fantechi, E.; Innocenti, C.; Sangregorio, C.; et al. Multifunctional magnetic nanoparticles for enhanced intracellular drug transport. J. Mater. Chem. B 2015, 3, 4134–4145.

18. Zhihua, F.U.; Gang, X.U. Crystalline, highly oriented MOF thin film: The fabrication and application. Chem. Rec. 2017, 17, 518–534.

19. Horcajada, P.; Gref, R.; Baati, T.; Allan, P.K.; Maurin, G.; Couvreur, P.; Ferey, G.; Morris, R.E.; Serre, C. Metal-Organic Frameworks in Biomedicine. Chem. Rev. 2012, 112, 1232–1268.

20. Zorainy, M.Y.; Alkalla, M.I.G.; Kaliaguine, S.; Boffito, D.C.C. Revisiting the MIL-101 metal-organic framework: Design, synthesis, modifications, advances, and recent applications. J. Mater. Chem. A 2021, 9, 22159–22217.

21. Hamedi, A.; Trotta, F.; Borhani Zarandi, M.; Zanetti, M.; Caldera, F.; Anceschi, A.; Nateghi, M.R. In Situ Synthesis of MIL-100 (Fe) at the surface of Fe_3O_4@AC as highly efficient dye adsorbing nanocomposite. Int. J. Mol. Sci. 2019, 20, 5612.

22. Karimi Alavijeh, R.; Akhbari, K. Biocompatible MIL-101 (Fe) as a smart carrier with high loading potential and sustained release of curcumin. Inorg. Chem. 2020, 59, 3570–3578.

23. Pashazadeh-Panahi, P.; Belali, S.; Sohrabi, H.; Oroojalian, F.; Hashemzaei, M.; Mokhtarzadeh, A.; de la Guardia, M. Metal-organic frameworks conjugated with biomolecules as efficient platforms for development of biosensors. TrAC Trend Anal. Chem. 2021, 141, 116285. Int. J. Mol. Sci. 2022, 23, 2874 14 of 15

24. Shan, Y.; Xu, C.; Zhang, H.; Chen, H.; Bilal, M.; Niu, S.; Huang, Q. Polydopamine-Modified Metal–Organic Frameworks, NH_2-Fe-MIL-101,

as pH-Sensitive Nanocarriers for Controlled Pesticide Release. Nanomaterials 2020, 10, 2000.

25. Xing, Y.; Si, H.; Sun, D.; Hou, X. Magnetic Fe3O4@NH2-MIL-101(Fe) nanocomposites with peroxidase-like activity for colorimetric detection of glucose. Microchem. J. 2020, 156, 104929.

26. Jiang, Z.W.; Dai, F.Q.; Huang, C.Z.; Li, Y.F. Facile synthesis of a Fe_3O_4/MIL-101(Fe) composite with enhanced catalytic performance. RSC Adv. 2016, 6, 86443.

27. Samui, A.; Ray Chowdhuri, A.; Mahto, T.K.; Sahu, S.K. Fabrication of a magnetic nanoparticle embedded NH_2-MIL-88B MOF hybrid for highly efficient covalent immobilization of lipase. RSC Adv. 2016, 6, 66385.

28. Tirado-Guizar, A.; Gonzalez-Gomez,W.; Pina-Luis, G.; Galindo, J.T.E.; Paraguay-Delgado, F. Anthracene removal from water samples using a composite based on metal-organic- frameworks (MIL-101) and magnetic nanoparticles (Fe_3O_4). Nanotechnology 2020, 31, 195707.

29. Chang, S.; Liu, C.; Sun, Y.; Yan, Z.; Zhang, X.; Hu, X.; Zhang, H. Fe_3O_4 Nanoparticles Coated with Ag-Nanoparticle-Embedded Metal-Organic Framework MIL-100(Fe) for the Catalytic Reduction of 4-Nitrophenol. ACS Appl. Nano Mater. 2020, 3, 2302–2309.

30. Sturini, M.; Puscalau, C.; Guerra, G.; Maraschi, F.; Bruni, G.; Monforte, F.; Profumo, A.; Capsoni, D. Combined Layer-by-Layer/Hydrothermal Synthesis of Fe_3O_4@MIL-100(Fe) for Ofloxacin Adsorption from Environmental Waters. Nanomaterials 2021, 11, 3275.

31. He, W.; Li, Z.; Lv, S.; Niu, M.; Zhou,W.; Li, J.; Lu, R.; Gao, H.; Pan, C.; Zhang, S. Facile synthesis of Fe_3O_4@MIL-100(Fe) towards enhancing photo-Fenton like degradation of levofloxacin via a synergistic effect between Fe_3O_4 and MIL-100(Fe). Chem. Eng. J. 2021, 409, 128274.

32. Liu, S.; Zhao, Y.;Wang, T.; Liang, N.; Hou, X. Core–Shell Fe3O4@MIL-100(Fe) Magnetic Nanoparticle for Effective Removal of Meloxicam and Naproxen in Aqueous Solution. J. Chem. Eng. Data 2019, 64, 2997–3007.

33. Yang, Q.; Zhao, Q.; Ren, S.; Lu, Q.; Guo, X.; Chen, Z. Fabrication of core-shell Fe_3O_4@MIL-100(Fe) magnetic microspheres for the removal of Cr(VI) in aqueous solution. J. Solid State Chem. 2016, 244, 25–30.

34. Yue, X.; Guo,W.; Li, X.; Zhou, H.;Wang, R. Core-shell Fe_3O_4@MIL-101(Fe) composites as heterogeneous catalysts of persulfate activation for the removal of Acid Orange 7. Environ. Sci. Pollut. Res. 2016, 23, 15218–15226.

35. Li, S.; Bi, K.; Xiao, L.; Shi, X. Facile preparation of magnetic metal organic frameworks core–shell nanoparticles for stimuliresponsive drug carrier. Nanotechnology 2017, 28, 495601.

36. Maksimchuk, N.V.; Zalomaeva, O.V.; Skobelev, I.Y.; Kovalenko, K.A.; Fedin, V.P.; Kholdeeva, O.A. Metal-Organic Frameworks of the MIL-101 Family as Heterogeneous Single-Site Catalysts. Proc. Math. Phys. Eng. Sci. 2012, 468, 2017–2034.

37. Carson, F.; Su, J.; Platero-Prats, A. E.;Wan,W.; Yun, Y.; Samain, L.; Zou, X. Framework isomerism in vanadium metal–organic frameworks: MIL-88B (V) and MIL-101 (V). Cryst. Growth Des. 2013, 13, 5036–5044.

38. Tudisco, C.; Bertani, F.; Cambria, M.T.; Sinatra, F.; Fantechi, E.; Innocenti, C.; Sangregorio, C.; Dalcanale, E.; Condorelli, G.G. Functionalization of Pegylated Fe_3O_4 Magnetic Nanoparticles with Tetraphosphonate Cavitand for Biomedical Application. Nanoscale 2013, 5, 11438–11446.

39. Bang, D.Y.; Lee, I.K.; Lee, B.-M. Toxicological Characterization of Phthalic Acid. Toxicol. Res. 2011, 27, 191–203.

40. Singh, N.; Qutub, S.; Khashab, N.M. Biocompatibility and biodegradability of metal organic frameworks for biomedical applications. J. Mater. Chem. B 2021, 9, 5925.

41. Tamames-Tabar, C.; Cunha, D.; Imbuluzqueta, E.; Ragon, F.; Serre, C.; Blanco-Prieto, M.J.; Horcajada, P. Cytotoxicity of nanoscaled metal–organic frameworks. J. Mater. Chem. B 2014, 2, 262–271.

42. Baati, T.; Njim, L.; Neffati, F.; Kerkeni, A.; Bouttemi, M.; Gref, R.; Najjar, M.F.; Zakhama, A.; Couvreur, P.; Serre, C.; et al. In depth analysis of the in vivo toxicity of nanoparticles of porous iron(III) metal–organic frameworks. Chem. Sci. 2013, 4, 1597–1607.

43. Ramalingam, B.; Parandhaman, T.; Choudhary, P.; Das, S.K. Biomaterial functionalized graphene-magnetite nanocomposite: A novel approach for

simultaneous removal of anionic dyes and heavy-metal ions. ACS Sustain. Chem. Eng. 2018, 6, 6328–6341.

44. Bauer, S.; Serre, C.; Devic, T.; Horcajada, P.; Marrot, J.; Ferey, G.; Stock, N. High-Throughput Assisted Rationalization of the Formation of Metal Organic Frameworks in the Iron (III) Aminoterephthalate Solvothermal System. Inorg. Chem. 2008, 47, 7568–7576.

45. Shi, L.; Wang, T.; Zhang, H.; Chang, K.; Meng, X.; Liu, H.; Ye, J. An Amine-Functionalized Iron (III) Metal–Organic Framework as Efficient Visible-Light Photocatalyst for Cr (VI) Reduction. Adv. Sci. 2015, 2, 150000.

46. Monforte, F.; Urso, M.; Alberti, A.; Smecca, E.; Mirabella, S.; Bongiorno, C.; Mannino, G.; Condorelli, G.G. New Synthetic Route for the Growth of -FeOOH/NH_2-Mil-101 Films on Copper Foil for High Surface Area Electrodes. ACS Omega 2019, 4, 18495–18501.

47. Monforte, F.; Falsaperna, M.; Pellegrino, A.L.; Bongiorno, C.; Motta, A.; Mannino, G.; Condorelli, G.G. Direct growth on Si (100) of isolated octahedral Mil-101 (Fe) crystals for the separation of aromatic vapors. J. Phys. Chem. C 2019, 123, 28836–28845.

48. Ezugwu, C.I.; Zhang, S.; Li, S.; Shi, S.; Li, C.; Verpoort, F.; Liu, S. Efficient transformative HCHO capture by defective NH2-UiO-66 (Zr) at room temperature. Environ. Sci. Nano 2019, 6, 2931–2936. Int. J. Mol. Sci. 2022, 23, 2874 15 of 15

49. Grosvenor, A.P.; Kobe, B.A.; Biesinger, M.C.; McIntyre, N.S. Investigation of multiplet splitting of Fe 2p XPS spectra and bonding in iron compounds. Surf. Interface Anal. 2004, 36, 1564–1574.

50. Swift, I.L. Adventitious carbon? The panacea for energy referencing? Surf. Interface Anal. 1982, 4, 47–51.

51. Briggs, D.; Beamson, G. Primary and Secondary Oxygen-Induced C1s Binding Energy Shifts in X-ray Photoelectron Spectroscopy of Polymers. Anal. Chem. 1992, 64, 1729–1736.

52. Rojas, J.V.; Toro-Gonzalez, M.; Molina-Higgins, M.C.; Castano, C.E. Facile radiolytic synthesis of ruthenium nanoparticles on graphene oxide and carbon nanotubes. Mater. Sci. Eng. B 2016, 205, 28–35.

53. Neˇcas, D.; Klapetek, P. Gwyddion: An open-source software for SPM data analysis. Cent. Eur. J. Phys. 2012, 10, 181–188.

54. Liu, L.; Zhang, D.; Zhu, Y.; Han, Y. Bulk and local structures of metal–organic frameworks unravelled by high-resolution electron microscopy. Commun. Chem. 2020, 3, 99.

55. Du, P.D.; Thanh, H.T.M.; To, T.C.; Thang, H.S.; Tinh, M.X.; Tuyen, T.N.; Hoa, T.T.; Khieu, D.Q. Metal-Organic Framework MIL-101: Synthesis and Photocatalytic Degradation of Remazol Black B Dye. J. Nanomater. 2019, 2019, 606127.